ICMM

CSIC

UNIVERSIDAD AUTONOMA
DE MADRID
Departamento de Física de la Materia Condensada

Preparation, characterization and magnetic properties of epitaxial iron nanostructures

Memoria presentada para optar al grado
de Doctor en Ciencias Físicas por
Elvira Paz Pérez de Colosía

Dirigida por **Francisco Javier Palomares Simón**
Co-dirigida por **Federico Cebollada Baratas**

Tutor: **Sebastián Vieira Díaz**

Madrid, Junio 2010

A mi familia
Sofía, bienvenida

The most beautiful thing we can experience is the mysterious.
It is the source of all true art and all science.

El misterio es la cosa más bonita que podemos experimentar.
Es la fuente de todo arte y ciencia verdaderos.

Albert Einstein

Agradecimientos

En primer lugar quiero agradecer a mis directores de tesis, Javier Palomares y Federico Cebollada, por haber confiado en mi desde el primer momento, por haberme contagiado vuestro entusiasmo por la ciencia, por la posibilidad de viajar tanto, enseñandome en cada sitio que hemos compartido, y sobre todo por el apoyo y ayuda en esta recta final sin vosotros no hubiese sido posible. Gracias por estos años juntos.

A mi tutor Prof. Sebastián Vieira por su ayuda y disponibilidad.

Este trabajo ha sido posible gracias a la ayuda de mucha gente en diversas técnicas: gracias al personal de SpLine, a Juan Rubio y Pilar Ferrer, nuestros *local contacts*, por hacer tan agradable los largos días de sincrotrón y la discusión de los datos, y a German de Castro por dar siempre ideas de como mejorar las medidas; Gracias Carmen Munuera por medir mis muestras siempre con una sonrisa a pesar de que sean tan planas que son aburridas; A Nuno y Joana por ayudarme con las medidas de FMR y hacer mis estancias en Aveiro llevaderas, y a Prof. Nikolai Sovolev por estar siempre disponible; Muchas gracias a María Jesús por tantas horas de espera juntas delante del microscopio viendo rayitas, al final dió su fruto; Y a Sandra y Bert thanks for let me use the equipments and for all the samples fabricated in the distance; Y a Tolek Tyliszczak y Peter Fischer por su ayuda con las medidas en los miscroscopios de trasmisión magnética.

Gracias a Jesús M^a González por su ayuda en todo momento y sus explicaciones. A Oksana por sus discusiones micromagnéticas. A Felipe por enseñarme a programar y su paciencia cuando el ordenador no me hacía caso. A Rocio, Unai y Raḿon, por su compañía en los congresos. Y a Mariano por sus continuos ánimos.

A Prof. Burkard Hillebrands y al resto de las personas del grupo de Kaiserslautern por acogerme en su grupo, en especial a Patrizio por toda su ayuda y paciencia con mis preguntas y Patricia por los buenos momentos dentro y fuera del laboratorio.

Al ICMM y la EUTITT-UPM por darme la posibilidad de utilizar sus intalaciones. A Luis Balo por preocuparse de tener siempre el VSM lleno de He, y a la gente del taller por hacer cada cosa que he necesitado para sacar adelante este trabajo.

A Cesar por dejarme participar en su experimento de XMCD y experimentar por primera vez lo que es un sincrotrón tan bien acompañada; a todas las personas que en los congresos me han dado su punto de vista de mi trabajo, en especial a Lluis Balcells por toda la información sobre litografía y a R. Allwood por fijarse en mi poster y darme una referencia que me llevó al enfoque correcto del comportamiento de las líneas.

A los compañeros de comida Lidia, María, Mercedes, Carlos, Renaud, Cesar, Anna, Elena y Manu (Yves y Elisa cuando se apuntan) por hacer tan agradable el momento de descanso del día. Y a JuanMa y Lidia por los tés a media tarde. A los del equipo de fútbol, aunque lleve tiempo sin ir a jugar. Al resto de la gente que he conocido por los pasillos Isa, María, Pilar, Ana, Marisa, Javi, Eva, Quique, Ramón, Jangel, Chicho, Ainara, Ainoha, Lucia, Félix, Juan y un largo etcetera gracias por hacer el día a día más divertido. A José Angel y a Paqui por preguntar siempre como lo llevo y sus mensajes de ánimo. Y a mis compañeros de despacho de ahora, Mercedes y Mathias, y de antes, Ramón y Carlos por haberme aguantado esta en esta última etapa un poco nerviosa y en la anterior que no dejaba de entrar y salir del despacho.

A Chris, Alex y Antonio por las cenitas y las partidas nocturnas de Carcassonne y a la familia Antelo por sus paellas en KL.

A José Oñorbe, gracias por ayudarme a que la tesis haya quedado tan bonita, por estar siempre disponible cuando te he necesitado, disfruta de Los Ángeles. Dani, gracias por la portada, el detalle que faltaba para que la tesis sea lo que es.

A los de siempre, Ana Gil, Ana Cainzos, Ana de Mesa, Moni, Ana de la

Torre, Gala, Natalia, Marian, Vane, Ali, Miguel, Eloy, Jorge, Emili, Salces, Nacho, Raúl y Fran; A las del pueblo; A las *sisters*; A Jaime; A las *NANAS*, Ana, Jose, Sonia y Moni, y los *NANOS*, Manu, Cristian, Mikel, Bai y Rafa; Y al grupo *Usamos Alicates Montevideo*, gracias por ser parte de mi vida, por todos los momentos compartidos y los que vendrán.

A la familia de Mesa por tratarme como una hija más.

A mis compis de piso, Luis y Leyre, aunque sólo estéis los fines de semana me encanta compartir piso con vosotros, gracias por haber estado ahí todo este tiempo de escritura.

Al apoyo de toda mi familia, aunque no sepan muy bien a que me dedico, a mis tíos, primas, abuelos y a Silvia, a la pequeña Sofía por las alegrias que nos traerá, y muy especialmente a Carmen, Carlos y mis padres por haberme ayudado en esto y en cada étapa anterior de mi vida.

Contents

Resumen

Los sistemas de magnéticos nanoestructurados, tales como nanopartículas, nanohilos, multicapas y redes de nanoelementos, son hoy en día de gran interés debido a su relevancia tecnológica, especialmente por sus aplicaciones relacionadas con el almacenamiento magnético, miniaturización de sensores y dispositivos magnetoelectrónicos. Estos sistemas se caracterizan por tener al menos una de sus dimensiones más pequeña o del orden de la longitud de canje, aproximadamente del orden del ancho de la pared de dominio (típicamente decenas de nanómetros para metales de transición magnéticos), lo que produce nuevos procesos de imanación, diferentes de los del material masivo. Tanto desde el punto de vista de la implementación de los dispositivos reales como desde el del progreso de la comprensión de esta nueva fenomenología, es importante utilizar procesos de nanoestructuración fiables y repetitivos, combinados con una buena resolución a escala nanométrica que minimice las imperfecciones químicas, estructurales o morfológicas. Esto es crucial debido a que estos defectos generalmente son incontrolables y pueden jugar un papel importante en las propiedades magnéticas y mecanismos de imanación de los nanoelementos. Consecuentemente, es muy importante fabricar redes de nanoelementos bien controlados en los que los procesos de imanación sean independientes de las imperfecciones generadas durante la nanoestructuración.

Esta tesis estudia la influencia sobre los procesos de imanación de las características estructurales de redes de nanoestructuras con dos tipos de motivos, nanohilos y antidots (agujeros no magnéticos), fabricados en láminas epitaxiales de Au (001)/Fe (001)/Mg (001) de 25 nm de espesor aproximadamente, crecidas mediante ablación de laser pulsado (PLD). Este trabajo incluye una rigurosa tarea de fabricación de las redes mediante diferentes técnicas de nanolitografía, haz de iones focalizado (FIB) y haz

de electrones (EBL) tanto con resina positiva como negativa, así como una detallada caracterización estructural y química de las láminas y las redes con una amplia variedad de técnicas: difracción y reflectividad de rayos X (XRD y XRR), microscopía de fuerzas atómicas (AFM), microscopía electrónica de barrido (SEM) y espectroscopia de fotoelectrones de rayos X (XPS).

Los procesos de imanación de nanohilos, con anchuras y separación entre hilos entre 100 y 1000 nm, se han estudiado con Efecto Kerr Magnetoóptico (MOKE) y Magnetómetro de Muestra Vibrante (VSM). Se han realizado también medidas de Resonancia Ferromagnética (FMR) para analizar la existencia de anisotropías diferentes de la magnetocristalina y la de forma inherente a los hilos. Los resultados experimentales indican que sus procesos de imanación evolucionan de enganche de paredes, para ángulos pequeños entre el campo aplicado y el eje de los hilos, a una rotación de la imanación básicamente uniforme, para ángulos grandes. Este comportamiento se puede describir en términos de configuración de un único spin. La habilidad de conseguir estos nanohilos de tan alta calidad y tan controlados ha permitido desarrollar un modelo analítico basado únicamente en las propiedades intrínsecas del Fe y la forma y dimensiones de los hilos. Este modelo tan simple presenta un buen acuerdo tanto cualitativa como cuantitativamente con los resultados, poniendo en evidencia el papel practicamente irrelevante de otros factores extrínsecos en los procesos de imanación y, de acuerdo con los resultados de resonancia ferromagnética, de otras contribuciones de energía de anisotropía.

El segundo tipo de nanoestructuras que constituyen el objeto de esta tesis son redes de antidots. Dichos antidots se han fabricado con litografía de haz de iones focalizado (FIB) y haz de electrones (EBL) en láminas de Au/Fe/MgO, formando redes cuadradas de agujeros cilíndricos, con diámetro y separación entre 200 y 2000 nm y con la diagonal de las redes a lo largo del eje fácil magnetocristalino de las láminas de Fe, (100) y (010). Las inhomogeneidades de la imanación, que aparecen en la superficie lateral

de los antidots para minimizar la energía dipolar, inducen una anisotropía interna de forma caracterizada por tener las direcciones fáciles a lo largo de la diagonal, por lo que refuerzan la anisotropía magnetocristalina de las láminas. La caracterización de los antidots, realizada con efecto Kerr magnetoóptico, se ha enfocado en la dependencia de la coercitividad con el diámetro y separación. Como resultado principal, la coercitividad de las redes es hasta 10 veces mayor que la de las láminas aumentando rápidamente cuando la separación decrece, además de presentar una fuerte dependencia con la coercitividad inicial de la lámina donde se han fabricado. Se ha puesto de manifiesto la existencia de un escalado de la coercitividad con el porcentaje de material magnético alrededor de los antidots que forma estructuras inhomogéneas, evaluado mediante la longitud de correlación magnetostática.

En resumen, en esta tesis se muestra la capacidad de fabricar láminas delgadas y nanoestructuras de alta calidad, que ofrecen una oportunidad única de estudiar procesos de imanación en sistemas modelo. La optimización de los parámetros utilizados en cada uno de los diferentes procesos de fabricación ha permitido producir redes de líneas y antidots cuyas propiedades magnéticas dependen casi exclusivamente de sus características morfológicas y sus dimensiones, con una mínima influencia de las imperfecciones inherentes a los diferentes procesos de fabricación.

Abstract

Nanostructured magnetic systems such as nanoparticles, nanowires, multilayers and arrays of nanoelements have drawn a lot of attention in recent years, mainly due to their technological relevance, specially for applications related to magnetic storage, miniaturization of sensors and the so-called magnetoelectronic devices. These systems are characterized by having at least one of its morphological dimensions smaller or of the order of the exchange length, roughly corresponding to the domain wall width (typically a few tens of nanometers for magnetic transition metals), which brings about new magnetization processes, different from those occurring in bulk materials. Both from the point of view of the implementation of actual devices and of the progress in understanding this new phenomenology, it is important to design reliable, repetitive nanostructuring processes, combining good resolution in the nanometer scale with a minimum influence of chemical, structural and morphological imperfections on the final magnetic properties. These issues are crucial because those defects are generally uncontrolled and they might play a fundamental role in the magnetization mechanisms of nanoelements. Consequently, it is highly desirable to customize simple series of well controlled nanoelement arrays exhibiting magnetization processes independent of features arising from the imperfections introduced upon nanostructuring.

This thesis studies the influence on the magnetization processes of the structural features of different arrays of nanostructures with two types of motifs, nanowires and antidots (non magnetic holes), fabricated in epitaxial Au (001)/Fe (001)/Mg (001) films, 25 nm thick approximately, grown by Pulsed Laser Deposition (PLD). This work includes a thorough task of fabrication of the arrays by means of different techniques, Focused Ion Beam (FIB) and Electron Beam Lithography (EBL) using either negative or positive resist, as well as a detailed structural and chemical characterization of the films and the arrays with a wide variety of techniques: X-ray Diffraction and Reflectometry (XRD and XRR), Atomic Force Microscopy (AFM), Scanning Electron Microscopy (SEM) and X-ray Photoelectron Spectroscopy (XPS).

The magnetization processes of the nanowires, with widths and interwire separation between 100 and 1000 nm, were studied by means of Magnetooptic Kerr Effect (MOKE) and Vibrating Sample Magnetometer (VSM). Ferromagnetic Resonance (FMR) measurements were also carried out to analyse the eventual existence of anisotropy contributions different from the magnetocrystalline and shape anisotropy inherent to the nanowires. The experimental results indicate that their reversal processes evolve from wall pinning, at low angles between the applied field and their long axis, to basically uniform magnetization rotation, at high angles. This behaviour can be described in terms of single spin configuration, thus ruling out the formation of multidomain structures even at high angles. The ability of achieving those high quality and well controlled nanowires allowed to develop an analytical model taking into account just the intrinsic Fe properties and the shape and dimensions of the wires. This simple approach provides a very good qualitative and quantitative agreement with the experimental results, thus evidencing the relatively poor role on their magnetization processes of other extrinsic factors and, in agreement with the ferromagnetic resonance results, of other eventual anisotropy energy contributions.

Antidots arrays constitute the second type of nanostructures studied in this thesis. These arrays were fabricated by Focused Ion Beam (FIB) and Electron Beam Lithography (EBL) on different Au/Fe/MgO thin films, forming square lattices of cylindrical holes, with diameter and separation ranging from 200 to 2000 nm and with the diagonal of the lattices coincident with the easy magnetocrystalline axes of the Fe films, (100) and (010). The magnetization inhomogeneities, appearing at the lateral surface of the antidots to minimize the dipolar energy, induce an internal shape anisotropy characterized by easy directions along the diagonal, thus reinforcing the magnetocrystalline anisotropy of the films. The magnetic characterization of the antidots, carried out by magnetooptic Kerr effect, was focused on the dependence of the coercivity on the diameter and separation of the arrays. As a main result, the coercivity of the arrays is up to a factor of 10 above that of the films and increases sharply with decreasing separation, although it also presents a relatively strong dependence on the specific coercivity value of the films on which they were fabricated. A general scaling of the coercivity is evidenced by considering the percentage of the magnetic material in the array around the antidots that forms the inhomogeneous structures, evaluated from the magnetostatic correlation length.

In summary, this thesis has shown the ability to produce high quality thin films and nanostructures offering a unique opportunity to study them as model systems. Although different fabrication processes were employed, the optimization of the parameters along each one of them allowed to produce arrays of nanowires and antidots whose magnetic properties depend almost exclusively on their morphology and characteristic dimensions, with minimum influence of the imperfections inherent to the different fabrication routes.

1

Introduction

As early as the 1950s, researchers had already envisioned the enormous technological potential of magnetic thin films for applications as sensors and information storage devices. Louis Néel made a number of contributions in the late 1950s and 1960s to the understanding of the phenomenology of magnetic thin films, mainly related with the Néel wall, surface anisotropy, and exchange anisotropy [1]. However, it was soon realized that difficulties in controlling sample quality, often due to the inevitable chemical contamination resulting from the inadequate vacuum techniques available for thin film growth and processing, limited the ability to control the thin films properties and to perform reliable experiments in the search for modified properties. Despite advances in surface science techniques and thin film growth it was only in the late 1990s that the early dreams of a new technology began to be truly fulfilled.

As the characteristic size of a magnetic system approaches key length scales, such as the domain wall width or exchange length, new magnetic properties arise. Before the single domain limit is reached, the spin configuration of small elements is strongly modified. A lot of research has been motivated by the demand for higher recording density and new components for sensing applications. Much effort has been recently devoted to fabricate patterned systems based on self-organization [2, 3] and lithography techniques [4, 5]. Beyond this technological motivation, the ability to achieve high quality and well controlled artificial nanostructures offers a unique opportunity to improve our understanding of low dimensional magnetism.

Since the 1990s different lithography techniques such as optical, electron beam, X-ray or extreme ultraviolet lithography [6] and Focused Ion Beam [7], have been substantially improved. These techniques provide very good control during the fabrication of nanoelements, with a very narrow distribution of shapes, sizes and distances. This improvement enables to fabricate large arrays of nanoelements with a reduced dispersion in the magnetic properties. A lot of studies about magnetic nanoelements were done in the last years. Figure 1.1 represents some important applications for these nanoelements discovered recently as magnetic sensors [8], logic gates [9], or racetrack memories [10].

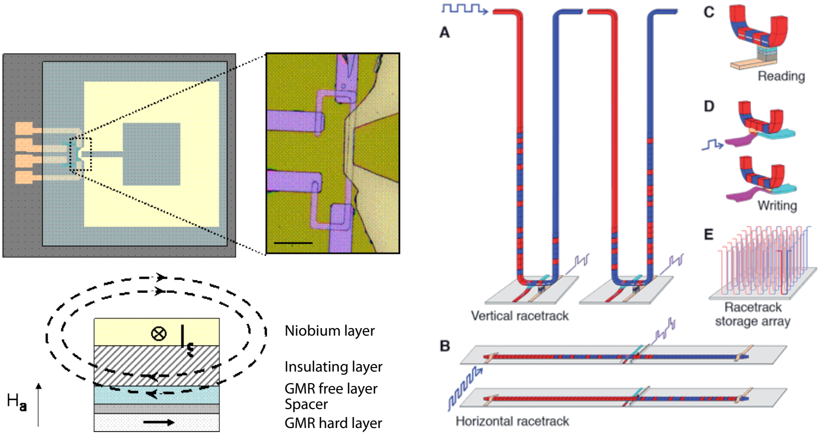

(a) (b)

Figure 1.1: Some of the applications of magnetic nanoelements: (a) magnetic sensors [8] and (b) racetrack memories [10].

This thesis is based on the study of two specific arrays of nanoelements fabricated by electron and focused ion beam lithography. In particular, it is focused in the study of planar nanowires and antidots lithographed in epitaxial Fe thin films grown onto MgO substrates.

Most of the applications of the magnetic nanoelements rely on their hysteresis behaviour. Since 1926, when the magnetization curves for the principal crystalline axis in bulk iron were published [11], an exhaustive study of the magnetic properties of iron was done, but until 1991 epitaxial iron thin films were not studied in detail [12]. The magnetization processes either for bulk materials or nanostructured thin films, result from the energy landscapes due to the competing energy terms which include exchange, magnetocrystalline anisotropy and magnetostatic energy among others. The high saturation magnetization of Fe provides the possibility to have strong magnetostatic effects in artificially made nanostructures. On the other hand, epitaxy provides a highly ordered crystalline structure, which, in combination with the relatively high magnetocrystalline anisotropy of Fe, leads to a very well defined configuration of magnetization easy and hard axes.

This thesis presents the study of the magnetization reversal processes of artificial nanostructured arrays, nanowires and antidots, lithographed on very high crystalline quality epitaxial Fe (001) thin films grown onto MgO substrates by means of pulsed laser ablation. These arrays of nanostructures were lithographed with very good control of the lithography parameters and with negligible influence on their magnetic properties by the imperfections generated along the fabrication process. The magnetic characterization of this nanostructures was focused on the dependence of the hysteresis behaviour on their morphological dimensions.

The thesis is divided into five sections organized as follows:

Chapter 1: Introduction and motivation of the study of the magnetic properties of magnetic nanostructures.

Chapter 2: A general description of the experimental techniques related to thin film deposition, structural, morphological, chemical and magnetic characterization and to the lithographic procedures is presented. The properties of the epitaxial Au (001)/Fe (001)/MgO (001) thin films on which the nanostructures were lithographed are also discussed.

Chapter 3: The fabrication of Au/Fe/MgO planar nanowires with different aspect ratios by FIB and EBL is reported. Structural and morphological results are discussed in terms of the optimization of parameters for each lithographic technique. The dependence of the magnetization reversal processes on the nanowires width and separation is analysed.

Chapter 4: The fabrication of Au/Fe/MgO antidots with different diameters and distances between them by FIB and EBL is reported. The magnetization reversal processes of the antidots are discussed in connection to their morphological features.

Finally the main conclusions of this study are summarized.

Bibliography

[1] J. M. D. Coey, *“Louis Néel: Retrospective (invited)”* Journal of Applied Physics **93** (10) 8224–8229 (2003).

[2] A. Fert and L. Piraux, *“Magnetic nanowires”* Journal of Magnetism and Magnetic Materials **200** (1-3) 338–358 (1999).

[3] O. Fruchart, *“Epitaxial self-organization: from surfaces to magnetic materials”* Comptes Rendus Physique **6** (1) 61–73 (2005).

[4] P. Vavassori, V. Bonanni, G. Gubbiotti, A. Adeyeye, S. Goolaup and N. Singh, *“Cross-over from coherent rotation to inhomogeneous reversal mode in interacting ferromagnetic nanowires”* Journal of Magnetism and Magnetic Materials **316** (2) e31–e34 (2007).

[5] M.-Y. Im, L. Bocklage, P. Fischer and G. Meier, *“Direct observation of stochastic domain-wall depinning in magnetic nanowires”* Physical Review Letters **102** (14) 147204 (2009).

[6] T. Ito and S. Okazaki, *“Pushing the limits of lithography”* Nature **406** (6799) 1027–1031 (2000).

[7] S. Reyntjens and R. Puers, *“A review of focused ion beam applications in microsystem technology”* Journal of Micromechanics and Microengineering **11** (4) 287–300 (2001).

[8] M. Pannetier, C. Fermon, G. Le Goff, J. Simola and E. Kerr, *“Femtotesla Magnetic Field Measurement with Magnetoresistive Sensors”* Science **304** 1648–1650 (2004).

[9] D. A. Allwood, G. Xiong, C. C. Faulkner, D. Atkinson, D. Petit and R. P. Cowburn, *“Magnetic domain-wall logic”* Science **309** 1688–1692 (2005).

[10] S. S. P. Parkin, M. Hayashi and L. Thomas, *“Magnetic domain-wall racetrack memory”* Science **320** 190–194 (2008).

[11] K. Honda, S. Kaya and Y. Masuyama, *“On the magnetic properties of single crystals of iron”* Nature **117** 753–754 (1926).

[12] J. M. Florczak and E. D. Dahlberg, *“Magnetization reversal in (100) Fe thin films”* Physical Review B **44** (17) 9338–9347 (1991).

2

Experimental techniques and thin films

2.1 Growth Techniques

During this thesis two Physical Vapour Deposition (PVD) techniques have been used for the growth of the thin films, Pulsed Laser Deposition (PLD) and Molecular Beam Epitaxy (MBE)

MBE is a sophisticated growth technique extensively used nowadays to grow a wide variety of materials because of its ability to produce very high quality thin films of excellent crystallinity and very high purity. Using a single crystal as a substrate it is possible to find adequate conditions for which the growth is epitaxial, in such a way that the crystalline structure of the layer is determined by the substrate. The MBE growth can be performed with a Knudsen cell in the regime of very slow deposition rate, 1-5 Å/min, around 1 ML/min.

PLD technique consists of a three steps process: laser-material interaction, plasma expansion and film nucleation and growth. A high power pulsed laser is focused onto a target material that is going to be ablated; the energy density in the focus point is high enough to create the plasma. This plasma expands in the vacuum and it is deposited on a substrate placed in front of the target, obtaining in this way the growth of a thin film (figure 2.1). Generally the film thickness is proportional to the number of pulses of the laser.

For low laser fluency (≈ 0.35 J/cm^2) and/or low absorption at a given wavelength, the laser pulse would simply heat the target, with the emission of an ejected flux due to thermal evaporation of the target material. As the laser fluency is increased, an ablation threshold is reached for which the laser energy absorption is higher than that needed for evaporation. The ablation threshold is dependent on the absorption coefficient of the material and, thus, on the laser wavelength. At such high fluencies, absorption by the ablated species also occurs, resulting in the formation of plasma at the target surface. With appropriate choice of ablation wavelength and absorbing target material, high-energy densities are absorbed by a small volume of material, resulting in the emission of target material species that is not dependent on the vapour pressures of the constituent elements.

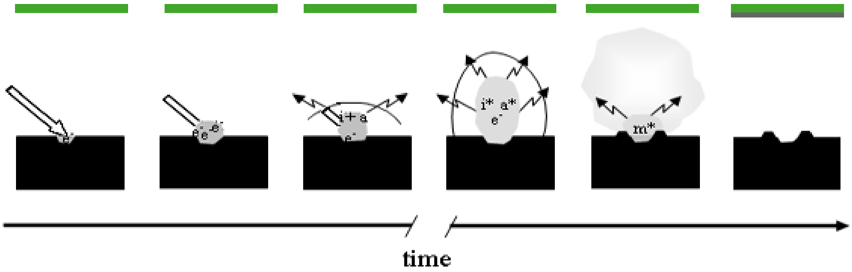

Figure 2.1: Sequence of events following the striking of a focused short laser pulse (ca. 5 ns) on the surface of a solid sample. The thick arrow represents the laser pulse and its length the pulse duration. e^-, free electrons; i, ionic species; a, atomic species; m, molecular species; *, excited species [1].

With this technique it is possible to deposit almost any material, with a congruent transfer of stoichiometry from target to film. In most PLD systems, a pulsed laser with wavelength in the ultraviolet region ($\lambda = 193$ nm) is used due to the suitability for the growth of insulating materials, specially those with wide energy gap. In the case of metals deposition this wavelength effect is not so important because they have no energy gap, so that a laser with visible radiation can be used (double frequency Nd-YAG $\lambda = 532$ nm).

Many experimental PLD systems developed to prepare oxide thin films, and, in particular, extensively used for high T_c superconductors, have a base pressure in the high vacuum range (10^{-7} mbar). In this case, deposition is performed under a controlled gas atmosphere with a partial pressure two orders of magnitude higher than the base pressure [2]. However, in the case of deposition of very pure metallic materials, which are more reactive, it is advised to work under ultra high vacuum (UHV) conditions to avoid any chemical modification of the material due to the residual atmosphere.

The system shown in figure 2.3 is the one used in this thesis for the growth of Au/Fe/MgO (001) films. The single crystal MgO (001) substrates

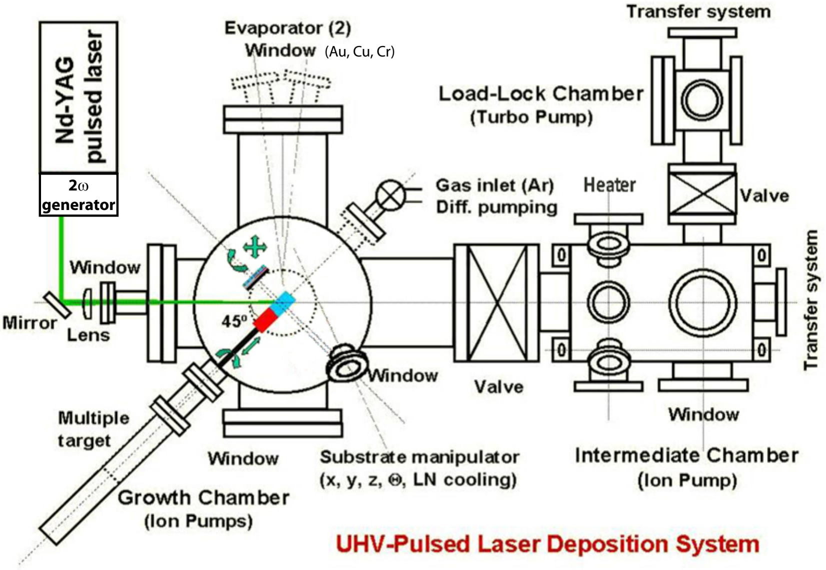

Figure 2.2: Scheme of the PLD system.

of 5 mm×5 mm×0.5 mm size were supplied by MaTeck GmbH, Germany, with an orientation accuracy $\leq 0.5^{\circ}$ and an average surface roughness of 1 nm ($R_{\text{max}} \leq 5$ nm).

The MgO substrates are placed in a set of sample holders specially design during this thesis. They are fabricated with tantalum (Ta) and molybdenum (Mo), which are refractory metals with high melting temperatures and very low vapour pressures [3], so that the contamination by the sample holder during the thermal annealing is minimized. The sample holders are placed onto the stainless steel holder specially designed for this system to allow sample transfer under vacuum. In figure 2.4 a scheme of the sample holder is shown. Firstly, a Ta disc 0.25 mm thick (2) is placed to avoid contact between the substrate and the stainless steel holder (1), then a Mo disc 0.5 mm thick (3) with a square of 5.5 mm in the centre where the substrate is placed, and finally another Ta disc (4) with

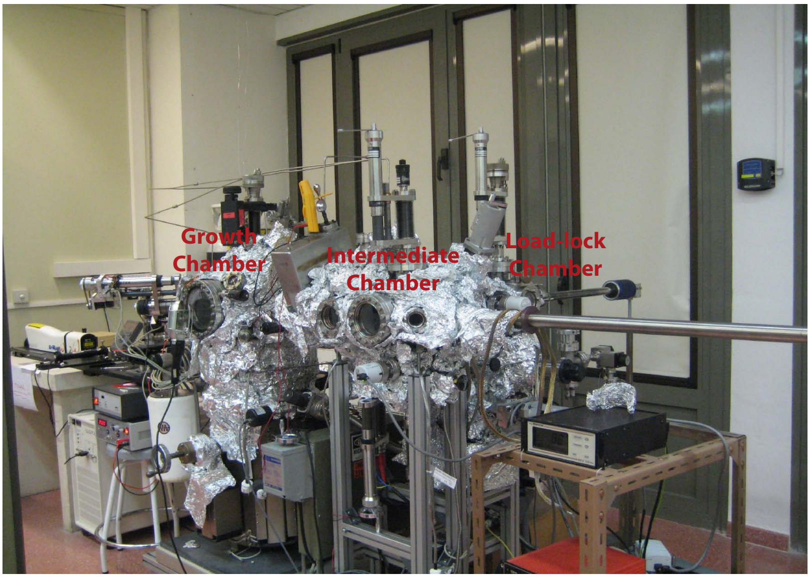

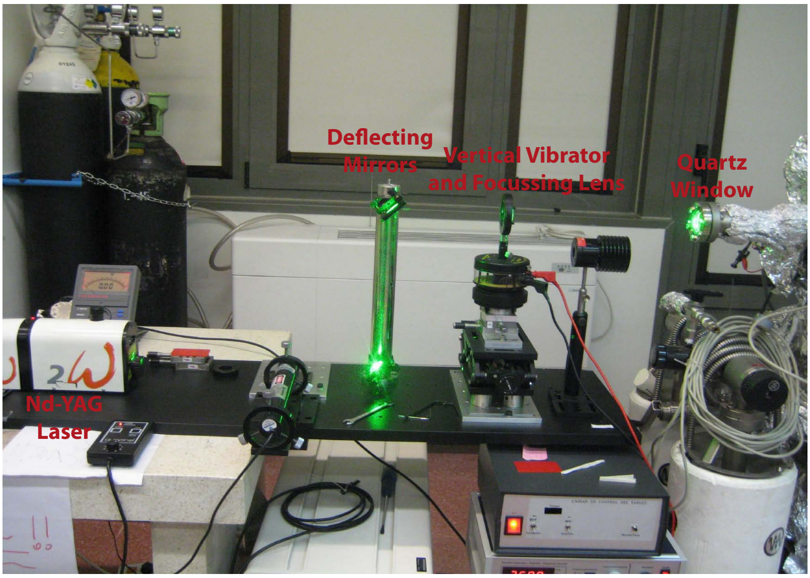

Figure 2.3: UHV Pulsed Laser Deposition system used in this work (top) and Nd-YAG laser, deflecting mirrors, vertical vibrator unit and focussing lens (bottom).

an square or patterned mask on top of the substrate. This last disc is used to hold down the substrate and as a shadow mask when a pattern is used.

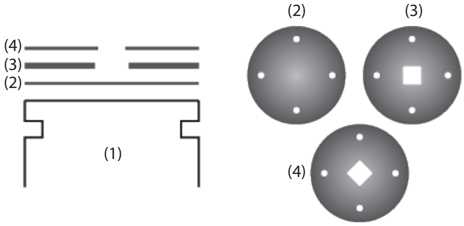

Figure 2.4: Side and top views of sample holders used for PLD growth.

The PLD system is a home made equipment that consists of three separate chambers:

I. The load-lock chamber that is used to load the substrates inside the system from atmosphere,. This chamber has a sample parking stage where three substrates can be loaded at the same time. It is pumped with a turbo molecular pump backed with a rotatory pump reaching a base pressure of $5 \cdot 10^{-8}$ mbar.

II. The intermediate chamber, which has two parking stages: one for samples once the holders are transferred from the load-lock chamber, and another for targets, so that it is possible to exchange both samples and targets without venting the growth chamber. This chamber has also a radiative heater to do thermal treatments of the sample. It is pumped by an ion pump achieving a base pressure below $1 \cdot 10^{-9}$ mbar.

III. The growth chamber, also pumped by an ion pump, has a base pressure of $8 \cdot 10^{-11}$ mbar. Inside this chamber there is a Fe target for PLD deposition, and two Knudsen cells with different metals (Au, Cr) for MBE evaporation.

The commercially available MgO substrates delivered by Mateck present high quality in terms of surface defects, roughness and surface morphology. Thus, to reduce any possible surface damage, MgO substrates are mounted "as-received" without any acetone or ethanol ultrasonic cleaning. They were outgassed at 150-200 ^{o}C for 30 minutes by placing them in front of the heater in the intermediate chamber. To avoid W contamination of the substrate a quartz tube is placed between the heater and the sample holder. Then the substrate is transferred into the growth chamber.

A high power laser beam is focussed onto the Fe target surface after passing through a quartz window to produce the ablation process. The laser used is a Quantel Brilliant Nd-YAG with a second harmonic 2ω generator ($\lambda = 532$ nm, $\tau = 4$ ns), with a repetition rate of 10 Hz and a maximum energy per pulse of 180 mJ.

In order to achieve the growth of high quality epitaxial Fe films it is mandatory to optimize the parameters involved in the ablation process. The most important problem in PLD growth is the droplet emission whose density was minimized when the laser power was set to 0.25 W.

Another important issue to be considered is the homogeneous erosion of the target [4]. A high purity Fe (99.99%) Johnson Mattey Ltd. target with cylindrical shape has been used so that uniform erosion is done by scanning the target surface across the laser beam upon translating and rotating along its length, respectively. An additional third scan shifts the laser beam vertically on the target surface by means of a vibrator on which the focussing lens is mounted.

The ablation deposition rate is accurately controlled by the stability of the laser power during the film growth. Most of the films studied in this thesis were prepared by using a laser power of 0.25 W providing a rate of 4 Å/min. Fe/MgO films 24 nm thick are grown at room temperature for 1 hour.

It is well known that the growth mode and crystalline quality of Fe depend on the deposition temperature [5]. Fe epitaxial films on MgO (001) substrates are obtained for RT growth and subsequent annealing at 400 ^{o}C. In this particular case, the sample was annealed for 25 minutes.

In addition, a very thin capping layer of Au has been deposited to preserve Fe chemical purity and prevent its oxidation. This Au layer is thermally evaporated by a Knudsen cell in MBE regime. The deposition rate is extremely stable and equal to 5 Å/min for the parameters used. The thickness of the Au layer was 3 nm.

2.2 Structural and chemical characterization

2.2.1 X-ray Diffraction and Reflectometry

X-ray diffraction (XRD) is a very suitable technique to provide information about crystalline structure because the wavelength of the radiation is of the same order of magnitude that the characteristic distance between the atoms of a solid.

Two different X-ray sources have been used for the diffraction measurements performed in this thesis:

I. A laboratory Bruker D8 Advance diffractometer with Cu K_α radiation ($\lambda = 1.5405$ Å) located at ICMM. The sample stage has a four circles Eulerian cradle and three translations x, y, z axes (figure 2.5(a)):

   - ω Angle between the direction of the incoming beam and the sample plane.
   - 2θ Angle between the incoming light and the inspected diffraction directions.
   - ϕ Angle defining the rotation around the axis normal to the sample plane.
   - χ Angle of the tilt obtained by rotating around a horizontal axis of the sample plane.

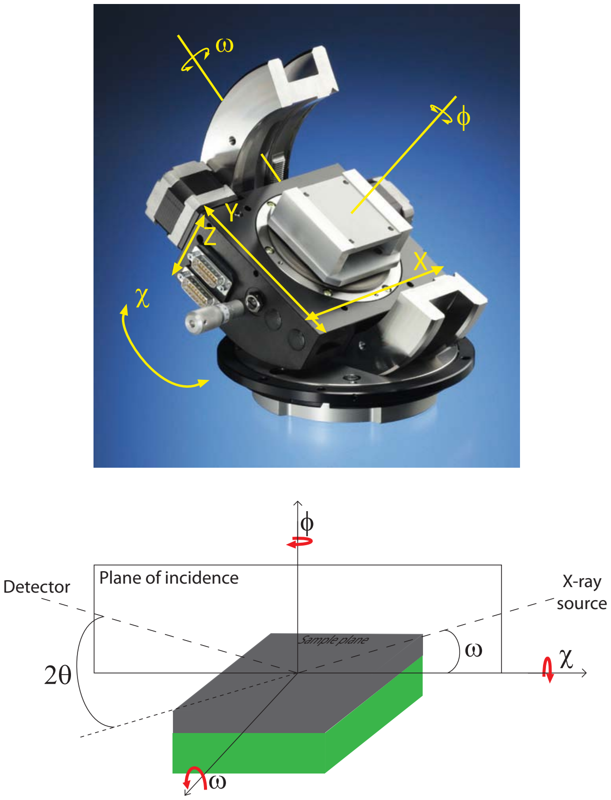

Figure 2.5: Sample stage with Eulerian cradle.

II. Synchrotron radiation of wavelength $\lambda = 0.8857$ Å from the Spanish beamline (SpLine, BM25) at European Synchrotron Radiation Facility (ESRF).

A diffraction pattern is obtained by measuring the intensity of scattered waves as a function of scattering angle. Very strong constructive interference from crystallographic planes (hkl) of the lattice is obtained in the diffraction pattern when scattered waves satisfy the Bragg condition:

$$2d_{hkl}\mathrm{sin}\theta = \mathrm{n}\lambda \tag{2.1}$$

where d_{hkl} is the interplanar separation, θ the angle of the incident and the diffracted beam with the planes and λ the wavelength of the radiation (figure 2.6).

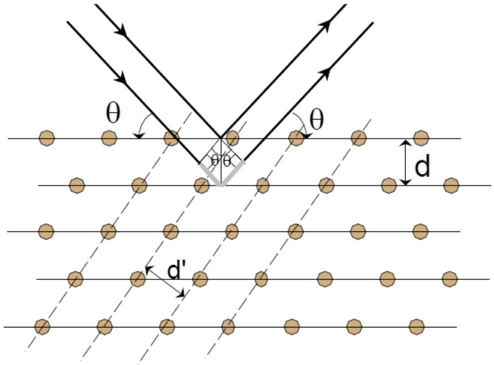

Figure 2.6: Bragg reflection from a group of planes separated a distance d.

The Bragg-Brentano configuration is used to determine the interplanar distance of the planes parallel to the sample surface (figure 2.7). This type of scan is a symmetric θ-2θ ($\omega = \theta$) where the angle θ of the incoming beam with respect to the sample surface is varied, while simultaneously keeping the detector at an angle of 2θ with respect to the incoming beam.

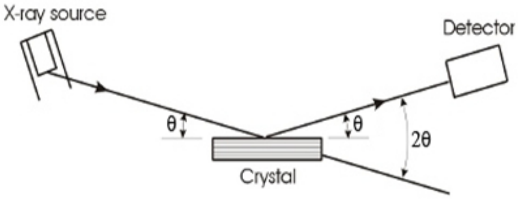

Figure 2.7: Symmetric θ-2θ scan, Bragg-Brentano configuration.

Figure 2.8 displays the Bragg-Brentano scan of the Au/Fe/MgO (001) thin film measured with $\lambda = 0.8857$ Å at SpLine beamline (ESRF). The

Bragg peak at $2\theta = 36.04^o$ from the Fe (002) crystallographic planes, provides an interplanar distance of $d_{Fe} = 2.861$ Å in good agreement with the bulk Fe lattice constant $a_{Fe} = 2.860$ Å. The absence of any other (hkl) diffracted beams confirms the preferential growth along (001) direction. The same discussion applies to Au layer, which is also (001) textured. The presence of well defined and sharp finite size oscillations around Fe (002) and Au (002) reflections is a good indication of the high crystallinity of the Au/Fe/MgO (001) films, which has to be verify.

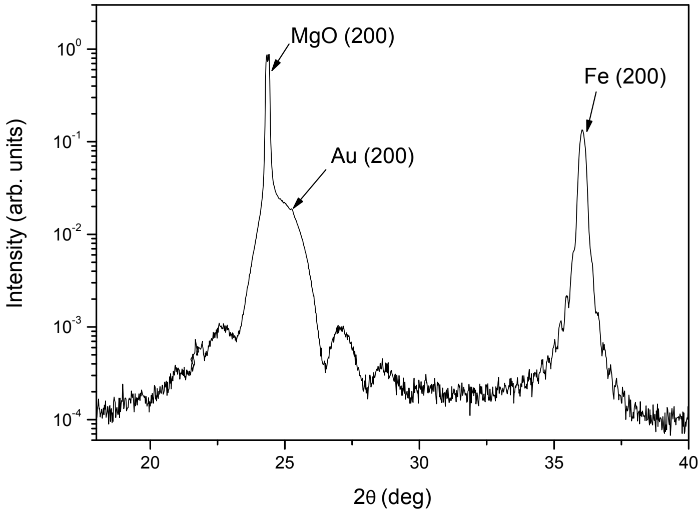

Figure 2.8: θ-2θ diffraction pattern from Au/Fe/MgO (001) thin films measured by synchrotron radiation ($\lambda = 0.885$ Å).

X-ray reflectometry (XRR) measurements are based on a special type of symmetric θ-2θ scans. Its principle is the same as the θ-2θ scan described above, except for the fact that the measurement is performed at grazing angles. In a standard θ-2θ experiment the distance between crystallographic planes, which is of the order of 0.5-5 Å, is measured. However, in XRR experiments the scattering of the X-rays now does not occur at the individual atomic planes, but at the interface between the layers in the film due to their difference in electron density. This type of measurement does not only allow to calculate the distance between adjacent layers and the total thickness of a thin film, but also to determine the surface and interfaces roughness.

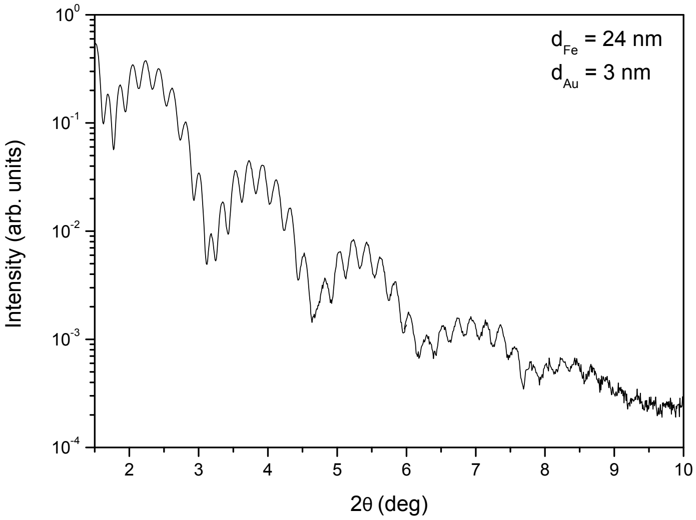

Figure 2.9: X-Ray reflectivity of the Au/Fe/MgO (001) thin film ($\lambda = 0.885$ Å).

X-ray reflectometry measurements of Au/Fe/MgO (001) thin films are shown in figure 2.9. The well defined oscillations and the "moderate" decay of the reflected intensity confirms the abrupt and flat nature of the surface and the interfaces. Besides, the superposition of long and short period oscillations from the Fe/Au and MgO/Fe interfaces, respectively, can be observed. A linear dependence of $\sin\theta_{\mathrm{i}}$ interference order $\mathrm{n_i}$is obtained from the angles θ_i at which each maximum appears. The linear fit of these values by a least square method provides a slope, which is inversely proportional to the film thickness, d ($\mathrm{m} = \mathrm{n}/\sin\theta$, $d = \lambda/(2\mathrm{m})$) (Eq. 2.1). Thus, this analysis yields a total thickness of 27 nm, for the Au/Fe/Mgo (001) thin films, where $\mathrm{d_{Fe}} = 23.8$ nm and $\mathrm{d_{Au}} = 3.2$ nm.

The film thickness was also calculated by SupReX, a software developed by E. Fullerton and I. K. Schuller [6–8]. This program fits the X-ray reflectometry pattern to obtain the film thickness and the interfaces roughness. It uses a kinematic model for the diffraction pattern at high angle and a dynamic model (Born approximation) based on optical theories that do not consider the crystalline structure for the low angle regime.

Figure 2.10 displays the experimental data (black) and the theoretical (red) XRR pattern simulated for a single Fe and Au bilayer. The excellent agreement of both curves reproduces not only the position of the maxima, but also the superposition of the long and short period oscillations and the reflectivity decay. The best fit yielded thickness values of $d_{Fe} = 23.3$ nm and $d_{Au} = 3.2$ nm, in very good agreement with the previous results. In addition, the roughness of the interfaces MgO/Fe, $\sigma_{MgO/Fe} = 1.9$ Å, and Fe/Au, $\sigma_{Fe/Au} = 1.4$ Å, are obtained.

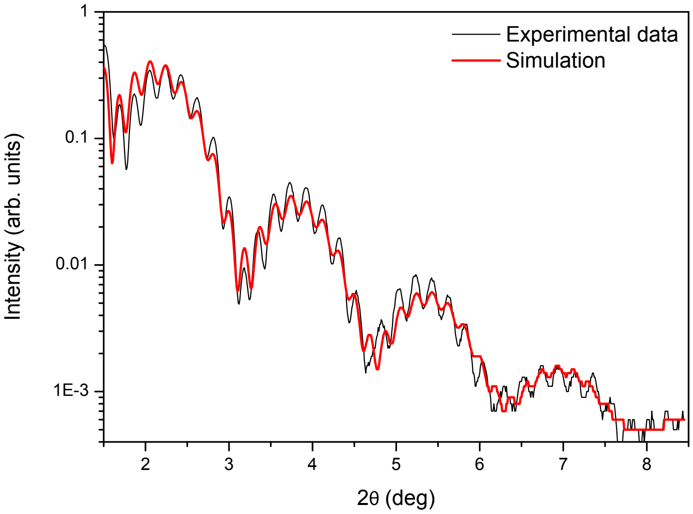

Figure 2.10: X-ray reflectivity of the thin film with the simulation made with SupReX program [6–8] ($\lambda = 0.885$ Å).

A full crystalline structural characterization of the Au/Fe/MgO (001) films requires to study the existence of in-plane domains. This analysis would allow to conclude whether the film is highly textured or epitaxial. In the latter case, the relationship of the crystallographic direction with the substrate are to be determined. This is done by measuring ϕ scans for asymmetric reflections of substrate and thin film, which consist of the rotation of ϕ at fixed χ, ω and θ angles. These experiments were performed with the 4 circle D8 Advance system at ICMM, with a Cu K_α X-ray source (figure 2.5(a)). ϕ-scans for the planes (110) of the Fe and MgO were measured with $\chi = 45^o$ and $2\theta = 44.77^o$ and $2\theta = 62.50^o$ for Fe and MgO, respectively.

Figure 2.11(a) shows the epitaxial relationship of MgO and Fe lattices in accordance with bulk constant values ($a_{MgO} = 4.203$ Å and $a_{Fe} = 2.860$ Å, $a_{Fe} \approx a_{MgO}/\sqrt{2}$) and the mismatch ($(a_{Fe} - a_{MgO}/\sqrt{2})/a_{MgO}/\sqrt{2} = -0.038$). Due to this small mismatch difference one might expect the epitaxial growth of Fe onto MgO (001) by means of an in-plane 45^o rotation of the lattices. This assumption is experimentally confirm as shown in figure 2.11(b), in which the Fe (110) asymmetric reflections have four-fold symmetry indicating the presence of a single in plane domain. In addition, Fe (110) peaks are 45^o apart from the MgO (220) ones, in agreement with the expected in-plane rotation of lattices with respect to one another. In summary, the XRD characterization presented so far allows to conclude the growth of Fe (001) on MgO (001) following the Fe (001)[100]//MgO (001)[110] epitaxial relation.

From previous wide angle XRD results, the Au capping layer of the Au/Fe (001)/MgO (001) thin films is highly textured. One might also expect a perfect epitaxy on Fe (001) films due to their similar in-plane lattice constants ($a_{Au} = 4.08$ Å$\approx a_{MgO}$) and mismatch $(a_{Au}/\sqrt{2} - a_{Fe})/a_{Fe} = 0.009$) by an additional 45 ^{o} rotation in registry with the MgO lattice. However, ϕ-scans of Au asymmetric reflections are difficult due to the very small thickness of this capping layer, which intensity is would be hindered by the strong signal from the MgO substrate.

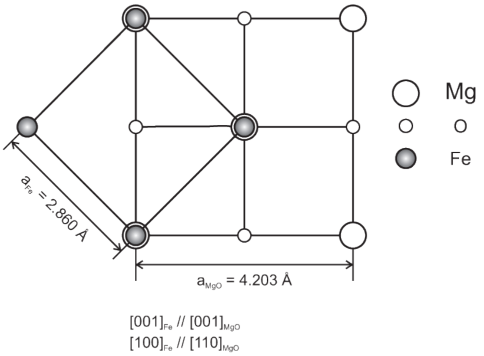

(a)

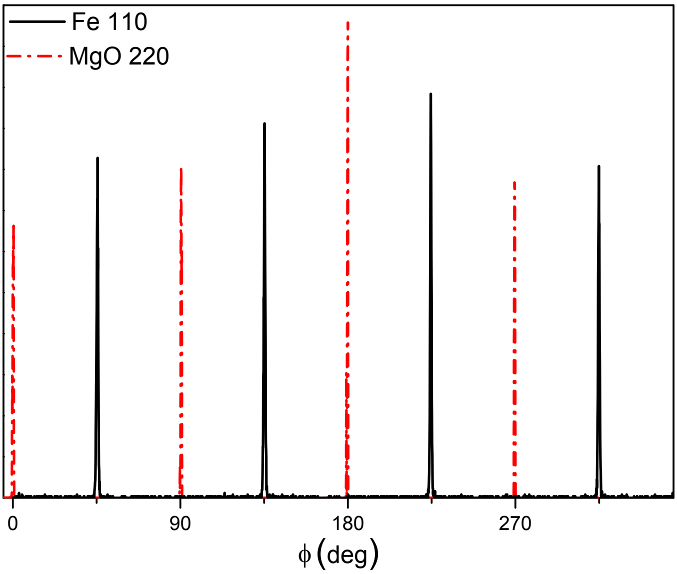

(b)

Figure 2.11: (a) Schematic view of in-plane Fe and MgO lattices and epitaxial relationship: 45^o rotation of the Fe lattice respect to the MgO one and (b) asymmetric reflections for the MgO and Fe.

Synchrotron based XRD experiments combining high photon flux and angle resolution are mandatory to get insight on the crystalline structure of the Au capping layer.

In addition to the peak position in a θ-2θ scan, the width of the peak under investigation also contains valuable information. In case of a perfect crystalline film, the width of the interference peak (as a function of θ) is inversely proportional to its thickness. The full width at half maximum (FWHM) of the peak is given by the Scherrer formula [9]:

$$\mathrm{FWHM} = \frac{0.94\lambda}{< \mathrm{L_c} > \cos(\theta_\mathrm{B})} \tag{2.2}$$

where FWHM is expressed in radians, λ is the wavelength of the X-rays, $< \mathrm{L_c} >$ is the thickness of the film and θ_B the Bragg angle of the reflection. A non-perfect crystal can be divided into different crystalline domains (or grains) with slightly different orientations. This is the case when long-range stacking faults and other extended defects are present in the sample, and $< \mathrm{L_c} >$ in the Scherrer formula is related to the out of plane crystallite grain size.

The FWHM of the Fe (002) reflection in the diffraction pattern displayed in figure 2.7 at $\theta_\mathrm{B} = 18.02^o$ is 0.27^o. According to the Scherrer formula (Eq. 2.2) the thin film has a perpendicular grain size of $< \mathrm{L_c} >= 18.56$ nm. This value can be understood as the coherence length of the out of plane lattice constant. As it will be shown in section 2.2.2, the mismatch at the interfaces generates a distortion of the Fe lattice, and, consequently, $< \mathrm{L_c} >$ value must be smaller than the real Fe film thickness evaluated by XRR.

Another type of scan closely related to a θ-2θ scan is a rocking curve (RC) scan, from which it is possible to determine the mean spread in orientation of the different crystalline domains of a non perfect crystal. In order to obtain a rocking curve the detector position 2θ is fixed at the Bragg angle of the corresponding reflection and the scan is then acquired by varying the angle θ by a range $\Delta\omega$ around its central position. For $\Delta\omega = 0$ the sample and detector are at the exact positions for Bragg condition. The RC corresponding to Fe (002) reflection have a FWHM of 0.57^o and 0.71^o, when measures with synchrotron radiation (($\lambda = 0.885$ $\overset{\circ}{\mathrm{A}}$)) and Cu-K$_\alpha$ (($\lambda = 1.5405$ $\overset{\circ}{\mathrm{A}}$)), respectively. These values are well bellow the best ones reported in the literature for epitaxial Fe thin films [10], which demonstrates the excellence crystallinity of the Fe films grown in this thesis.

2.2.2 Reciprocal Space Maps

Consider a set of points $\vec{R}$ constituting a Bravais lattice. The reciprocal lattice can be characterized as the set of wave vectors $\vec{K}$ satisfying

$$\mathrm{e}^{i\vec{K}\vec{R}} = 1 \tag{2.3}$$

For any family of crystal planes separated by a distance d, there are reciprocal lattice vectors perpendicular to the planes, the shortest of which has a length $2\pi/d$.

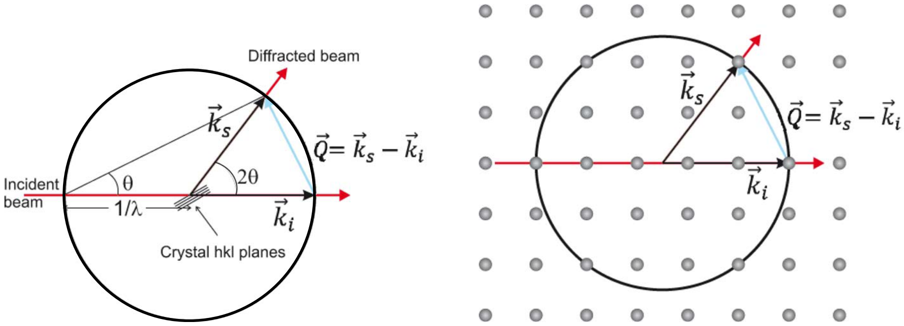

Figure 2.12: Ewald's geometric model. When the Ewald's sphere intersects a point of the reciprocal lattice, a vector to this point from the centre of the sphere represents the diffracted beam $\vec{k_s}$.

A sphere of radius $\left|\vec{k_i}\right| = 2\pi/\lambda$ centred at a point defined by the incident vector $\vec{k_i}$ with respect to the origin of the crystal, known as Ewald's sphere (figure 2.12), provides a very easy geometric interpretation of the directions of the diffracted beams. When the end of the diffracted beam wave vector $\vec{k_s}$ lies on the Ewald's sphere and the scattering vector $\vec{Q} = \vec{k_s} - \vec{k_i}$ belongs to the reciprocal lattice, $\vec{Q} = h\vec{b_1} + k\vec{b_2} + l\vec{b_3}$, a diffracted beam is generated and the family of planes $[h, k, l]$ are in Bragg's condition (h, k, l are the Miller indexes of the scattering planes, and $\vec{b_1}$, $\vec{b_2}$, $\vec{b_3}$ form the base of the reciprocal space)

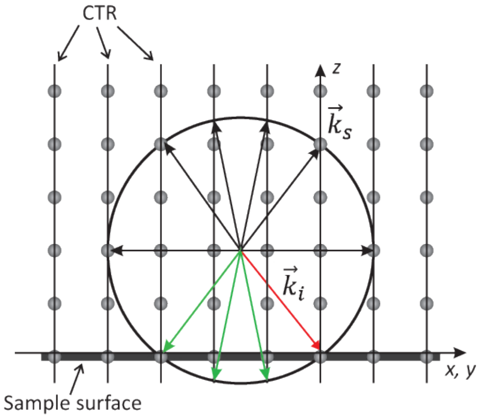

Figure 2.13: The incident wave vector $\vec{k_i}$ points to the origin of the reciprocal space, the wave vectors $\vec{k_s}$ lie in the cross sections between the Ewald sphere and the crystal truncation rods; the diffracted waves (green) penetrate into the sample and are not measurable in reflection geometry.

For diffraction purposes involving the surface (or thin film overlayer with different periodicity), for which the system is two-dimensional periodic (parallel to the surface), only the component of a wavevector parallel to the surface is conserved with the addition of a reciprocal net vector. As a consequence of the sharp truncation of the scattering system at the surface the reciprocal lattice points are replaced by rods in the reciprocal space, hence the name of Crystal Truncation Rods (figure 2.13) [11].

Reciprocal space maps have been measured at SpLine beamline (BM25)

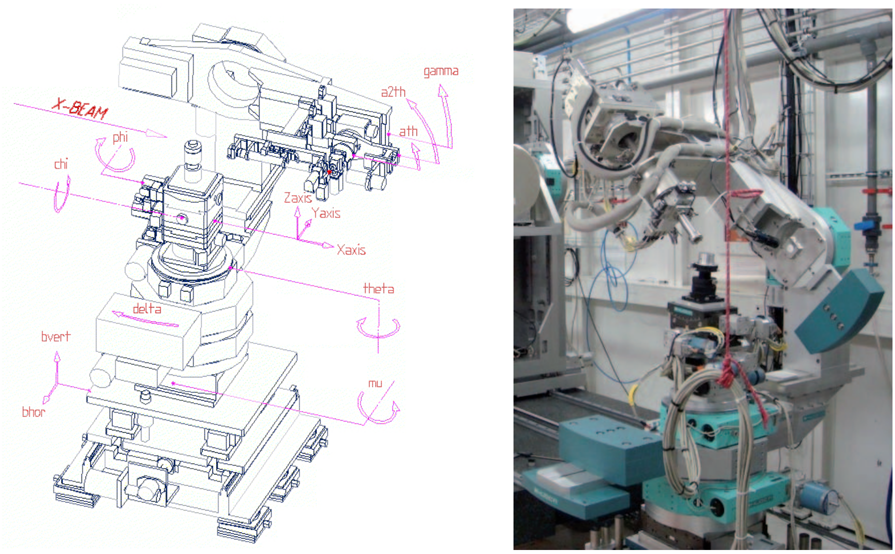

Figure 2.14: Scheme and picture of the six circle diffractometer installed at SpLine beamline (ESRF).

in the European Synchrotron Radiation Facility (ESRF). The branch B of this beamline is equipped with a single crystal diffraction endstation [12]. Figure 2.14, shows the six circle diffractometer in vertical geometry which allows to scan the reciprocal space: Three circles are dedicated to the sample motion (θ, χ, φ), two circles are dedicated to the detector motion (δ, γ) and the sixth one (μ) is coupled to the sample and the detector motion.

Therefore, it is possible to fix the values h and k of the $\vec{Q}$ vector, so that crystal truncation rod measurements are performed by varying l (l-scans). Reciprocal space maps (RSM) around a given reciprocal space point (h,k) are performed by changing Δh and Δk at a fixed value of l.

In the particular case of Au/Fe/MgO samples, the MgO (001) substrate was used as reference, so that all the (h,k,l,) values correspond to its lattice and not to the thin film one.

Each point of the reciprocal space corresponds to a group of atomic

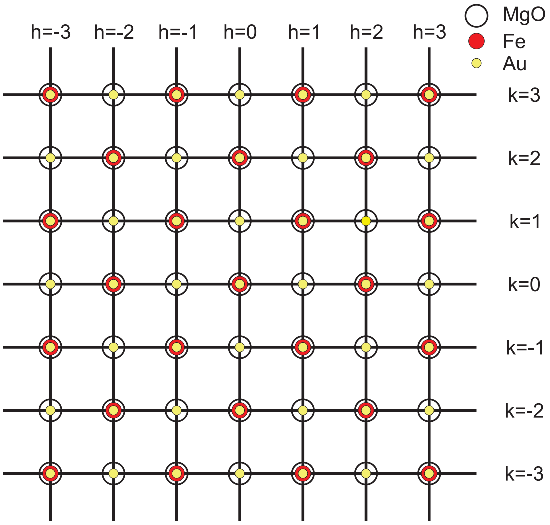

Figure 2.15: Scheme of the theoretical plane of reciprocal space for $l = 0$.

planes, as displayed in figure 2.15 for $l = 0$. For each l integer value the points of the MgO lattice are coincident with those of $l = 0$ (fig, 2.15). However, the case of Au planes the reciprocal space points expand with increasing l by a factor $l \cdot 1.03$ (l integer) due to the ratio $a_{MgO}/a_{Au} = 1.03$. Similarly, in the case of Fe planes the network expands with l by a factor $l = a_{MgO}/a_{Fe} = 1.47$. The almost identical lattice constant of MgO and Au makes it difficult to resolve two different reflections due to the overlapping of both MgO and Au peaks and the very strong signal of the MgO substrate. Therefore, Au reflection is to be measured in l-scans by increasing l.

The experimental set-up can not measure l-scans or reciprocal space maps for both h and k or l equal to zero. Figures 2.16(a) and 2.17(a) display the simulations of the l-scans made with AnaRod, which is a surface crystallographic code specially developed to describe the continuous intensity distribution along rods perpendicular to the surface taking the surface roughness into account properly [13]. From of these simulations signals from substrate (black line) and Au/Fe thin film (red line) as well

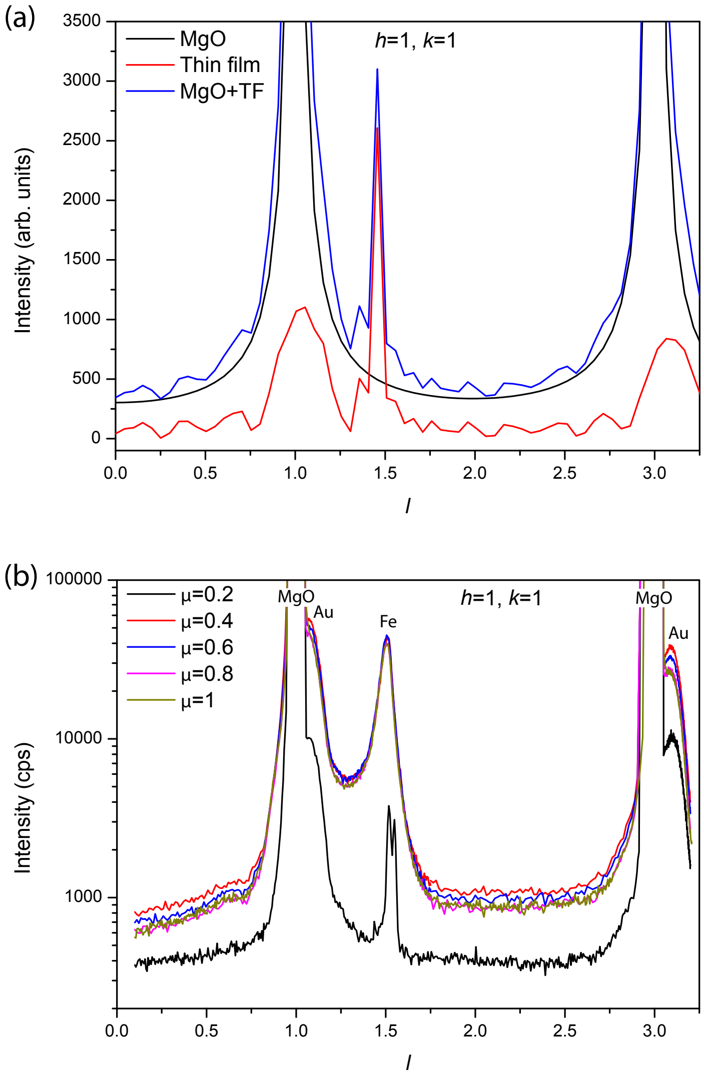

Figure 2.16: l-scans $(11l)$ (a) simulation with AnaRod program [13] and (b) experimental data for different incident angles.

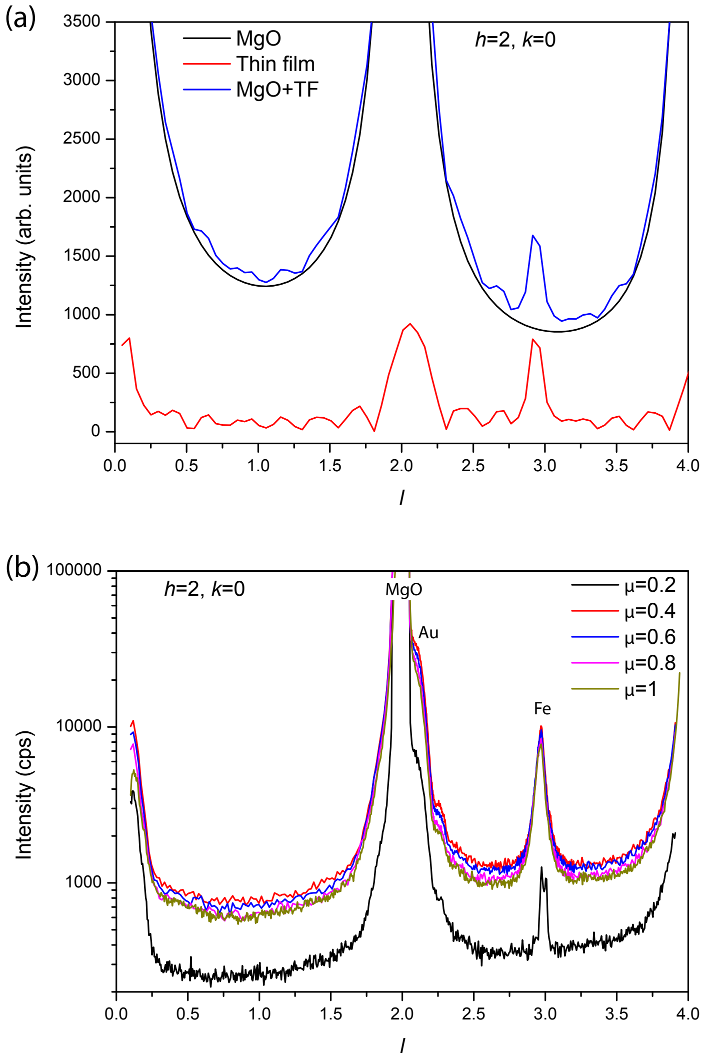

Figure 2.17: l-scans $(20l)$ (a) simulation with AnaRod program [13] and (b) experimental data for different incident angles.

as its sum can be extracted for comparison with the experimental results. Au reflections in the l-scan appear approximately at integer odd l values for $h = k = 1$ and even values for $h = 2,\ k = 0$; Fe reflections appear at $l = (2\mathrm{n} - 1) \cdot 1.47$ for $h = k = 1$ and $l = 2\mathrm{n} \cdot 1.47$ for $h = 2,\ k = 0$. The experimental l-scans readily shows a good agreement with the previous AnaRod simulations (figures 2.16(b) and 2.17(b))

Although Au reflections are on the high intensity tail of the MgO ones, they can be clearly resolved for all l values due to the extremely good experimental angular resolution (l-scans are measured in steps of $1.1 \cdot 10^{-3}$ reciprocal space units).

Figures 2.16(b) and 2.17(b) show the l-scans $(11l)$ and $(20l)$ for different incident angles, from 0.2 to 1.0 degrees. As the incident angle increases, X-ray penetration also increases and depth information is obtained. Surface sensitivity is mostly provided by lowest incident geometry.

The analysis of l-scans from Fe reflections taken at different incident angles indicates a modification of the Fe vertical lattice constant with depth. This fact is readily observed for the most grazing incidence ($\mu = 0.2^o$) l-scans, in which, for $h = k = 1$, the Fe reflection at $l = 1.5$ is split in two peaks. The first peak corresponds to the reflection observed at higher incident angles providing the lattice constant of deep Fe atomic layers ($c_{Fe} = 2.82$ Å) similar to the bulk Fe. However, there exist a second contribution associated with smaller lattice constant which points out the existence of vertical contraction in the outermost atomic layers of the film. At this incidence angle of $\mu = 0.2^o$, below the critical angle ($\theta_\mathrm{c} = 0.25^\mathrm{o}$), the penetration depth is about 2 nm in Fe.

Figure 2.18 shows a detail of the $h = k = 1$, $l = 1.5$ Fe reflection taken at incident angle $\mu = 0.2^o$. This peak is fitted with two gaussians with relative areas of 63.5% (A_1) and 36.5% (A_2). A_2 corresponds to Fe atomic planes near the Fe/Au interface. this means that 0.7 nm out of the 2 nm penetration depth correspond to the Fe region distorted due to the Fe-Au interface effects. These Fe atomic layers are contracted in the vertical

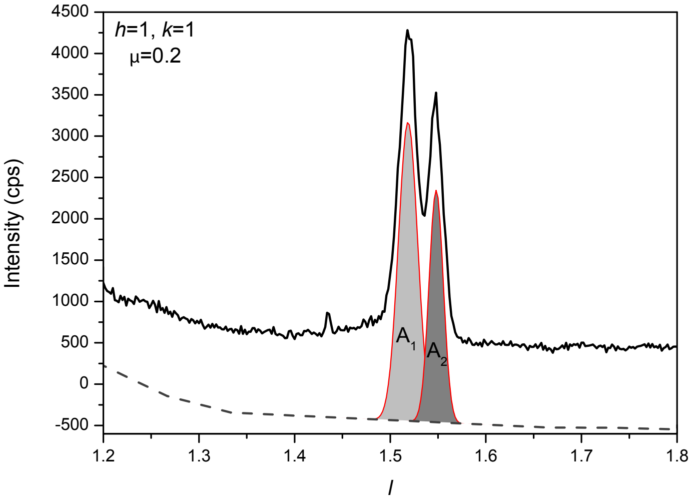

Figure 2.18: l-scans $(11l)$ of the Fe peak with $\mu = 0.2^o$ with the fitting of the two components.

direction yielding an effective lattice constant $c_{Fe_{Fe/Au}} = 2.72$ Å.

Regarding the Au vertical lattice parameter, a value $c_{Au} = 4.1$ Å was obtained from the l-scans of figures 2.16(b) and 2.17(b). This parameter is very close to those of section 2.2.1.

A full crystallographic characterization of the film is carried out by the measurement of reciprocal space maps (RSM). Figure 2.19 displays RSM for different families of planes to analyse the influence on the in-plane structure of the epitaxial strain. RSMs will probe the existence of structural distortions if present in the film. The notation in these maps is referred to the reciprocal space units of the MgO substrate. Note that Fe layer is rotated 45^o with respect the MgO substrate, so that the in-plane RSM of the Fe (101) directions correspond to the reciprocal space indexes $h = k = 1$; the same argument accounts for Fe (112) for which $h = 2$, $k = 0$.

In figure 2.19(d) it can be seen the very sharp space map of the MgO (111), characteristic of a high quality single crystal. Figures 2.19(a)

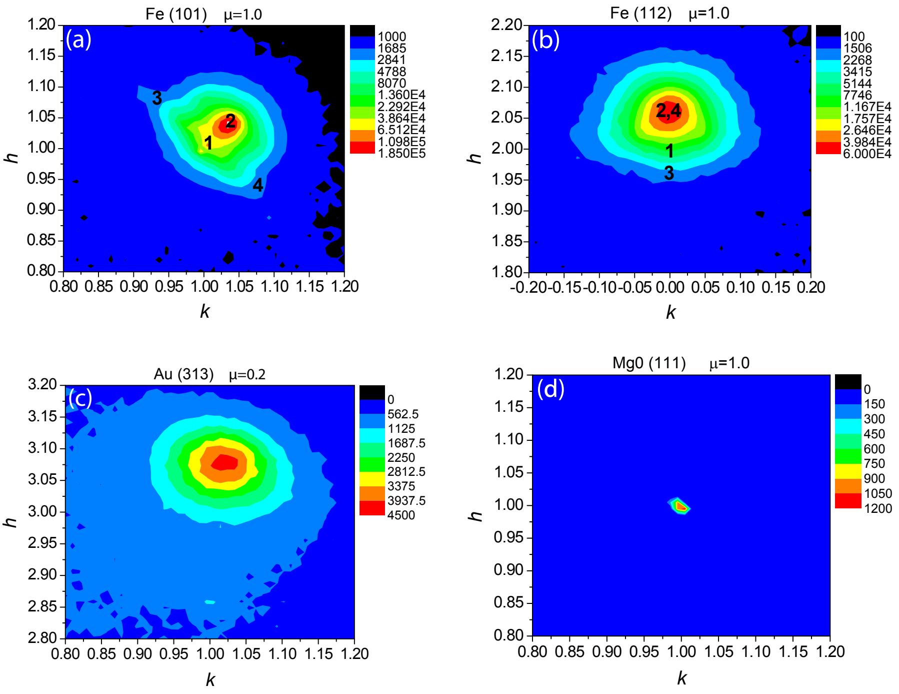

Figure 2.19: Reciprocal space maps of the Au (001)/Fe (001)/MgO (001) thin film for different families of planes: (a) Fe (101) and (b) Fe (112) in logarithmic scale; and (c) Au (313) and (d) MgO (111).

and 2.19(b) evidence some degree of in-plane distortion in the iron layer. Note that four different regions (labelled with numbers) of the reciprocal space with useful information can be distinguished. Number 1 is the contribution from the Fe planes at the MgO/Fe interface. It corresponds to values of $h = k = 1$, equal to the reciprocal point of the MgO substrate, which yields in-plane parameters of $a_{Fe_1} = b_{Fe_1} = 2.97$ Å, consistent with the expansion of the in-plane lattice. This means that Fe grows expanded in the film plane to accommodate a perfect epitaxy with the MgO substrate lattice.

However, the maximum intensity of Fe (101) RSM is located at number

2, for which $h = k = 1.04$. It corresponds to fully relaxed Fe planes with lattice parameter $a_{Fe_2} = b_{Fe_2} = 2.86$ Å, similar to the bulk one. This means that most of the Fe film has essentially been relaxed preserving its own bulk lattice constant.

Numbers 3 and 4 are contributions from the interface Fe/Au for which $h = 1.04$, $k = 0.96$, and $h = 0.96$, $k = 1.04$ respectively. These signals are symmetric due to the cubic structure of the system and they correspond to the same planes, yielding values of $a_{Fe_{3,4}} = b_{Fe_{3,4}} = 2.96$ Å for the in-plane lattice parameters.

The volume of the unit cell for the relaxed Fe layer is obtained from the in-plane lattice parameters determined by the reciprocal space maps and the perpendicular one from the l-scan, $V_{Fe} = a_{Fe_2} b_{Fe_2} c_{Fe} = 23.07$ Å^3. The perpendicular lattice parameter of the Fe atomic planes at the Fe/Au interface is also known from the l-scans taken at grazing incidence $\mu = 0.2^o$, $c_{Fe_{Fe/Au}} = 2.72$ Å. Assuming that the volume of unit cell is constant, the in-plane lattice parameters leads to $a_{Fe_{Fe/Au}} = b_{Fe_{Fe/Au}} = 2.91$ Å, in close agreement with the values obtained from the RSM maps. Similar result is extracted for the perpendicular lattice parameter of Fe at the MgO/Fe interface, $c_{Fe_{MgO/Fe}} = 2.62$ Å.

Figure 2.20 represents three profiles of the Fe (101) RSM; **A** is the $h = k$ profile, which has two peaks corresponding to the MgO/Fe interface and the relaxed Fe contributions (1 and 2), respectively; **B** presents only the contribution of the relaxed Fe (2); and **C** has three contributions, two from the Fe/Au interface (3 and 4) and another more intense corresponding to the MgO/Fe interface (1). A qualitative analysis of these three profiles shows that the largest signal comes from the relaxed Fe followed by the Fe atomic planes of the MgO/Fe and Fe/Au interfaces.

It could be noticed that at the interfaces the two in-plane Fe lattice constants are equal and larger than the perpendicular one, $a = b > c$. These results are consistent with the existence of tetragonal structural distortion. This effect is more pronounced at the MgO/Fe interface

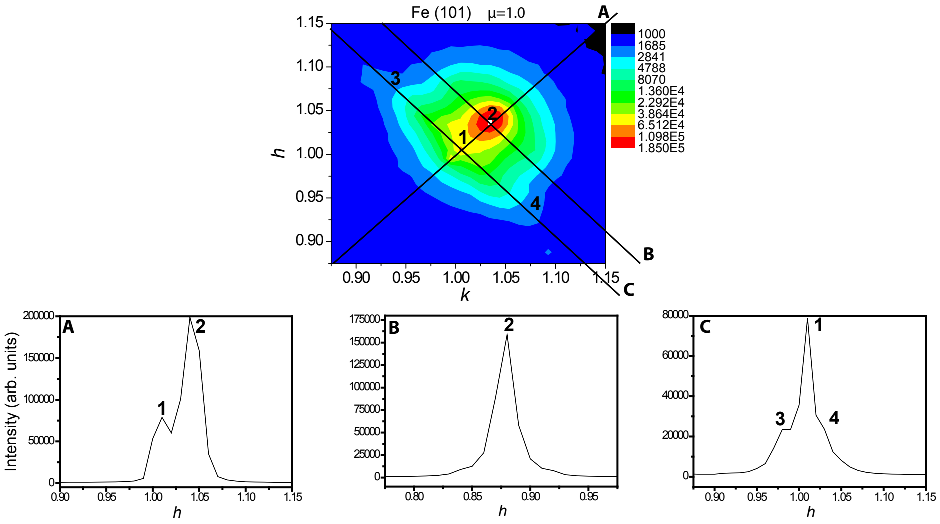

Figure 2.20: Reciprocal space map of Fe (101) with three profiles to resolve the Fe contributions.

($a_{Fe_{MgO/Fe}} = b_{Fe_{MgO/Fe}} = 2.97$ Å, $c_{Fe_{MgO/Fe}} = 2.62$ Å) than at the Fe/Au one ($a_{Fe_{Fe/Au}} = b_{Fe_{Fe/Au}} = 2.96$ Å, $c_{Fe_{Fe/Au}} = 2.72$ Å). This is a direct consequence of the mismatch between the lattices at those interfaces, which is more severe for MgO/Fe (-3.8%) than for Fe/Au (0.9%). However, the central Fe region has essentially relaxed Fe layers with the bulk lattice parameters.

Figure 2.19(c) displays the RSM of the Au (313) planes. In this case the Au in-plane lattice is rotated 45^o with respect to the Fe, and in registry with the MgO lattice. Due to the similar lattice constants of Au and MgO, Au RSM are to be measure for high h and l values to clearly detect any crystalline structural change if present. Au (313) RSM shows a single contribution at $h = 3.075$, $k = 1.025$. This results when referenced to MgO $h = k = 1$ provide $h^* = k^* = 1.025$ meaning that the Au has a square lattice with $a_{Au} = b_{Au} = 4.1$ Å, equal to perpendicular lattice parameter obtained from the l-scans. This evidences the cubic structure ($a_{Au} = b_{Au} = c_{Au}$) of the Au capping layer and the negligible influence of Fe/Au interface.

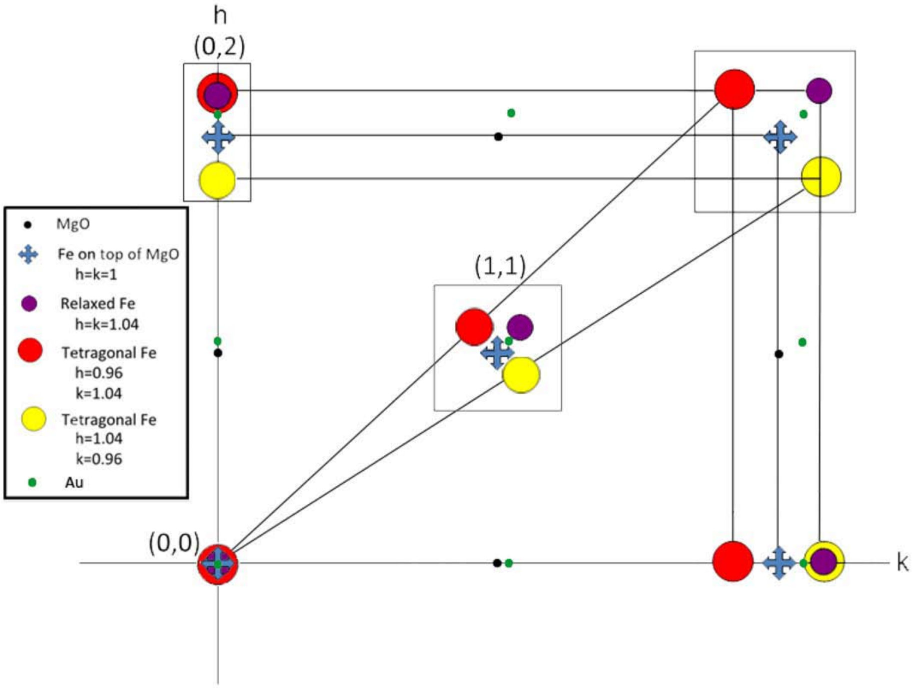

Figure 2.21: Scheme of the thin film plane $l = 0$ of the reciprocal space.

With all the previous results the $l = 0$ plane of the reciprocal space should be drawn as shown in figure 2.21. If this analysis is correct the Fe signals in the Fe (112) RSM, which corresponds to (200) reciprocal lattice point, referenced to the reciprocal units of the MgO substrate, should appear in the following positions: (i) the relaxed Fe at $h = 1.04 \cdot 2 = 2.08$, $k = 0$; (ii) the Fe from the MgO/Fe interface at $h = 1 \cdot 2 = 2$, $k = 0$; and (iii) the two signals from the Fe/Au interface at $h = 0.96 \cdot 2 = 1.92$, $k = 0$ and $h = 1.04 \cdot 2 = 2.08$, $k = 0$ (same position of the relaxed Fe). These calculated values are in good agreement with the those observed in the Fe (112) RSM, corresponding to numbers 2, 1 and 3 and 4 of figure 2.19(b), respectively.

2.2.3 Atomic Force Microscopy

Atomic force microscopy (AFM) is a scanning probe method to investigate the surface morphology and topography of a sample. It has a very high lateral resolution, which makes it a valuable technique for studying micro- and nano-structured surfaces. It uses a very fine tip on the end of a cantilever to probe the surface contours. A laser beam is focused on the backside of the cantilever, which is reflected onto a photodiode (figure 2.22). When the cantilever moves up and down according to the surface landscape, the laser beam gets deflected as well. Thus the deflection of the laser spot on the photodiode is proportional to the relative height displacement from the tip on the surface. Scanning the sample by means of xy piezos from side to side across the cantilever it provides a 2D/3D image which reveals information of morphology and roughness of the surface.

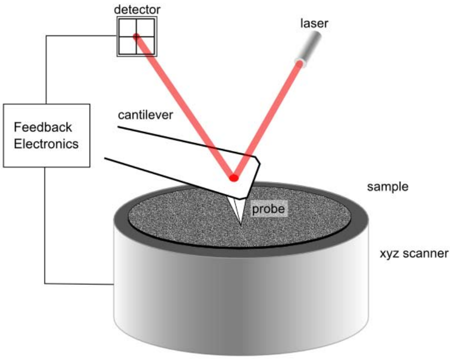

Figure 2.22: Scheme of the AFM operation.

The curvature of the cantilever tip, with dimensions of the order of nanometers, defines the lateral resolution of the atomic force microscope. The vertical or Z resolution is completely independent of the sharpness of the tip, usually below 0.1 nm. It depends on the noise in the system, and when feedback is enabled on the resolution limit of the actuating scheme, including the piezoelectric actuator that moves the tip and the sample relative to each other in the vertical direction.

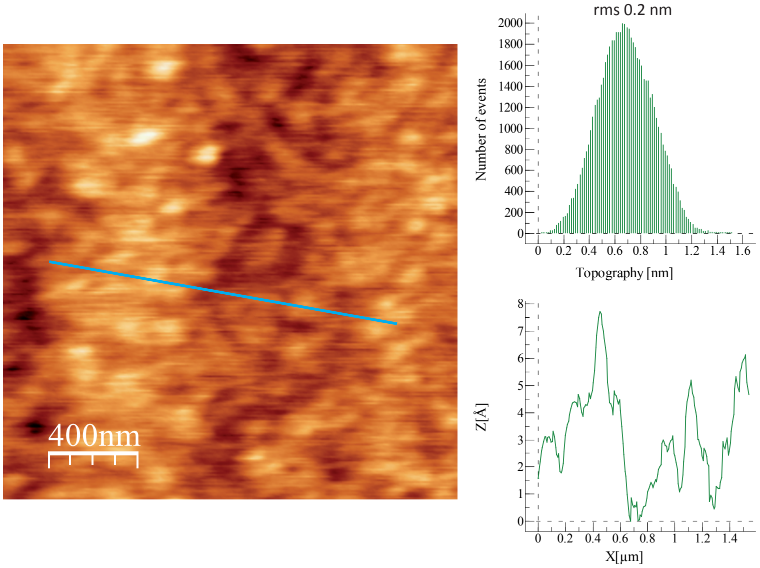

Figure 2.23: AFM image of size 2×2 μm^2 with the calculated roughness (rms), and a vertical profile across the surface of the sample.

In this thesis the AFM was used to study the sample morphology and to determine roughness of the surface. Different size AFM images were taken in tapping mode by Dr. C. Munuera and Prof. C. Ocal (ICMM) with a home-made AFM following the design by Kolbe *et al.* [14] and using an electronic control unit from Nanotec. It is known that the roughness of the image depends on the size of it [15]. The nominal roughness increases with the image size until it gets to a constant value higher than the real one. In the AFM used it is known that images of 2×2 μm^2 provide a good estimation for the roughness analysis.

The images were acquired and treated with the software WSxM from Nanotec [16]. Figure 2.23 shows a 2×2 μm^2 AFM image of the continuous thin film Au(001/Fe(001)/MgO(001) surface. It can be seen that the average height of the sample is 0.4 nm, the maximum height 1.4 nm and the rsm roughness 0.2 nm. These values show that the sample has a very flat surface. The profile of the entire sample shows a change of height of 8 Å in a very wide range, this result emphasizes the flatness of the sample. The image also shows the surface homogeneity and continuity, in good agreement with the previous X-ray structural characterization. These results confirms the good quality of the thin film.

2.2.4 X-ray Photoelectron Spectroscopy

The X-ray Photoelectron Spectroscopy (XPS) is based on the photoelectric effect. This technique is used to investigate the chemical composition at the surface of the sample, from which electrons are emitted and filtered in energy via a hemispherical analyser. The number of electrons (or intensity) with defined kinetic energy ($\mathrm{E_K}$) are recorded by a detector. The resulting spectrum exhibits resonance peaks at binding energies ($\mathrm{E_B}$) characteristics of the electronic structure of the atoms present at the sample surface. Therefore $\mathrm{E_B}$ allows to identify not only the present element but also its chemical state. The relationship between the parameters involved in the XPS experiment is $\mathrm{E_B} = h\nu - \mathrm{E_K} - \phi_\mathrm{s}$, where $h\nu$ is the photon energy and ϕ_s is the sample work function (figure2.24).

While the X-rays may penetrate deep into the sample, the escape depth of the ejected electrons is limited, providing surface sensitivity to the XPS technique. By considering electrons with $\mathrm{E_K} = 1000$ eV that emerge at 90^o to the sample surface, 65% of the signal will emanate from a depth of less than 1.7 nm, 85% and 95% from a depth of 3.3 nm and 5 nm, respectively.

XPS measurements have been performed in UHV system equipped with a Specs Phoibos-100 electron spectrometer (Berlin, Germany), using a non-monochromatic Mg-K_α ($h\nu = 1253.6$ eV) X-ray source.

This UHV system is also equipped with an ion gun from which Ar^+ ions are accelerated at a given energy onto the sample surface. This ion bombardment sputters the outermost layers of the sample by controlling the ions current and the irradiation time. Depth profiling experiments are

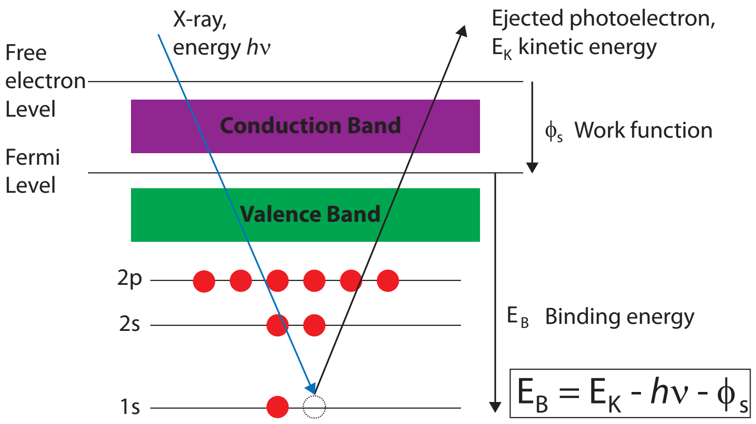

Figure 2.24: Energy diagram of XPS process.

done by measuring XPS spectra at different stages of ion sputtering and sample thickness.

Depth profiling results in Fe/MgO thin films, grown in the same conditions as Au/Fe/MgO samples, but with no Au capping layer are displayed in figure 2.25. Each individual spectrum is taken at different depth as the thin film atomic layers are sputtered off. Thus, chemical composition of the thin film for different thickness can be extracted. The sample was eroded with two different conditions: i) Low rate (E=1 KeV, 0.08 Å/min) to study the presence of different oxidation states and to follow the chemical composition changes at the outermost layers of the thin film. ii) medium rate (E=1.4 KeV, 0.23 Å/min) to study the cleanliness of the Fe layer and discard the existence of Fe-oxide phases or contaminants in depth. The XPS spectrum of the as-grown samples (black) shows the full oxidation of the Fe surface. Upon a very gentle ion bombardment and the removal of a layer 0.7 nm thick, the emission of metallic Fe is readily observed apart from the presence of Fe-oxides (red). As ion sputtering proceeds, the increase of this metallic signal is clearly evidenced until it reaches saturation. Fe-oxides contribution continuously

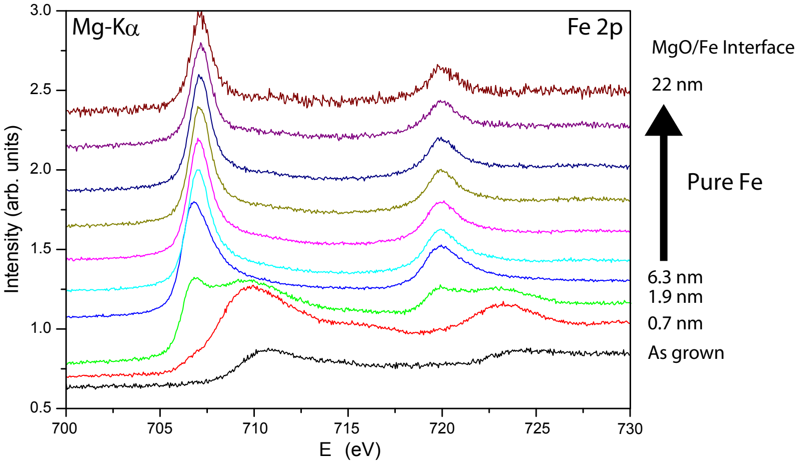

Figure 2.25: XPS spectra of the Fe 2p region taken at different depths of the thin film.

decreases from an effective depth of 2 nm (green) until 6 nm (dark blue), form which there only exists the characteristic lineshape of metallic pure Fe. The last spectrum (the upper one) corresponds to the Fe layers next to the MgO/Fe interface, where a very low signal to noise ratio is obtained since most Fe was removed.

The oxidation of the Fe surface might influence on the magnetic properties of the thin film. Therefore, samples are to be protected or passivated by the growth of a capping layer, which should prevent any eventual chemical modification. In particular a Au layer 3 nm thick has been deposited on the Fe/MgO (001) films. Similar depth profiling experiments have been performed in Au/Fe/MgO samples. Once the Au layer is plenty sputtered off, Fe 2p emission from pure metallic Fe is only present, confirming the good properties of the Au layer for capping purposes.

2.3 Magnetic characterization

2.3.1 Magneto Optical Kerr Effect

The Faraday Effect, observed in 1845 in a piece of glass placed between the poles of a magnet, was the first magneto-optical effect discovered. The existence of this effect was a strong affirmation of the electromagnetic nature of light. The phenomenon, a rotation of the plane of polarization of linearly polarized light propagating in a medium in a magnetic field, was rightly understood as implying a circular birefringence, that is, different indexes of refraction for the left and right circularly polarized components into which the linearly polarized wave could be resolved. The corresponding effect in reflection, known as Kerr effect, was discovered by Kerr in 1876.

There are three different configurations to measure the Kerr effect with a Magneto Optical Kerr Effect magnetometer (MOKE) (figure 2.26): the longitudinal, in which the magnetic field is applied parallel to the sample surface and to the incidence plane; the transverse, in which the magnetic field is applied parallel to the sample plane but perpendicular to the incidence plane; and the polar, in which the sample plane is perpendicular to the applied magnetic field.

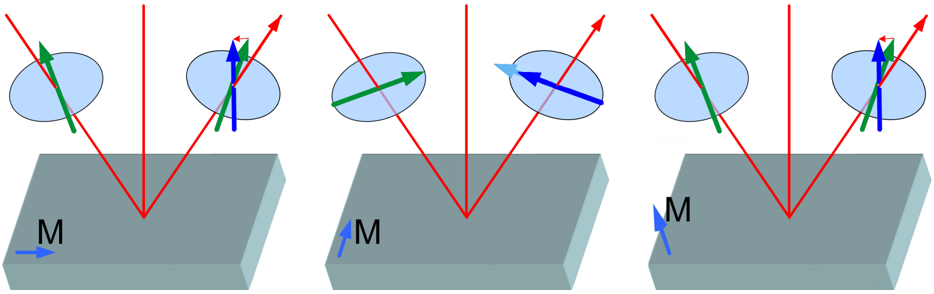

(a) (b) (c)

Figure 2.26: The three possible configurations to measure Kerr effect (a) longitudinal (b) transverse and (c) polar.

Both in the longitudinal and the polar cases the effect is simple and occurs either for P polarized ($\vec{E}_0$ parallel to the plane of incidence) or S polarized ($\vec{E}_0$ perpendicular to the plane of incidence) incident radiation. The effect is that radiation incident in either of these linearly polarized states is, on reflection, converted to elliptically polarized light. The major axis of the ellipse is often rotated a small angle with respect to the incoming polarization plane, this angle is referred to as the Kerr rotation (θ_k). There is an associated ellipticity, called Kerr ellipticity (ϵ_k). The sign and magnitude of these effects are proportional to $\vec{M}$.

The reflected beam consists of two orthogonal electric fields: $\vec{E}_r$, with the same polarization state of the incident beam, is large and proportional to the usual Fresnel coefficient r, $\left|\vec{E}_r\right| = r\left|\vec{E}_0\right|$, where $\vec{E}_0$ represents the field of the incident beam; $\vec{E}_k$, perpendicular to $\vec{E}_r$, is small and proportional the Kerr coefficient k, $\left|\vec{E}_k\right| = k\left|\vec{E}_0\right|$ (figure 2.27). The reflected beam is monochromatic plane wave with the frequency ω and the wave number k_z propagating in z direction that can be described in the following way:

$$\vec{E}_{ref} = Re(\vec{E}_{ref_0} e^{i(\omega t - k_z z)}), \text{ with } \vec{E}_{ref_0} = \begin{pmatrix} E_r \\ E_k \\ 0 \end{pmatrix} \tag{2.4}$$

Since $k << r$ the complex Kerr rotation can be written as:

$$\theta_k + \mathrm{i}\epsilon_k = \frac{E_k}{E_r} \tag{2.5}$$

The transverse case is quite different from the previous two. There is only an effect for P polarized radiation, and in such a case, the reflected radiation remains linearly polarized with just a slight change in the reflected intensity of the order of 1% or less. The field of the reflected beam results from the sum of two parallel vectors, $\vec{E}_r$, one whose magnitude is proportional to the normal Fresnel coefficient, $\left|\vec{E}_r\right| = r\left|\vec{E}_0\right|$, and a small vector, $\vec{E}_k$, with its magnitude proportional to the Kerr coefficient, whose

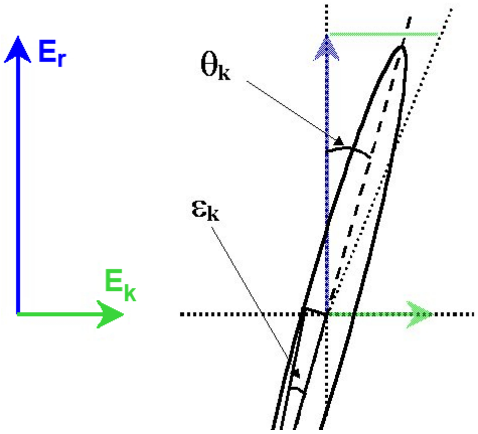

Figure 2.27: Decomposition of the reflected beam in the two orthogonal $\vec{E}$ showing θ_k and ϵ_k.

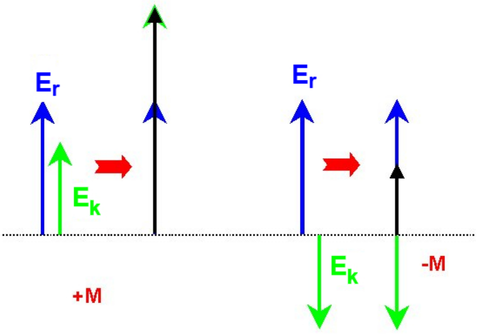

Figure 2.28: Variation of the amplitude for Kerr transverse configuration.

magnitude and direction depends on $\vec{M}$. As $\vec{M}$ changes sign from $+\vec{M}$ to $-\vec{M}$ the reflectivity changes from $\mathrm{R}_{\max} = |r + k|$ to $\mathrm{R}_{\min} = |r - k|$ as can be seen in figure 2.28.

A more detailed theoretical explanation can be found in the literature, for example in references [17] and [18].

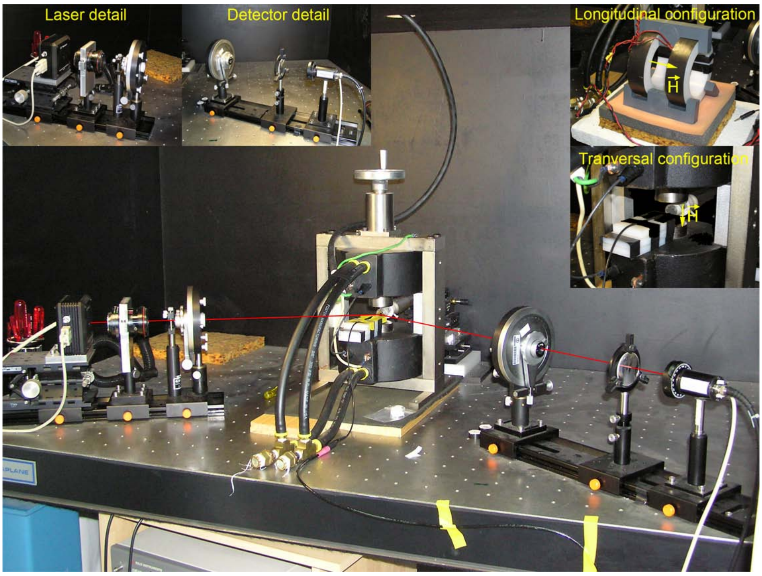

Figure 2.29: Picture of the Kerr set-up.

In this thesis both the longitudinal and transverse configuration have been used in a custom designed vectorial MOKE. It consists of a laser diode with a wavelength of 640 nm, the laser beam passes through a first polariser, S polarized for the longitudinal configuration and P polarized for the transverse configuration. A magnetic field is applied to the sample, for the longitudinal configuration it is applied with a pair of Helmholtz coils, having a maximum field of 550 Oe, whereas for the transverse case an electromagnet is used having a maximum field of 5 kOe. The polarized laser beam is reflected by the magnetized sample and then passes through a second polariser (analyser) P polarized for both configurations, the polarized reflection gets to a photodiode that measures its intensity. A photo of the set-up is shown in figure 2.29. With this set up it is possible to measure the magnetization parallel and perpendicular to the applied magnetic field just by rotating 90^o the polariser.

The longitudinal configuration was measured with S polarized radiation and with the analyser almost perpendicular to the entrance one, thus cancelling the $\vec{E}_r$ component; just intensity variations associated with the $\vec{E}_k$ component are measured. The transverse configuration was measured with P polarized radiation and with the analyser parallel to the first polariser, in this case all the intensity is measured.

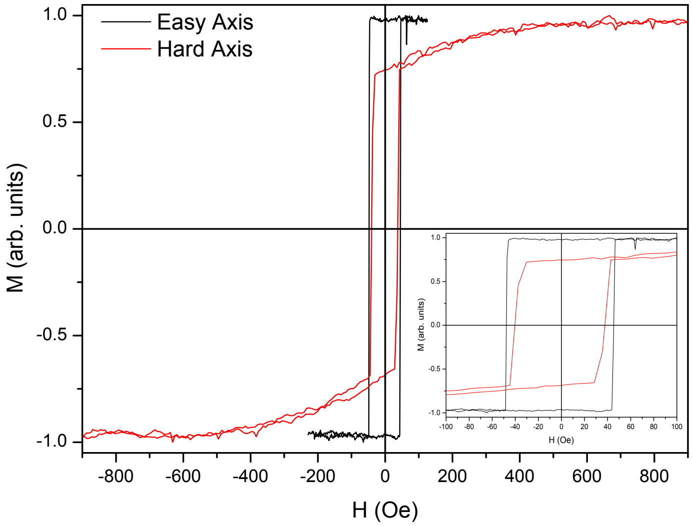

Figure 2.30: Hysteresis loops for the easy and hard axes.

By means of this system, in the longitudinal configuration, the hysteresis properties of the as deposited films were analysed. Figure 2.30 shows the hysteresis loops of the easy and the hard axes. As expected, very square hysteresis loop is obtained for the easy magnetocrystalline axes, with remanence equal to saturation. The magnetization switches from $+M_s$ to $-M_s$ in a single jump with a very narrow switching field distribution

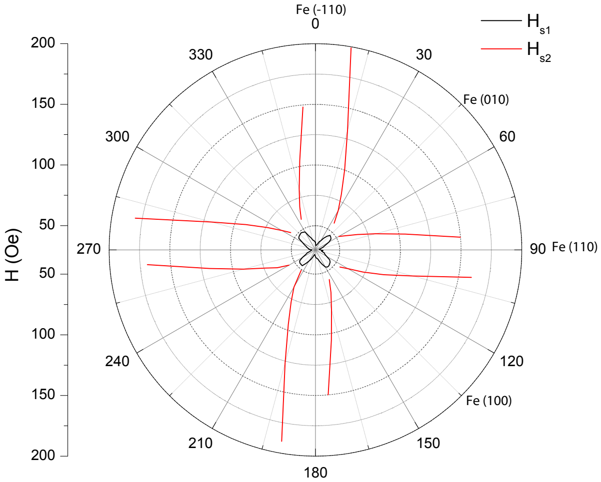

(a)

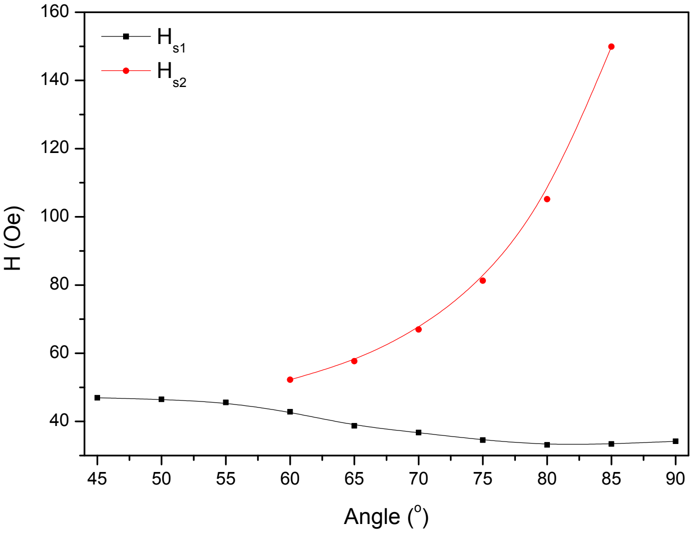

(b)

Figure 2.31: (a) Polar diagram of the angular dependence of the switching fields in epitaxial Au (001)/Fe (001)/MgO (001) films (b) Detail of the two jumps in the switching fields for the angular range between the easy and hard magneto crystalline axes.

(SFD), of 1 Oe approximately. This narrow switching process relies on the nucleation of one or just a few reversed nuclei that sweep the whole film when the field reaches the coercive force value [19, 20]. In contrast the hard axis has a remanence of $0.7M_s$, because the magnetization lies along the easy axis (at 45^o with respect to the hard axis) in absence of any applied field. It exhibits the hysteresis loop typical of a hard axis magnetization rotation mechanism, after the switching process, the magnetization approaches saturation by means of reversible rotations. The field required to reach the saturation is about 500 Oe, in agreement with the anisotropy field. All these experimental data are a strong affirmation of the excellent singlecrystalline nature of the Au/Fe/MgO (001) films [20, 21].

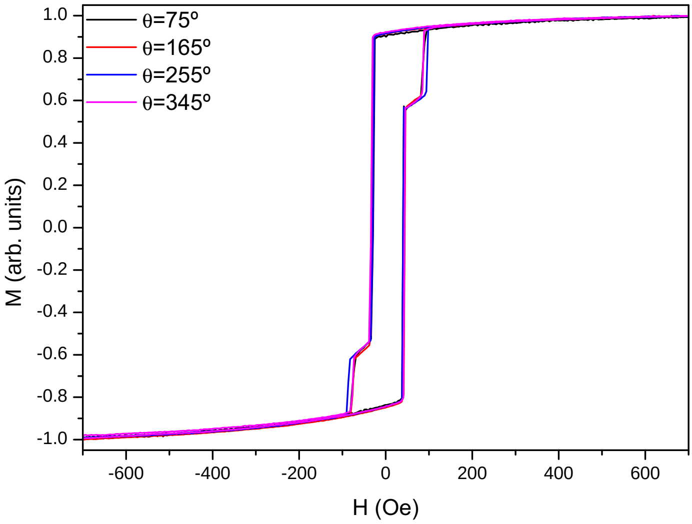

Figure 2.32: Orthogonal hysteresis loops out of the easy or hard axes.

The in-plane hysteresis loops of the Fe films are characterized by the existence of either one or two irreversible jumps. The loops measured along the hard and easy axes or 10^o, approximately, around the easy axis a single jump occurs at $H = H_{s1}$, whereas for the rest of the cases the loops present two jumps at H_{s1} and H_{s2}, respectively. Figure 2.31(b) shows the evolution of both switching fields between an easy (45^o) and hard (90^o) axis the smaller switching field, as the loops are measured closer to the hard axes H_{s1} decreases, whereas H_{s2} exhibits a steep increase. Figure 2.32 exhibits four hysteresis loops for orthogonal angles (75, 165, 255 and 345^o) with similar H_{s1} and H_{s2}. Those behaviours are typical of films with four-fold anisotropy.

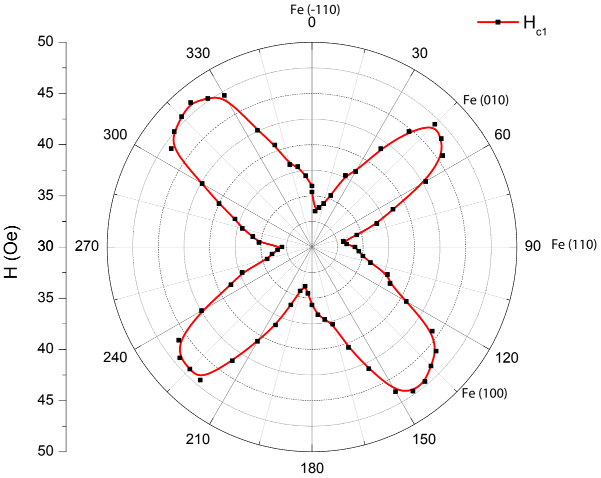

Figure 2.33: Angular dependence of the coercive field.

Even though the samples are fabricated under highly controlled conditions, as the coercivity is an extrinsic parameter, they do not have all the same coercive field. Most films have a coercive field around 40 Oe in the easy axes and 35 Oe in the hard one, but there is a distribution of values from 140 Oe to 10 Oe

To check the quality of the films the angular dependence of the quality of the Au/Fe/MgO (001) films the angular dependence of the switching fields, of the coercivity ($H_c = H_{s1}$) and of the remanence were studied along a full 360^o round, presented in figures 2.31(a), 2.33 and 2.34, respectively. The three polar plots evidence an excellent four-fold symmetry with a H_c from 47 to 48 Oe and from 33 to 34 Oe along the easy and hard axes, and

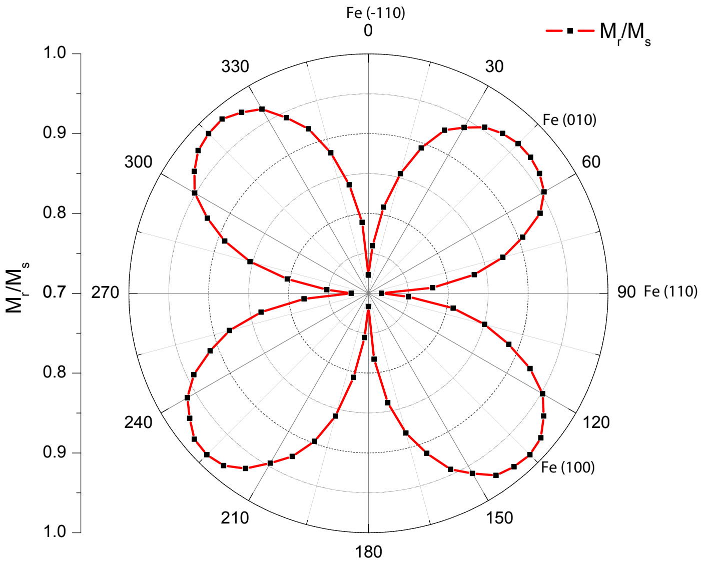

Figure 2.34: Angular dependence of the remanence of the thin film.

$M_r = 0.99M_s$ and $0.7M_s$ along easy axis and the hard axis, respectively, as said above.

This study allows to discard the eventual existence of any uniaxial anisotropy contribution superimposed to the biaxial anisotropy in the Au/Fe/MgO (001) films, which is usually presented in many Fe films reported in the literature. An example of this are the epitaxial Fe films studied by Costa-Krämer *et al.* [22], which, although having a four-fold symmetry due to their in-plane biaxial anisotropy, present different coercivity and remanence values for the cases of loops measured at orthogonal angles. The superimposed uniaxial anisotropy contributions might be due to the many different causes, such as specific substrate surface features (steps or miscuts) or the existence of uncontrolled magnetic fields in the deposition systems (in the case of some magnetron sputtering systems).

2.3.2 Vibrating Sample Magnetometer

The Vibrating Sample Magnetometer (VSM) uses an induction technique for the measurement of magnetic moment by detecting the a.c. field produced by an oscillating sample moment. The technique was first highlighted by Simon Foner [23] and has since become universally accepted as a research measurement technique for various magnetic and superconducting applications.

VSM provides the full magnetic moment of the sample, while the MOKE is a localized technique that provides a signal proportional to the magnetization in the area illuminated by the laser spot and the penetration depth of the incident beam (typically a few tens nanometers for visible light in metals).

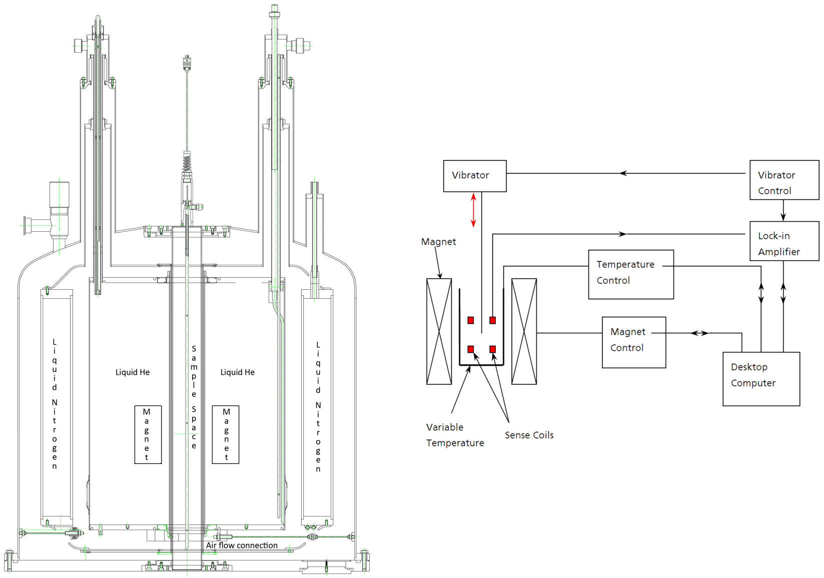

Figure 2.35: Scheme of the VSM: different chambers of the cryostat and operation configuration.

In this work an Oxford Instruments MLVSM9 MagLabVSM was used (figure 2.35). It consists of a vibrator that makes the sample oscillates with

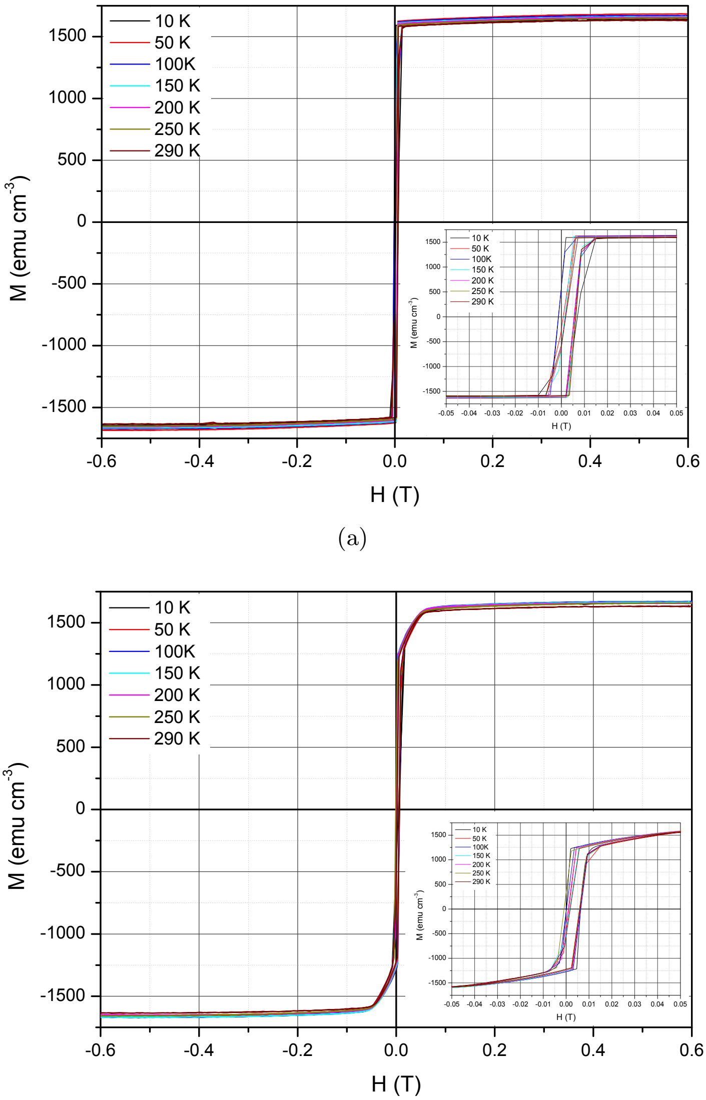

(a)

(b)

Figure 2.36: In-plane hysteresis loops taken at different temperatures from 10 to 290 K with magnetic field parallel to magnetocrystalline (a) easy and (b) hard axes.

a constant frequency (55 Hz) and amplitude (0.1-1.5 mm). A maximum magnetic field of 9T is applied to the sample with superconducting coils, parallel to the vibration direction. The oscillatory motion of the sample changes the flux in the detection area, where four sense coils measure the electromotive force induced by this flux change following the Faraday's law, being proportional to the magnetic moment of the sample.

This VSM has a cryostat with liquid He (LHe) surrounded by a chamber with liquid N_2 (figure 2.35). The LHe reservoir is connected to the sample space by a needle valve that controls the flux of He gas around the sample. The sample temperature can be varied from 300 K to 5 K by controlling the He gas flow and powe of the resistive heater located near the sample.

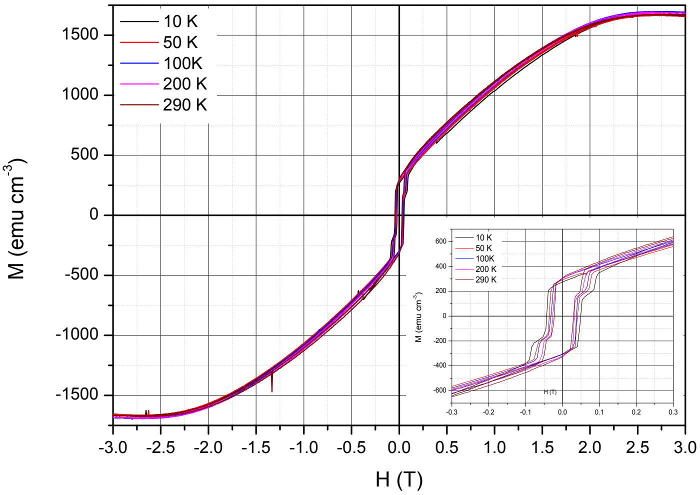

Figure 2.37: Out of plane hysteresis loops for different temperatures (10-290 K) with magnetic field perpendicular to the thin film.

This VSM allows to measure the change of the sample magnetization as a function of any combination of the following parameters, magnetic field, temperature and time, with a resolution of approximately, $1 \cdot 10^{-6}$ emu and noise of $4 \cdot 10^{-7}$ emu. Hysteresis loops of the Au/Fe/MgO (001) thin film in three interesting directions (in-plane parallel and perpendicular to the magnetocrystalline easy axes, and perpendicular to the thin film) are exhibited in figures 2.36 and 2.37.

In the out of plane hysteresis loops (figure 2.37) the value of the saturation field obtained is $H_{sat} = 2.5$ T. The saturation magnetization in-plane at room temperature is $M_s = 9.4 \cdot 10^{-4}$ emu, as the sample has a volume of Fe of $V_{Fe} = 5.76 \cdot 10^{-7}$ cm^3. The saturation magnetization in emu/cm^3 is then $M_s = 1631.94$ emu/cm^3. The in-plane saturation magnetization at room temperature, $M_s = 2.05$ T, is in good agreement with the theoretical value, 2.15 T, and is equal to the one reported in [24].

2.3.3 Ferromagnetic Resonance

In a conventional Ferromagnetic Resonance experiment (FMR) a magnetic system is simultaneously exposed to a variable static external field ($\vec{H}_0$) and to a sinusoidal electromagnetic field ($\vec{H}_1$), with a fixed angular frequency, ω, typically in the Gigahertz range (microwaves). The microwave pumping field $\vec{H}_1$ exerts a small perturbing torque $\vec{M} \times \vec{H}_1$ tilting the magnetic momentum $\vec{M}$ by a small angle θ out of its equilibrium, resulting in a small amplitude harmonic oscillation of $\vec{M}$ around the static equilibrium in the direction of total effective field $\vec{H}_{eff}$ as shown in figure 2.38. This magnetic field $\vec{H}_1$ of small amplitude and perpendicular to the static field, gives rise to an oscillatory (magnetization) response of the same frequency whose amplitude depends on ω and reaches a maximum at a value $\omega = \omega_r$. The resonance frequency, ω_r, is determined by the effective field which includes both external and internal fields. As a result of $\vec{H}_0$ and the internal fields (magnetocrystalline anisotropy, dipolar fields, interface anisotropy, etc) the magnetization is stabilized along a given direction corresponding to an energy minimum.

The equation of motion of the magnetization, assumed to be homogeneous throughout a sample (what is known as ”saturated mode”), is given by:

$$\frac{d\vec{M}}{dt} = -\left|\gamma\right| \mu_0 \vec{M} \times \vec{H}_{eff} \tag{2.6}$$

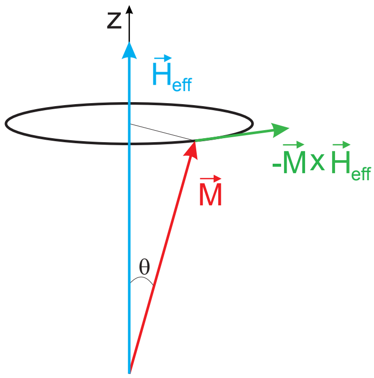

Figure 2.38: Precession of $\vec{M}$ around the static equilibrium in the direction of total effective field $\vec{H}_{eff}$.

Where γ is the gyromagnetic factor and $\vec{H_{eff}}$ represents the effective field acting on the magnetization, which comprises the applied field and the internal fields. Although this equation includes no dissipative terms, it allows to explain the main features of the resonance phenomenon. Upon the application of the oscillatory, low amplitude field $\vec{H}_1$, magnetization oscillations with the same frequency are induced along the direction of $\vec{H}_1$. The susceptibility χ associated with these oscillations is:

$$\chi = \frac{C}{1-(\omega/\omega_r)^2} \tag{2.7}$$

C being a constant. As can be seen in figure 2.39(a), χ tends to infinity as ω approaches the resonance frequency ω_r. The resonance frequency depends on the curvature of the energy landscape around the energy minimum and, as a consequence, on the applied static field. It can be calculated by means of equation 2.6 by taking into account the specific conditions of a given sample: geometry, crystalline structure and magnetic anisotropy, intensity and relative orientation of the applied field with respect to the crystalline axes, etc. When dissipative (damping) terms are included in equation 2.6 the value of ω_r remains essentially unchanged unless the dissipative terms are too large. Under resonance conditions the phase of the magnetization oscillations is delayed $\pi/2$ with respect to the excitation field and maximum absorption of the microwave radiation occurs.

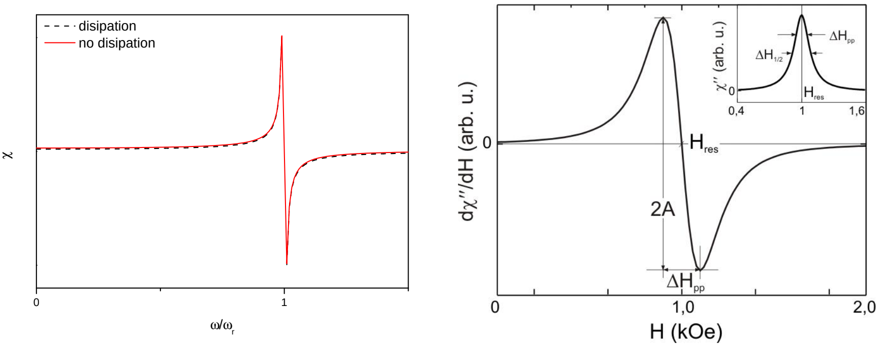

(a) (b)

Figure 2.39: (a) Solid (dotted) line: evolution of the susceptibility with the frequency when the dissipation terms are (are not) not taken into account and (b) field derivative of the imaginary part of the susceptibility with the field (Inset: Imaginary part of the susceptibility with the field with the parameters corresponding to the main features.

In the specific case of singlecrystalline Au (001)/Fe (001)/MgO (001) thin films, the resonance frequency can be calculated taking into account the demagnetizing fields, associated with the demagnetizing factors $N_x = N_y \approx 0$ and $N_z \approx 1$, where z corresponds to the (001) direction (normal to the film), and the anisotropy field due to the magnetocrystalline energy, a cubic anisotropy with anisotropy constant K_{ani} and the in-plane easy axes along the (010) and (100) directions. When the static field $\vec{H}_0$, enough to saturate the sample, is applied in-plane, the resonance frequency can be obtained either as [25, 26]:

$$\left(\frac{\omega}{\gamma}\right)^2 = \left(\mu_0 H_r + \frac{2K_{ani}}{M_s}\right)\left(\mu_0 H_r + \mu_0 M_s + \frac{K_{ani}}{M_s}\right) \tag{2.8}$$

if $\vec{H}_0$ is parallel to an easy axis, (100) or (010), or as:

$$\left(\frac{\omega}{\gamma}\right)^2 = \left(\mu_0 H_r - \frac{2K_{ani}}{M_s}\right)\left(\mu_0 H_r + \mu_0 M_s + \frac{K_{ani}}{M_s}\right) \tag{2.9}$$

when $\vec{H}_0$ is along a hard in-plane axis (110). In these expressions K_{ani} represents the magnetocrystalline anisotropy constant and M_s is the saturation magnetization.

Regarding the experimental FMR set-ups, most of them use a microwave excitation of constant frequency and drive the magnetic system through the resonance condition by sweeping the external field $\vec{H}_0$. The measured FMR signal is proportional to the field derivative of the imaginary part of the susceptibility ($d\chi''/dH_0$) (figure 2.39(b)), which, in turn, is proportional to the absorption power. In other words, the FMR technique is based on measuring microwave losses in a magnetic sample as a function of the external d.c. magnetic field.

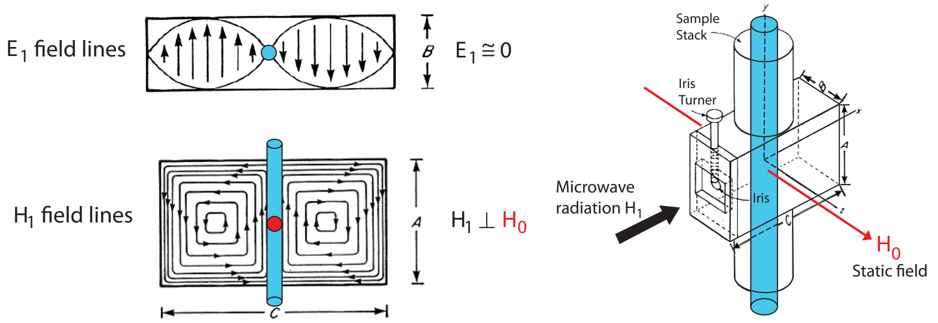

Figure 2.40: Resonance cavity of FMR.

The FMR studies included in this thesis were carried out in collaboration with Professor Nikolai A. Sobolev at the Physics Department of Aveiro University, Portugal. The set up consists of a resonant cavity TE_{102} in which the sample is placed and exposed to microwave radiation of 9.8 GHz and to a variable static field $\vec{H}_0$ (1.5 T maximum). The magnetic sample is placed in the centre of the cavity, where the microwave and static magnetic fields are perpendicular one to another as shown in figure 2.40. When the resonance field is achieved the sample goes to maximum absorption, which changes the quality factor of the cavity and increases the reflected power. In order to enhance the signal to noise ratio an additional sinusoidal signal of small amplitude at 100 kHz, modulates the d.c. magnetic field. This 100 kHz modulated part of the reflected signal is detected via lock-in techniques improving the signal to noise ratio and the precision of the measurement.

In addition, this set up is configured to measure the angular dependence of the FMR. The sample can be placed with its surface plane parallel to both magnetic fields (see figure 2.40) and rotated around its normal axis, thus changing the angle between the in-plane easy axes and the applied static field.

This type of measurement was used to study the anisotropy of the as-deposited Au/Fe/MgO (001) films. Figure 2.41(a) shows the angular dependence of Au (001)/Fe (001)/Mg (001) epitaxial thin film, prepared at the PLD system described in section 2.1, similar to those employed to fabricate the lithographic arrays that are going also to be studied by FMR in this thesis. FMR spectra are taken for a complete 360^o rotation with 5^o step. A detailed analysis, 1^o step, was carried out when the applied field is close to the in-plane hard axis Fe (110), as shown in figure 2.42(a). Resonance peaks are observed for fields about 100 mT, around angular positions corresponding to the magnetocrystalline in-plane hard axes of this particular sample, with a four-fold symmetry (90^o periodicity), as depicted in the polar plot of figure 2.41(b). This polar diagram was obtained by fitting each spectra, such as the one represented in figure 2.39(b), to a Dyson curve, equation 2.10 [27].

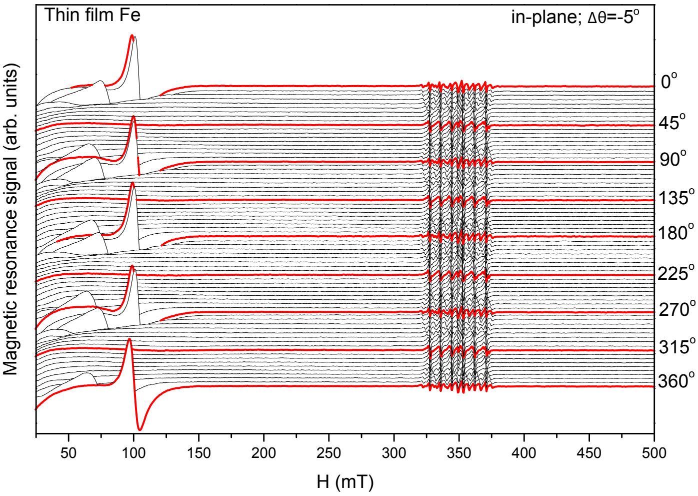

(a)

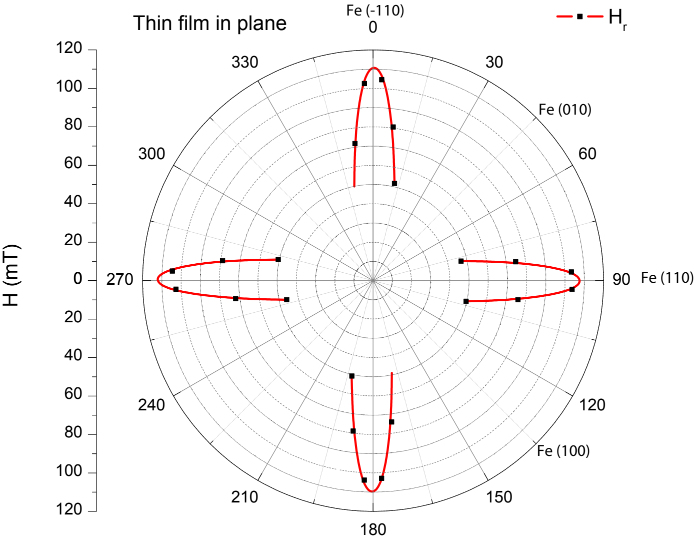

(b)

Figure 2.41: (a) Angular dispersion of the FMR spectra for in-plane applied magnetic field (b) Polar plot of the resonance field.

$$\begin{aligned} I =& I_0 + A\left(\frac{c(H-H_r)^2 + c\cdot\Delta H_{pp}^2 - 2(H-H_r)(\Delta H_{pp} + c(H-H_r))}{((H-H_r)^2+\Delta H_{pp}^2)((H-H_r)^2+\Delta H_{pp}^2)}\right. \\ &\left. + \frac{c(H+H_r)^2 + c\cdot\Delta H_{pp}^2 - 2(H+H_r)(\Delta H_{pp} + c(H+H_r))}{((H+H_r)^2+\Delta H_{pp}^2)((H+H_r)^2+\Delta H_{pp}^2)}\right) \end{aligned} \quad (2.10)$$

The Dyson curve is a combination between the absorption and dispersion of a symmetric Lorenztian function, where A is the amplitude of the signal, ΔH_{pp} the width and H_r the resonance field.

The small amplitude signal observed at fields between 310 and 380 mT is angle independent, and it was proved to be due to the paramagnetic resonance of the substrate. The detailed analysis presented in figures 2.41(b) and 2.42(b) shows that the field matching the FM resonance condition is 106 mT along the hard axis direction.

The field dependence of the resonance frequency was calculated according to expressions 2.8 and 2.9 by using the gyromagnetic factor for a free electron ($g = 2$, $\gamma = 1.759 \cdot 10^{11}$ T^{-1} s^{-1}), the anisotropy constant value reported in the literature for bulk Fe at room temperature ($K_{ani} = 45 \cdot 10^3$ J m^{-3}) and the saturation magnetization at room temperature obtained by in-plane VSM measurements ($M_s = 2.05$ T). As can be seen in figure 2.43, when the field is applied along an easy axis direction, the value matching the resonance frequency of 9.8 GHz is close to zero, making it impossible to observe the resonance peaks by experimentally sweeping the field in our FMR set-up. Even for $H_0 = 0$ mT a frequency higher than 9.8 GHz should be needed to observe the FMR absorption. On the contrary, when the field is applied along the in-plane hard axis (see inset of the figure 2.43) the frequency of 9.8 GHz corresponds to a field value of 107.5 mT, in very good agreement with the experimental maximum absorption (106 mT). This result garanties the confidence on the used values of the magnetocrystalline anisotropy constant and saturation magnetization, in good agreement with the reported ones, with no extra anisotropy

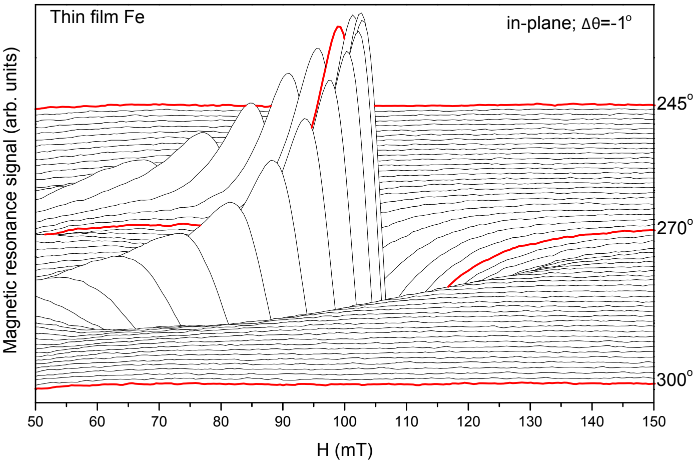

(a)

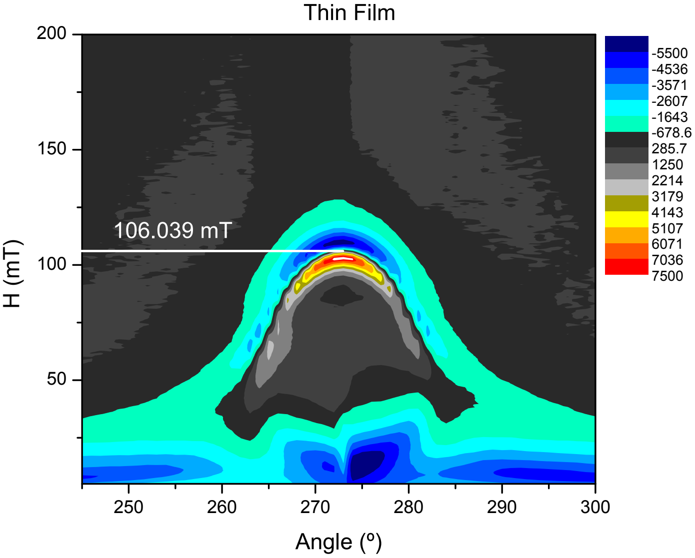

(b)

Figure 2.42: (a) Detail of the angular dispersion around the Fe (1-10) hard axis direction shown in figure 2.41(a) (b) 2D plot of the FMR intensity.

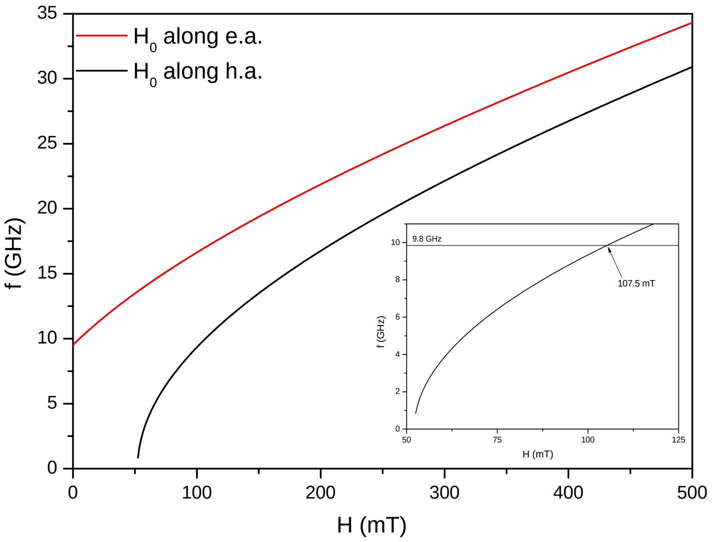

Figure 2.43: Resonance frequency as a function of the applied field calculated by means of equations 2.8 and 2.9. The inset show a detail of the curve obtained when the field is applied along the hard axis, around the resonance condition.

contributions, as already confirmed by means of the results of section 2.3.1.

2.4 Lithography

Electron beam lithography (EBL) and lithography with focused ion beam (FIB) are specialized techniques for creating micro and nanostructures. A beam of electrons or ions is scanned in a well defined pattern across a surface. There are various methods to transfer the scanned patterns into the desired structure. In the case of the classical EBL the substrate is covered with a resist film sensitive to electron irradiation. The exposed structure can be developed (positive or negative) subsequently and transferred by etching or deposition methods. In the standard operation mode of FIB lithography the ion beam removes atoms from the surface at the spot where it hits the substrate (milling). Thus the pattern can be engraved directly into the material. The main attributes of these technologies are the very high spatial resolution to the nanometric level and the extraordinary flexibility which can be applied to a broad variety of materials and an almost infinite number of patterns.

2.4.1 Focused Ion Beam Lithography

In recent years several fabrication techniques using electrons and ions have been develop to achieve a better control of nanostructures fabrication. The FIB is one of the most promising techniques because it is a maskless process providing great flexibility and simplicity. Apart from that, a regular application of FIB is the preparation of specimens for cross-section transmission electron microscopy (TEM) [28]. This technique has also a very serious drawback due to the spatial extension associated with the focused ion beam irradiation, which leads to radiation damage and ion implantation in extensive areas that may change the properties of the material, especially in systems with materials very sensitive to ion induced effects [29].

A schematic diagram of a FIB ion column is shown in figure 2.44. The structure of the column is similar to that of a scanning electron microscope, the major difference being the use of a gallium ion (Ga^+) beam instead of an electron beam. A vacuum of 10^{-7} mbar is maintained inside the column. The ion beam is generated from a liquid-metal ion source (LMIS) by the application of a strong electric field. This electric field causes the emission of positively charged ions from a liquid gallium cone, which is formed on the tip of a tungsten needle. A typical extraction voltage and current are 7000 V and 2 μA, respectively, under normal operating conditions. The ion beam energy is typically between 10 and 50 keV, with beam currents varying, over four decades, between 1 pA and 10 nA. This allows both a fine beam for high-resolution imaging on sensitive samples and a heavy beam for fast and rough milling.

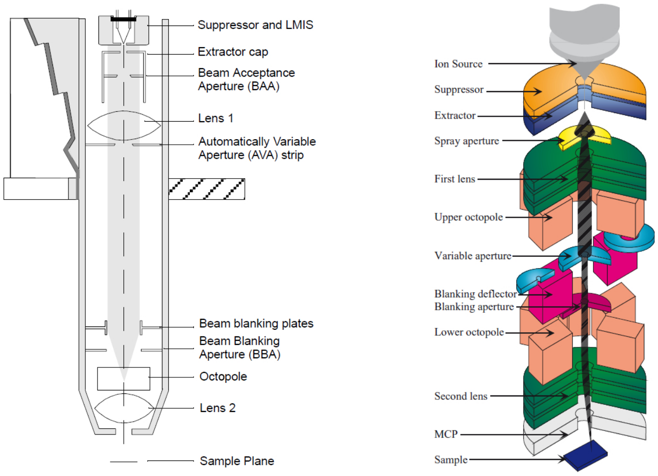

Figure 2.44: Schematic diagram of FIB ion gun column [30].

The beam is focused to a fine spot, enabling a best resolution in the sub 10 nm range. Blanking of the beam is accomplished by the blanking deflector and aperture, while the lower octopole is used for raster scanning the beam over the sample in a user-defined pattern. The multichannel plate (MCP) is used to collect secondary particles for imaging.

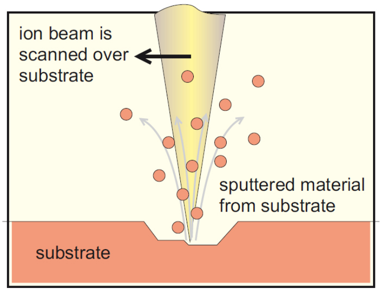

Figure 2.45: Sputtering process during the FIB lithography [30].

The removal of sample material is achieved using a high ion current beam. The result is a physical sputtering of sample material, as illustrated schematically in figure 2.45. By scanning the beam over the substrate, an arbitrary shape can be etched. Redeposition occurs, which drastically reduces the effective etch rate.

The main benefits of FIB nanofabrication are the high flexibility in the shapes that can be lithographed, and the attainable resolution (below 50 nm). The size of the structures that can be obtained is limited by the current; small structures require small current and a lot of processing time. The slow processing is the main drawback of FIB. Hence only relatively small structures (typically tens of micrometers) can be realized within a reasonable time. This technique is best suited for small-scale post-processing or prototype fabrication.

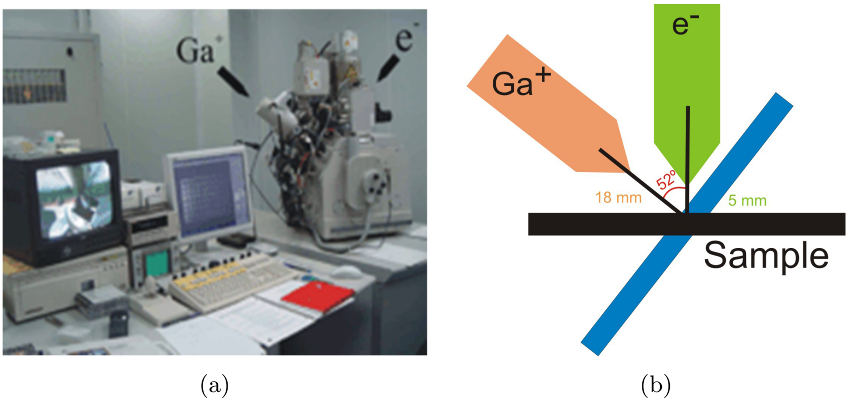

(a) (b)

Figure 2.46: (a) FIB Strata DB235 from FEI at the Nanotechnology Platform (Barcelona Science Park) and (b) schematics of the ions and electrons beams configuration.

During this thesis a dual-beam STRATA DB235 from FEI at the Nanotechnology Platform of the Barcelona Science Park (figure 2.46(a)) was used. The ion beam works at a constant energy of 30 KeV and the current has been varied between 100 pA to 1000 pA depending on the size of the nanostructure. Figure 2.46(b) shows a schematic view of the configuration of the two beams and sample position for SEM or FIB.

2.4.2 Influence of galium implantation on the magnetic properties

As previously discussed, a disadvantage of this technique is the Ga^+ implantation in the sample during the milling process. As shown in figure 2.47 some Ga^+ ions, due to their high energy are implanted in the sides of the fabricated structures (side-wall doping). Depending on the irradiation conditions, this Ga^+ implantation modifies the magnetic properties of the material as reported in references [29, 31–33].

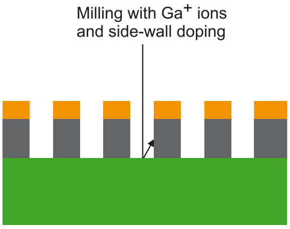

Figure 2.47: Implantation of Ga^+ in the edges of the nanostructure fabricated by FIB.

To study the effect of the implantation of Ga^+ in the Au/Fe/MgO films the FIB was used to irradiate them in twelve areas of 1.33×1.29 mm^2 with different doses by varying both the intensity and the irradiation time. Table 2.1 summarizes the irradiation conditions of the twelve areas in three different films.

Some of these irradiated areas have been characterised by synchrotron radiation XRD ($\lambda = 0.8857$ Å). These experiments were possible due to the high intensity and small size of the beam available at SpLine beamline (ESRF). These measurements allow to study whether Ga^+ implantation produces a distortion in the Fe lattice or the formation of Fe-rich Fe-Ga alloys.

Sample	Intensity (nA)	Time (min)	Dose ($\times10^{15}$ ions/cm^2)
1	0.841	10	0.21
	5.70	5	0.71
	5.68	10	1.41
	5.70	35	4.25
2	2.92	40	2.91
	6.38	20	3.18
	6.35	32	5.06
	6.34	40	6.37
3	0.932	30	0.7
	0.942	60	1.41
	0.920	120	2.85
	0.950	420	7.03

Table 2.1: Doses of Ga^+ in the irradiated thin films.

Figure 2.48 displays the equilibrium phase diagram of Fe-Ga alloys. The first stable Fe-rich alloy at room temperature is α-Fe_3Ga, which crystalline structure $L1_2$ [34] is shown in figure 2.49. It is worth to mention that implantation is an out of equilibrium process, and other Fe-Ga alloys could be formed for the same Ga concentration due to the high energy of the incoming Ga^+ and the local temperature increase. Figure 2.49 shows the crystalline structure $D0_3$ corresponding to the stable high temperature β-Fe_3Ga phase.

The diffraction patterns of these $L1_2$ and $D0_3$ structures have been simulated and compared with the experimental XRD results to get information of the presence of any contribution of Fe-Ga alloys in the samples. Assuming that only part of the Fe layer is implanted with Ga atoms and also that the majority formation of Fe-Ga alloy is $L1_2$ phase, and $D0_3$ in minor contribution, the simulated diffraction pattern should be similar to that shown in figure 2.50 (calculated for Fe 25%, $L1_2$ 60% and $D0_3$ 15%). Most Fe_3Ga Bragg peaks of these Fe_3Ga phases are very close

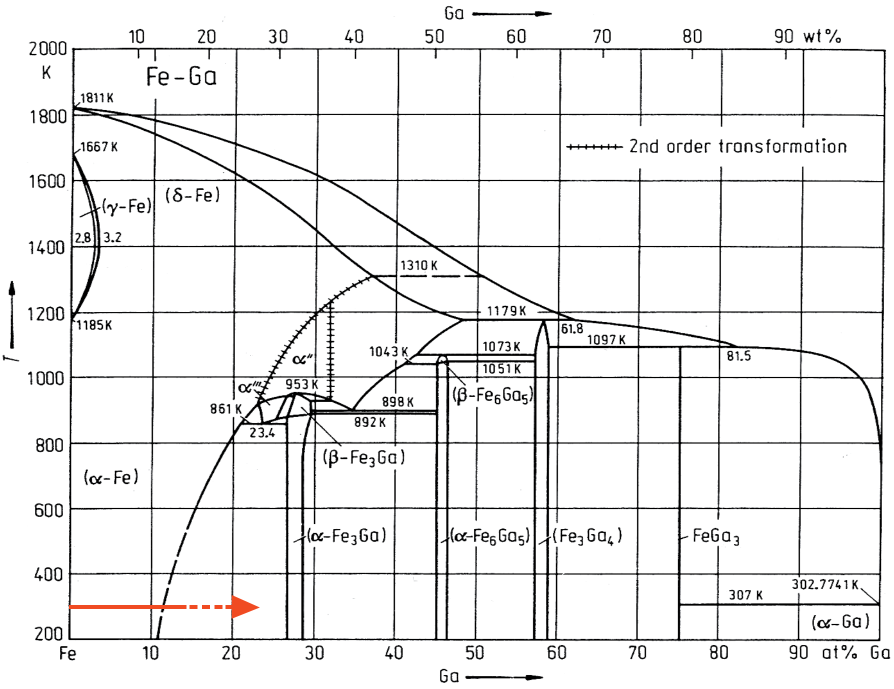

Figure 2.48: Equilibrium phase diagram of Fe-Ga alloys.

to the Fe ones, so that they are very difficult to be resolved. Both D0$_3$ and L1$_2$-Fe$_3$Ga (220) Bragg peaks overlap with MgO (200) and Au (200) of the epitaxial Au/Fe/MgO thin film, so that it would be very difficult to observed them due to the large signal of the substrate. Also the (400) peaks if a significant amount of crystalline Fe is left. However, L1$_2$-Fe$_3$Ga displays multiple Bragg peaks in the central region of the 2θ range with missing reflections of substrate and thin film, which should appear in the experimental diffraction patterns depending on its concentration.

The existence of D0$_3$ and/or L1$_2$-Fe$_3$Ga crystallines structures would lead to an asymmetry of the Fe (200) peak due to the small separation of their (400) reflections (0.14 and 0.58 degrees, respectively) as seen in figure 2.50.

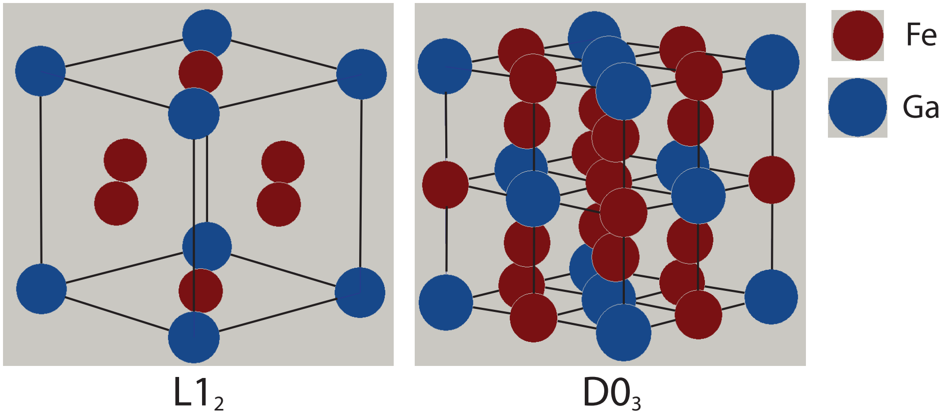

Figure 2.49: Crystalline structures of the $\alpha-$ and $\beta-$ Fe_3Ga alloys.

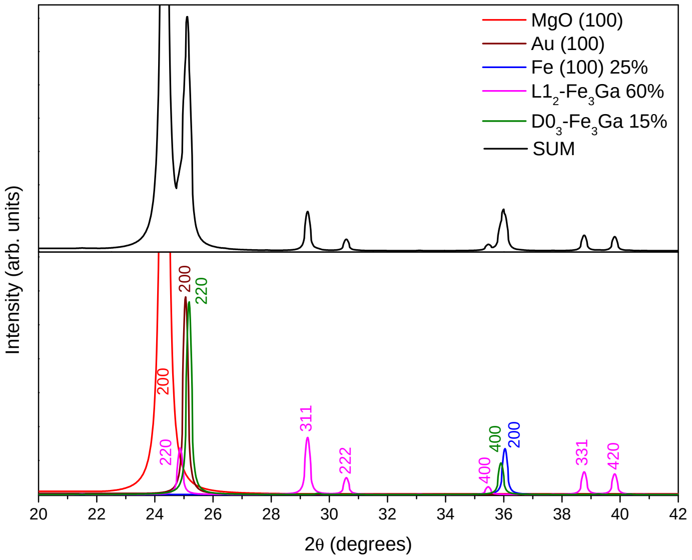

Figure 2.50: Simulated diffraction patterns of $\alpha-$ and $\beta-$ Fe_3Ga phases ($\lambda = 0.8857$ Å).

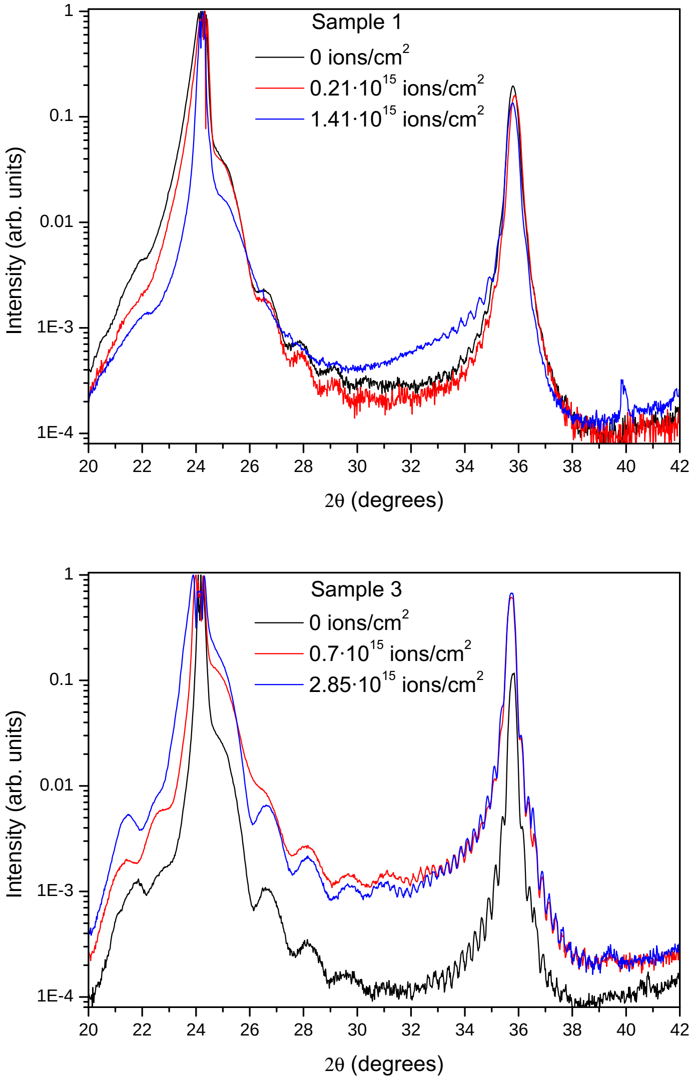

Figure 2.51: Normalized X-ray diffractograms of Au/Fe/MgO (001) samples irradiated with Ga^+.

Figure 2.51 represents a selection of XRD results of the irradiated areas with different Ga^+ doses. It is readily observed a broad contribution on the left side of the Fe (200) peak. This signal should come from induced disorder, presence of intersticials, expansion of the unit cell and nanocrystalline alloy formation, taking place during the Ga implantation process. In addition, a small peak at $2\theta \approx 40^o$ is present for doses above $2 \cdot 10^{15}$ ions cm^2, which might be assigned tentatively to the (420) Bragg peak of the $L1_2$ phase.

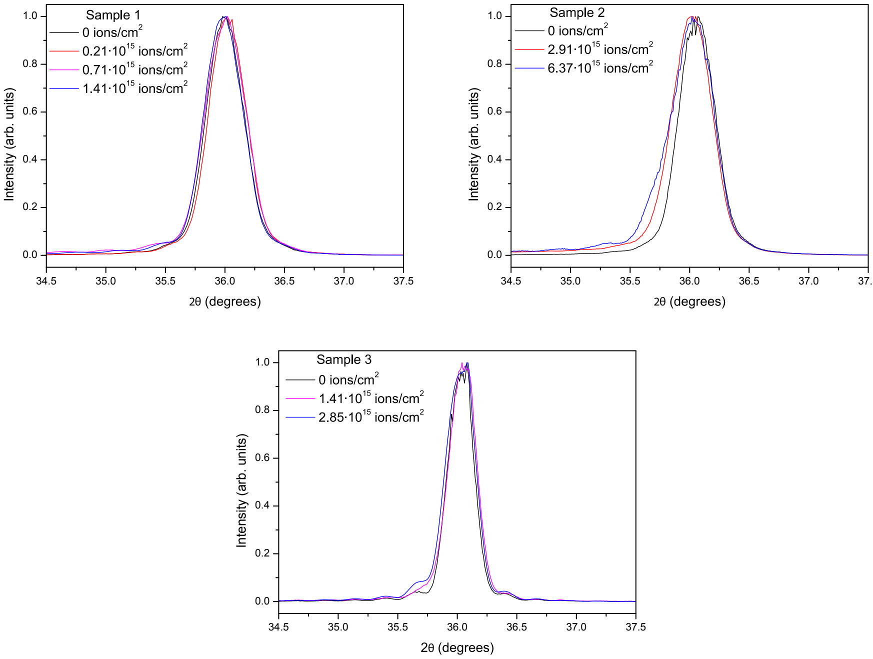

Figure 2.52: Normalized Fe (200) X-ray diffractograms of the three samples upon Ga^+ irradiation.

Figure 2.52 shows the broadening of Fe (200) peak as result of the alloy formation. This effect is more important in sample 2, for which higher values of Ga^+ intensity were used and Ga implantation reaches the maximum dose. The right side of the Fe (200) peak remains the same as Ga irradiation is performed. It means that <L_c^{Fe} > should not change and the broadening might be due to the small contribution of Fe-Ga alloy at 2θ values below the Fe (200) reflection. This peak asymmetry, towards higher lattice parameters values, might correspond to emission from (400) peak of the D0$_3$ structure, which also suggest the formation of Fe$_3$Ga D0$_3$ phase.

If one assumes that the increase of FWHM of the Fe (200) Bragg peak with Ga$^+$ dose is only due to structural modifications in the Fe layer, the variation of <L_c > calculated by Scherrer formula, equation 2.2, shows a linear decay of the perpendicular coherence length (figure 2.53). This value decreases by 2.3 nm, approximately, with respect to that of the Fe layer for non-irradiated samples.

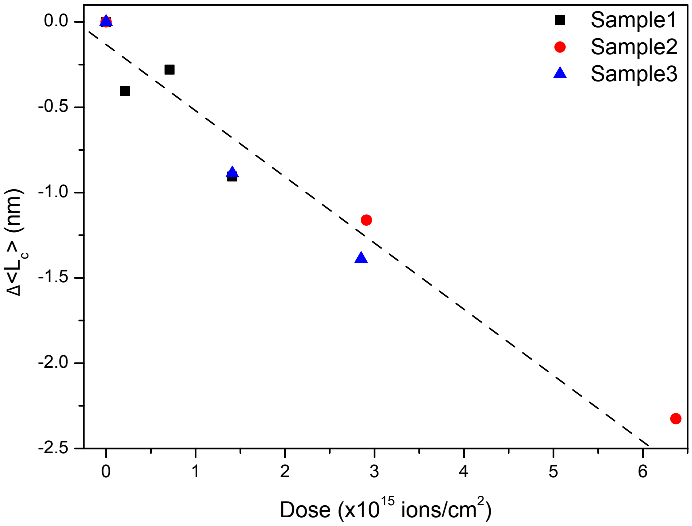

Figure 2.53: Variation of the perpendicular coherence lenght of the Fe layer in the Au/Fe/MgO(001) thin film with the Ga$^+$ dose.

XRR measurements, similarly to the experiments performed in the non-irradiated samples (figure 2.9), show very intense oscillations (figure 2.54). The period of such oscillations yields a decrease of 3.5 nm of the effective thickness, approximately, as shown in figure 2.55. This loss of effective thickness is in agreement with the value obtained for the perpendicular coherence length decrease. These results might be explained in terms of the effect of Ga sputtering and implantation. Nevertheless, some sputtering effects can not be discarded.

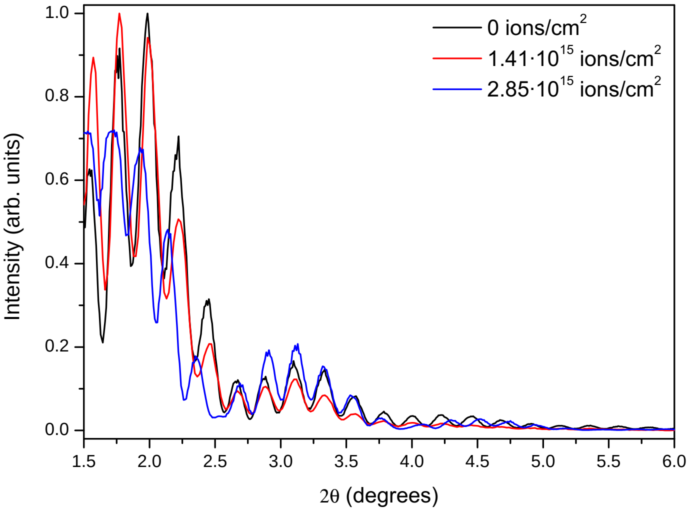

Figure 2.54: X-ray reflection diffractograms upon Ga$^+$ irradiation.

In summary, although there are not significant changes in the crystalline structure of the samples, Ga$^+$ irradiation produces some degree of structural disorder and the formation of both L1_2 and D0_3 Fe-rich FeGa alloys. This is illustrated in figure 2.56, where the oscillations with well defined periods are preserved, confirming the high quality of the irradiated Fe layer. According to these results one might expect minor effects on the magnetic properties of the Au/Fe/MgO (001) films upon Ga$^+$ exposure for the studied irradiation conditions.

As a general trend, the effects of ion irradiation of magnetic films and multilayers are quite complex and depend on the characteristic parameters of the beam, such as the mass and kinetic energy of the

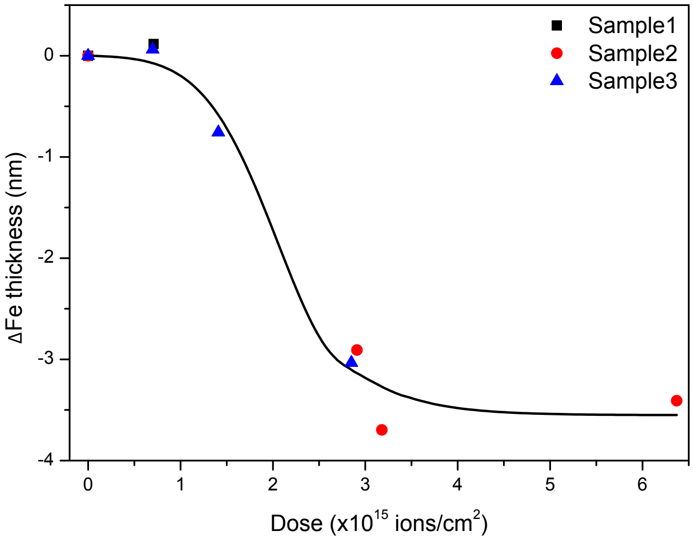

Figure 2.55: Variation of the effective thickness of the thin film with the Ga$^+$ dose.

ions and the total fluency (dose), as well as on the specific features controlling the magnetization processes: the existence of high surface, magnetoelastic anisotropy contributions or the presence of defects involved in nucleation and pinning mechanisms. In the case of systems whose magnetic properties arise from strong effects in the interfaces, the eventual disorder and intermixing induced by irradiation usually lead to a substantial modification of the magnetic anisotropy, even affecting their easy axes configuration. Substantial modifications of the anisotropy might also occur in the case of highly disordered systems, for which irradiation can improve the chemical order or even induce the formation of new phases -affecting the magnetocrystalline anisotropy- and, at the same time, relax the residual stresses, decreasing the eventual magnetoleastic anisotropy energy contributions. On the contrary, in the case of relatively ordered systems the irradiation might increase the chemical disorder and also generate new phases, usually leading to a decrease of the magnetocrystalline

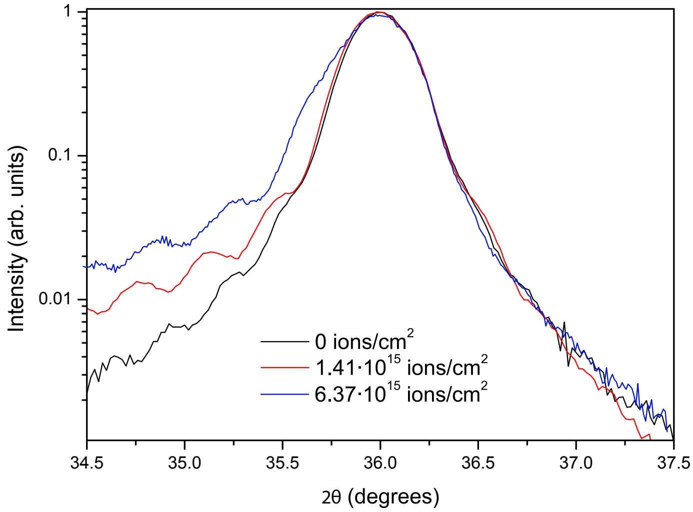

Figure 2.56: Normalized Fe (200) X-ray diffractograms in logarithmic scale of the three samples upon Ga^+ irradiation.

anisotropy but also to an increase of the density of nucleation sites and pinning defects. From all these considerations it is evident that many competing effects might take place upon irradiation that would affect the overall magnetic behaviour of a system, rendering difficult the direct interpretation of the eventual modifications of the hysteresis parameters and of the magnetization mechanisms.

In the specific case of the Fe films studied in this thesis, the effects of the Ga^+ irradiation on the coercivity, remanence and saturation field, H_{sat}, required to saturate them along the hard axis. H_{sat}, which provides an indirect measure of the K_{ani}/M_s ratio, was employed because the use of the MOKE system precluded the direct measurement of the saturation magnetization. However, the evidences of surface damage on the capping layer upon irradiation did not allow using the reflectivity as a relative measure of the saturation magnetization.

Figure 2.57 presents the hysteresis loops measured along the hard axis

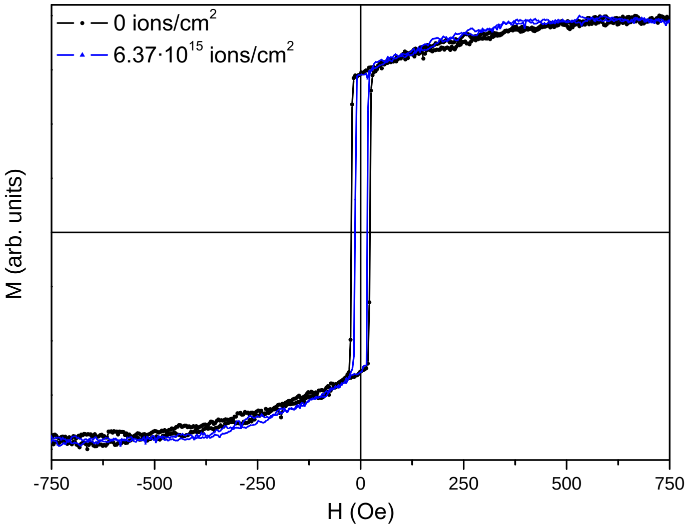

Figure 2.57: Hysteresis loops along the hard axis prior and after Ga^+ irradiation with $6.37 \cdot 10^{15}$ ions cm^{-2} dose.

of sample 2 prior to irradiation and after irradiation with the highest dose, $6.37 \cdot 10^{15}$ ions cm^{-2}, by using the highest current intensity, 6.34 nA. No differences are observed in the reversible, approach to saturation region, which indicates that H_{sat} is essentially unchanged. This, in turn, shows that the structural modifications due to the irradiation process do not largely affect the anisotropy and saturation magnetization (they are not strictly proportional to one another). The structural analysis after irradiation suggests that, at least, a given percentage of the Ga atoms implanted in the Fe films produced Fe_3Ga clusters. No evidences were found of a generalized dilution of the Ga atoms into the Fe lattice leading to a metastable and complete Fe-rich Fe-Ga alloy, although the appearance of local clusters of such an alloy are not excluded. These facts are consistent with the negligible variation of the intrinsic magnetic parameters involved in H_{sat}.

Regarding the coercivity and remanence of the films, as a first point it is important to remark that the coercivity values measured along the easy

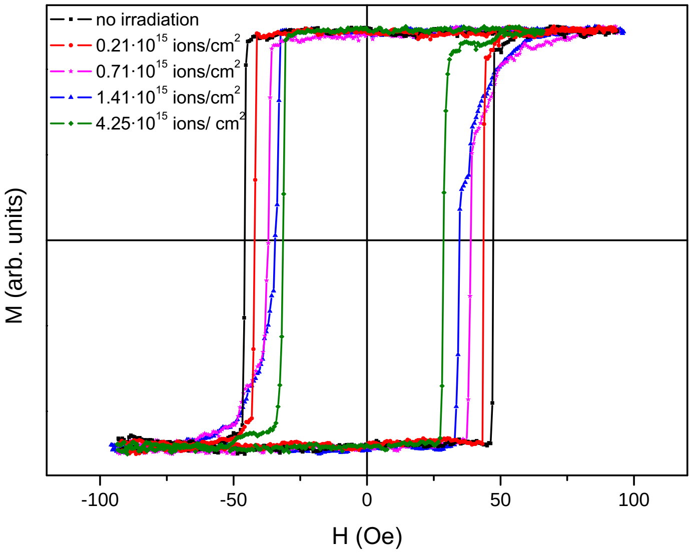

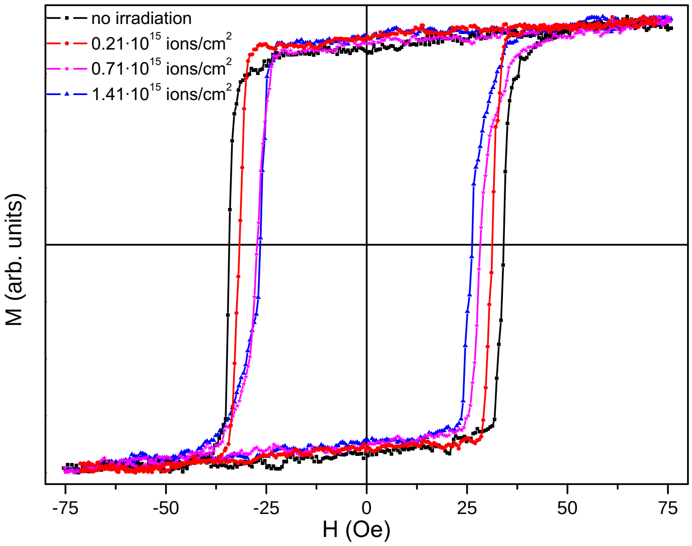

Figure 2.58: Hysteresis loops along the easy (top) and hard (bottom) axes of Ga^+ irradiated sample 1.

axis for the three Fe films were very different: 46, 23 and 11 Oe for samples 1, 2 and 3, respectively. Samples 1 and 2 evidenced the same qualitative behaviour. Figure 2.58 shows the hysteresis loops of sample 1 along the easy and the hard axis, respectively. The easy axis loop prior to saturation is square, with remanence equal to saturation, and its demagnetization branch is characterized by a single switching step that takes the magnetization from $+M_s$ directly to $-M_s$. After irradiation, the remanence remains equal to saturation; the demagnetization takes place by means of a very large irreversible step followed by a relatively broad distribution of switching events until (negative) saturation is reached. The field corresponding to the large switching step, taken as coercive field, decreases with increasing the irradiation dose. When the loops are measured along the hard axis a similar behaviour occurs, with the only difference that the remanence is in all cases equal to $0.7M_s$, approximately, due to the alignment of the magnetization along the easy axis, at 45^o with respect to the direction of the applied field.

Sample 3, which presents a weak coercivity, about 11 Oe, exhibits a very different behaviour upon irradiation. The hysteresis loops along the easy axis (figure 2.59) are also square, with remanence equal to saturation. However, in contrast to the case of samples 1 and 2, the coercivity and the very narrow switching field distribution are not modified even with doses as high as $7.03 \cdot 10^{15}$ ions cm^{-2}. It is important to remark that the irradiation of sample 3 was carried out with very low current intensity, about 0.9 nA, even for the highest doses (see table 2.1).

The magnetic parameter most sensitive to changes is the coercivity H_c, because it depends strongly on the defect and grain structure and the internal strains of the specimen. In addition, impurities incorporated during deposition or ion implantation can increase H_c. Muller *et al.* [35] showed a strong reduction in coercivity during the initial stage of irradiation in electron-gun deposited films, that may be explained by the reduction in the intrinsic stress; and an increase in H_c after high-fluence ion irradiation, that

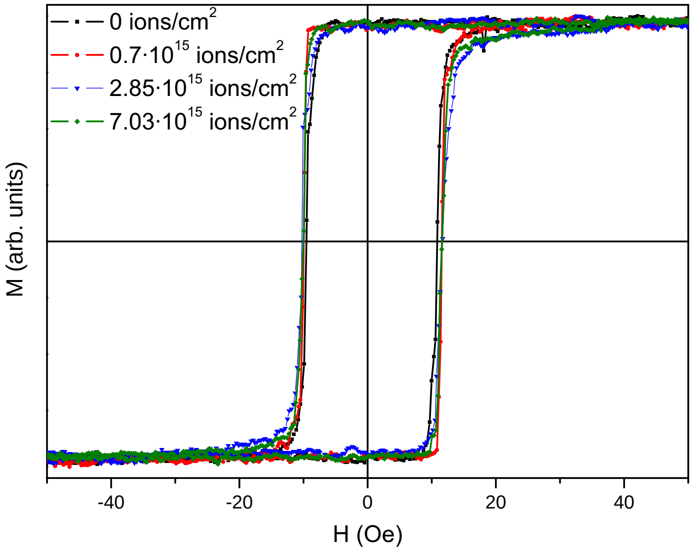

Figure 2.59: Hysteresis loops along the easy axis of Ga^+ irradiated sample 3.

might be correlated to the large number of impurities generating pinning centres in the damage cascades.

The behaviour of the coercivity of the three films is summarized in figure 2.60. For samples 1 and 2 it decreases with increasing dose, about 37% and 43%, respectively, for the highest dose employed, whereas it remains constant for sample 3. In the frame of a magnetization reversal mechanism triggered by the nucleation of reversed nuclei, at regions with reduced energy barriers, the decrease of the nucleation field H_n required to launch the switching events can be tentatively interpreted as due to the generation of local highly disordered centres. Their reduced magnetocrystalline anisotropy, due to the loss of crystalline quality, would easy their magnetization reversal. The long sequence of jumps that conforms the broad switching field distribution of the demagnetization curve is probably linked to the generation of defects involved in the pinning

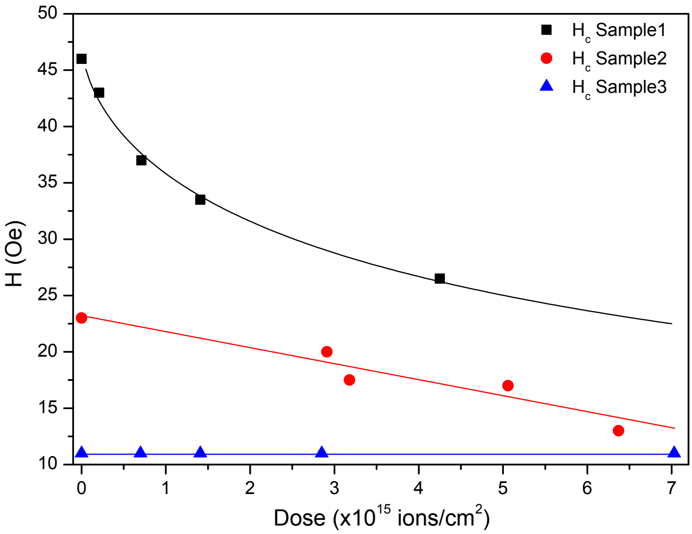

Figure 2.60: Variation of the coercive field of the Au/Fe/MgO (001) thin films with the Ga^+ dose.

of the propagating walls. The defects with associated pinning fields below the nucleation field value are obviously not effective in impeding the wall propagation. In the case of sample 3, the negligible modifications of the hysteresis parameters suggest that the low current employed during the irradiation process leads neither to the formation of the nucleation centres nor to the defects involved in pinning. This interpretation is consistent with the broadening at the low θ side of the Fe (002) reflection just for samples 1 and 2, but not for sample 3, as can be seen by comparing the Fe (200) Bragg peak of the three samples in figure 2.52.

2.4.3 Electron Beam Lithography

The Electron Beam Lithography consist of scanning a fine focused beam of electrons across a surface covered with a resist film sensitive to those electrons, thus depositing energy in the desired pattern in the resist film.

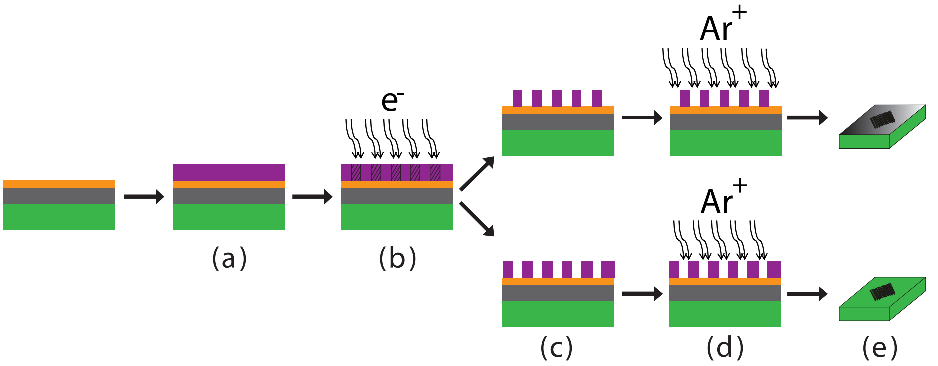

Figure 2.61: Scheme of the processes involved in the EBL (a) deposition of the photoresist; (b) electron irradiation of the pattern; (c) development; (d) ion etching; (e) lift-off (Positive resist in the upper and negative resist in the lower part, respectively).

This technique involves a multistep process where either the chemical composition of the sample or its crystalline structure can be modified as shown in figure 2.61:

(a) Deposition of the photosensitive resist, positive (PMMA) or negative (AZ nLOF 2070)

(b) Electron irradiation. In the positive resist it breaks polymer backbone bonds, leaving fragments of lower molecular weight, more soluble in the developer. In the negative resist it cause a cross-linking of the polymer chains, rendering them less soluble in the developer.

(c) Development. It dissolves the more soluble part of the resist, leaving the non-irradiated part in the positive resist and the irradiated part in the negative one.

(d) Ion etching. The resist left in the sample works as a mask, removing the part of the sample not covered with resist.

(e) Lift-off. Removes the resist left after the process, leaving the pattern

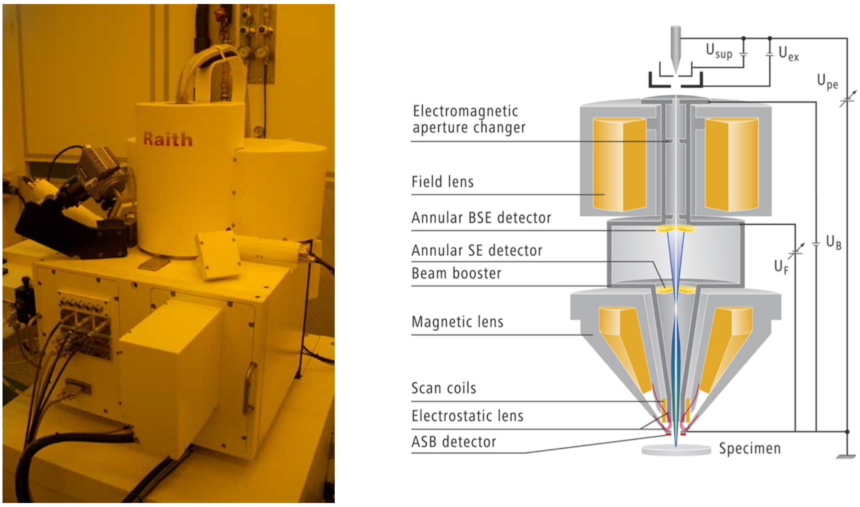

(a) (b)

Figure 2.62: (a) Raith e-LiNE at the Nano+Bio Center of the Technical University of Kaiserslautern and (b) Schematic drawing of the Zeiss GEMINI field emission column: U1 - extractor voltage at first anode, U0 - accelerator voltage at second anode, UB - booster voltage.

clean.

An electron beam lithography tool Raith e-LiNE system located at the Nano+Bio Center of the Technical University of Kaiserslautern, has been used to fabricate the patterns (nanowires, antidots). More details are given in section 3.2. Figure 2.62 illustrates a schematic drawing of the Raith e-LiNE electron column (Zeiss GEMINI), the main components of which are the electron source and the magnetic lenses for focusing the beam. The electron source is a thermionic emission element (a Schottky thermionic field emission, SFE). The SFE combines the high brightness and low energy spread of the cold field emitter with high stability and low beam noise. The special electron beam path inside the Gemini column has been designed to eliminate beam cross-over and ensure a field free specimen area.

Bibliography

[1] C. Pasquini, J. Cortez, L. M. C. Silva and F. B. Gonzaga, *"Laser induced breakdown spectroscopy"* Journal of the Brazilian Chemical Society **18** (3) 463–512 (2007).

[2] T. J. Jackson and S. B. Palmer, *"Oxide superconductor and magnetic metal thin-film deposition by pulsed-laser ablation - a review"* Journal of Physics D: Applied Physics **27** (8) 1581–1594 (1994).

[3] S. Lampman, *Weld integrity and performance: a source book adapted from ASM international handbooks, conference proceedings, and technical books ASM Handbook Series.* ASM International (1997).

[4] A. Jacquot, B. Lenoir, M. O. Boffoué and A. Dauscher, *"Pulsed laser deposition of PbTe films on glass substrates"* Applied Physics A: Materials Science & Processing **69** **[Supl.]** (7) S195–S199 (1999).

[5] C. Martínez Boubeta, J. L. Costa-Krämer and A. Cebollada, *"Epitaxy, magnetic and tunnel properties of transition metal/MgO(001) heterostructures"* Journal of Physics: Condensed Matter **15** (25) R1123–R1167 (2003).

[6] I. K. Schuller, *"New class of layered materials"* Physical Review Letters **44** (24) 1597–1600 (1980).

[7] W. Sevenhans, M. Gijs, Y. Bruynseraede, H. Homma and I. K. Schuller, *"Cumulative disorder and X-ray-line broadening in multilayers"* Physical Review B **34** (8, Part 2) 5955–5958 (1986).

[8] E. E. Fullerton, I. K. Schuller, H. Vanderstraeten and Y. Bruynseraede, *"Structural refinement of superlattices from X-ray diffraction"* Physical Review B **45** (16) 9292–9310 (1992).

[9] B. D. Cullity, *Elements of X-Ray diffraction.* Addison-Wesley Publishing, New York (1967).

[10] C. Martínez Boubeta, E. Navarro, A. Cebollada, F. Briones, F. Peiró and A. Cornet, *"Epitaxial Fe/MgO heterostructures on GaAs(001)"* Journal of Crystal Growth **226** (2-3) 223–230 (2001).

[11] D. P. Woodruff and T. A. Delchar, *Modern techniques of surface science.* Cambridge Solid State Science Series, Second ed. (1994).

[12] J. Rubio Zuazo, *Synchrotron X-ray radiation applied to the study of thin films: The case of* $La_{0.7}Ca_{0.3}MnO_3/SrTiO_3$*(001).* PhD thesis, Universidad Autónoma de Madrid (2005).

[13] E. Vlieg, *"ROD: a program for surface X-ray crystallography"* Journal of Applied Crystallography **33** (2) 401–405 (2000).

[14] W. F. Kolbe, D. F. Ogletree and M. Salmeron, *"Atomic force microscopy imaging of T4 bacteriophages on silicon substrates"* Ultramicroscopy **42-44** 1113 (1992).

[15] T. Yoshinobu, A. Iwamoto and H. Iwasaki, *"Scaling analysis of* SiO_2/Si *interface roughness by atomic force microscopy"* Japanese Journal of Applied Physics **33** (Part 1, No. 1B) 383–387 (1994).

[16] I. Horcas, R. Fernández, J. M. Gómez-Rodríguez, J. Colchero, J. Gómez-Herrero and A. M. Baró, *"WSxM: A software for scanning probe microscopy and a tool for nanotechnology"* Review of Scientific Instruments **78** (1) 013705 (2007).

[17] M. J. Freiser, *"A survey of magnetooptic effects"* IEEE Transactions on Magnetics **4** (2) 152–161 (1968).

[18] R. Lopusnik, *Time resolved magneto-optical investigations of magnetization dynamics in iron garnet films.* PhD thesis, Universität Kaiserslautern (2001).

[19] U. Ebels, A. O. Adeyeye, M. Gester, R. P. Cowburn, C. Daboo and J. A. C. Bland, *"Anisotropic domain evolution in epitaxial Fe/GaAs(001) wires"* Physical Review B **56** (9) 5443–5451 (1997).

[20] F. Cebollada, A. Hernando-Mañeru, A. Hernando, C. Martínez Boubeta, A. Cebollada and J. M. González, *"Anisotropy, hysteresis, and morphology of self-patterned epitaxial Fe/MgO/GaAs films"* Physical Review B **66** (17) 174410 (2002).

[21] C. Salvador, T. Freire, C. G. Bezerra, C. Chesman, E. A. Soares, R. Paniago, E. Silva-Pinto and B. R. A. Neves, *"Properties of*

Fe/MgO(100) nanometric films grown by dc sputtering" Journal of Physics D: Applied Physics **41** (20) 205005 (2008).

[22] J. L. Costa-Krämer, J. L. Menéndez, A. Cebollada, F. Briones, D. García and A. Hernando, *"Magnetization reversal asymmetry in Fe/MgO(001) thin films"* Journal of Magnetism and Magnetic Materials **210** (1-3) 341–348 (2000).

[23] S. Foner, *"Versatile and sensitive vibrating-sample magnetometer"* Review of Scientific Instruments **30** (7) 548–557 (1959).

[24] G. Counil, J. V. Kim, T. Devolder, P. Crozat, C. Chappert and A. Cebollada, *"Magnetic anisotropy of epitaxial MgO/Fe/MgO films studied by network analyzer ferromagnetic resonance"* Journal of Applied Physics **98** (2) 023901 (2005).

[25] C. Kittel, *"On the theory of ferromagnetic resonance absorption"* Physical Review **73** (2) 155–161 (1948).

[26] Kh. Zakeri, Th. Kebe, J. Lindner and M. Farle, *"Magnetic anisotropy of Fe/GaAs(001) ultrathin films investigated by in situ ferromagnetic resonance"* Journal of Magnetism and Magnetic Materials **299** (1) L1–L10 (2006).

[27] F. J. Dyson, *"Electron spin resonance absorption in metals. II. Theory of electron diffusion and the skin effect"* Physical Review **98** (2) 349–359 (1955).

[28] J. F. Walker, J. C. Reiner and C. Solenthaler, *"Focused ion beam sample preparation for TEM"* in Microscopy of Semiconducting Materials 1995 (Oxford, England, 20-23 March) **146** 629–634 (1995).

[29] Ll. Balcells, Ll. Abad, H. Rojas and B. Martinez, *"Material damage induced by nanofabrication processes in manganite thin films"* Nanotechnology **19** (13) 135307 (2008).

[30] S. Reyntjens and R. Puers, *"A review of focused ion beam applications in microsystem technology"* Journal of Micromechanics and Microengineering **11** (4) 287–300 (2001).

[31] C.-M. Park and J. A. Bain, *"Local degradation of magnetic properties in magnetic thin films irradiated by Ga$^+$ focused-ion-beams"* IEEE Transactions on Magnetics **38** (5, Part 1) 2237–2239 (2002).

[32] S. Blomeier, D. McGrouther, R. O'Neill, S. McVitie, J. N. Chapman, M. C. Weber, B. Hillebrands and J. Fassbender, *"Modification of the magnetic properties of exchange coupled NiFe/FeMn films by* Ga^+ *ion irradiation"* Journal of Magnetism and Magnetic Materials **290-291** (Part 1) 731–734 (2005).

[33] R. Gupta, K.-H. Han, K. P. Lieb, G. A. Müller, P. Schaaf and K. Zhang, *"Influence of ion implantation on the magnetic properties of thin FeCo films"* Journal of Applied Physics **97** (7) 073911 (2005).

[34] N. Srisukhumbowornchai and S. Guruswamy, *"Influence of ordering on the magnetostriction of Fe–27.5 at. % Ga alloys"* Journal of Applied Physics **92** (9) 5371–5379 (2002).

[35] G. A. Müller, E. Carpene, R. Gupta, P. Schaaf, K. Zhang and K. P. Lieb, *"Ion-beam induced changes in magnetic and microstructural properties of thin iron films"* European Physical Journal B **48** (4) 449–462 (2005).

3

Nanowires

3.1 Introduction

Planar nanowires fabricated by different patterning procedures in continuous films grown by deposition techniques such as sputtering, molecular beam epitaxy (MBE) or pulsed laser deposition (PLD) lead to different scenarios for their magnetization reversal mechanisms [1–7]. Very different mechanisms may occur in nanowires with similar dimensions depending on:

1. Their specific intrinsic parameters, basically magnetocrystalline anisotropy energy (MAE) and saturation magnetization M_s.
2. Their structural and morphological features, which include, among others, their single or polycrystalline character, textures and aspect ratio.
3. The quality of the nanowire-substrate interface (roughness, interdiffusion of chemical species, eventual presence of stresses due to the lattice mismatch...)
4. Other factors such as residual stresses, impurities or defects inherent to the fabrication technique.

One of the main issues of these mechanisms is the presence of either quasi-uniform or non-uniform magnetization configurations associated with the reversal. As an example, the reversal of nanowires based on low anisotropy materials such as permalloy evolves with increasing wire thickness from coherent rotation to more complex mechanisms based on non-uniform magnetization [3]. Different mechanisms take also place in polycrystalline cobalt nanowires with widths between 30 nm and 2 μm. While the reversal of the widest wires is accomplished through the generation of a multidomain state, that of narrower ones is due to the propagation and pinning of walls nucleated at the ends of the wires, these two mechanisms are represented in figure 3.1.

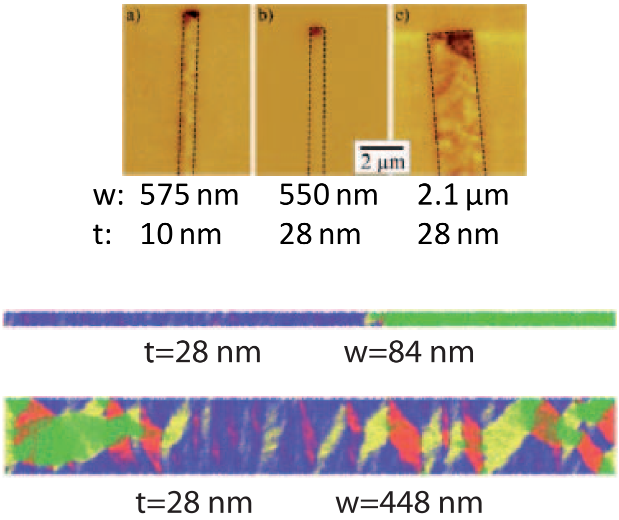

Figure 3.1: MFM images and simulations of the reversal processes of Co nanowires were t is the thickness and w the width of the wire [4].

Figure 3.2 represents the “phase” diagram of the switching mechanism of Co nanowires as a function of their thicknesses and widths [4]. The crossover from nucleation-propagation to multidomain-based reversal occurs for widths between 200 and 700 nm, approximately, when the thickness increases from 15 to 30 nm, respectively. This transition has a linear behaviour in the “phase” diagram. For a given thickness the reversal process is based on a single domain structure for narrow wires and it changes to multidomain when the width increases; the width value at which this change occurs increases with the thickness.

On the other hand, the magnetization processes of singlecrystalline Fe wires are strongly dependent on their crystalline orientation relative to the axis of the wires. In epitaxial Fe (001) wires with the long axis, called *es* in figure 3.3, along the magnetocrystalline hard axis (Fe (110)) and widths in the micrometer range, the magnetization reversal process takes place through a nucleation and propagation mechanism controlled by the

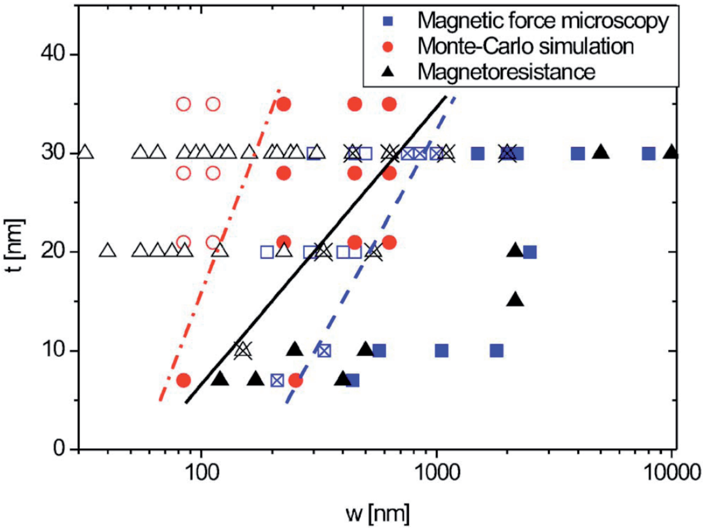

Figure 3.2: Phase diagram of the switching mechanisms of Co nanowires as a function of their thicknesses and widths. Experimental findings from magnetoresistance measurements (triangles) and MFM imaging (squares) are compared to theoretical values obtained from Monte Carlo simulation (circles). Note that MFM was only performed in remanence. The lines indicate the transition from multidomain switching (full symbols) to a reversal process by domain nucleation and propagation (open symbols) [4].

local edge dipolar fields and the four-fold in-plane anisotropy, for applied fields parallel to the axis of the wires, switching to a multidomain mediated reversal for perpendicular fields [5]. Scanning Kerr microscope images of the domain patterns for nanowires with thickness t=30 nm, length l = 500 μm, width w = 15 μm and distance between the wires d = 8 μm, are represented in figure 3.3. The contrast in the H_{c1}^{hs} , H_{c1}^{es} images is due to changes in the magnetization component parallel to the applied field ($M_{||}$), when the field is applied perpendicular and parallel to the wires respectively.

In the case of epitaxial nanowires fabricated from Fe (110)/GaAs (110) films with widths of the order of hundreds of nanometers a high, well defined uniaxial in-plane anisotropy results from the superposition of the MAE

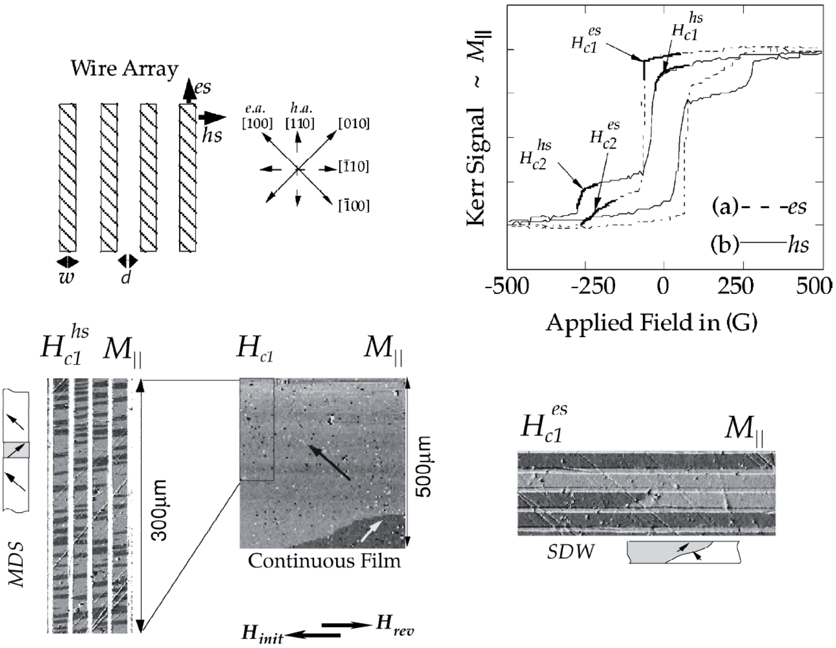

Figure 3.3: Scanning Kerr microscope images of the reversal processes of Fe epitaxial nanowires (t=30 nm, l = 500 μm, w = 15 μm, d = 8 μm) [5].

and a contribution due to the stress generated by the lattice mismatch at the interface. When its easy axis is perpendicular to the wires, and for sufficiently wide wires, the remanent magnetization can be stabilized perpendicular to the wires. The magnetization switching processes that spring out from the competing magnetostatic and anisotropy energy terms are also mediated by the formation of multidomain structure. The Object Oriented MicroMagnetic Framework (OOMF) simulations of these reversal processes are represented in figure 3.4 [6].

In this chapter the magnetization reversal processes of Fe nanowires lithographed in highly epitaxial Au(001)/Fe(001)/Mg(001) thin films by using two different techniques, electron and focused ion beam lithographies (EBL and FIB, respectively), are going to be analysed. For this

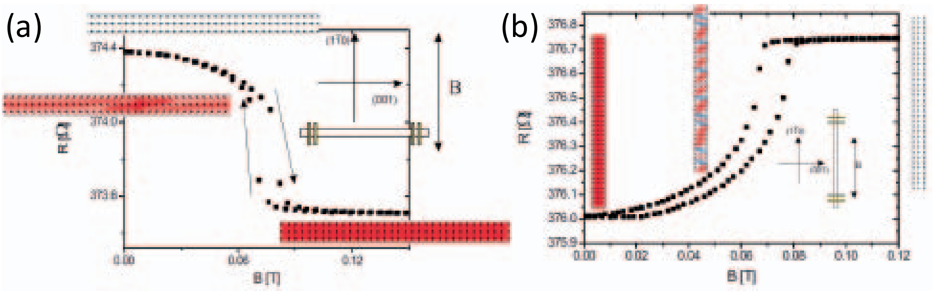

T=4.2 K; w=2 μm T=4.2 K; w=2 μm

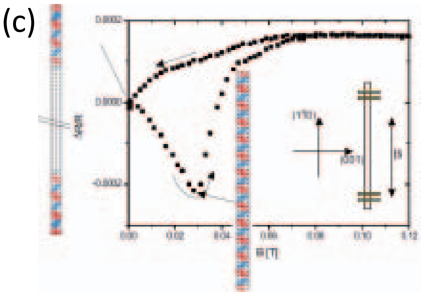

T=4.2 K; w=250 nm

Figure 3.4: Magnetoresistance curves and OOMF simulations of the reversal processes of Fe (110) epitaxial nanowires [6].

purpose different studies were carried out: the coercivity and the angular dependence of the reversal processes, FMR and scanning transmission X-ray microscopy (STXM). Special emphasis was put on the influence of the lithography techniques on the reversal processes.

3.2 Fabrication

During this thesis three different types of lithography have been used for the nanowire fabrication, as explained in section 2.4. All the nanowires have been lithographed with the Fe easy magnetocrystalline axes parallel and perpendicular to the axis of the wire, which is coincident with the Fe (010) direction (and MgO (010)).

First, a set of arrays were lithographed by FIB. The ion beam had an energy of 30 kV, and its intensity depends on the size of the structure. The nanowires made in this work were lithographed with two different currents, 1000 pA when both the width of the wires and the separation between them are 500 nm or larger, and 300 pA when at least one of the dimensions is smaller.

The FIB lithographed arrays cover an area of 400×450 μm^2 with wires of different widths (w) and distance between them (d). After the lithography of the nanowires a frame 3 μm wide was lithographed surrounding the patterned area using an intensity of 3000 pA, leaving the nanowires isolated from the continuous thin film.

For the positive resist EBL process, photoresist 950K poly-methyl methacrylate (PMMA) was used in ethyl-lactate at a concentration of 4%, spin coated at 300 rpm and baked at 180 ^{o}C for 20 minutes, which provides a 200 nm thick layer of photoresist. Then, a 5 nm thick layer of Cr was deposited, making the surface conductive so it is possible to lithograph without charge problems. For the e-beam irradiation the beam was accelerated at 20 kV with an intensity of 0.15 nA, irradiating a 200 μC cm^{-2} dose. After the irradiation a 20 s treatment with a crometch was carried out to get rid of the Cr layer. The development was performed for 20 s in MIBK:IPA 1:3 and 20 s in pure IPA, removing the irradiated resist.

Once the photoresist was developed an ion beam etching (IBE) was performed, in a base pressure of $5.5 \cdot 10^{-4}$ mbar to avoid contamination, with an ion beam of Ar$^+$ accelerated at 500 V with an intensity of 64 mA for 45 s, to sputter the part of the thin film that was not covered with photoresist. During the IBE the thin film was tilted 66^o with respect to the ion beam to avoid the retrodeposition of the sputtered material, and it was kept rotating at 10 rpm for a more uniform etching. After this process the thin film was immersed in acetone for the lift-off of the remaining photoresist. It was rinsed in deionized water and blown with dry N_2 to finish the cleaning.

In this case the patterned area is surrounded by the thin film, the ends of the wires are not isolated so that the thin film may have some influence in the magnetic properties of the nanowires. With this procedure a 2×2 mm^2 area of wires was obtained.

The last set of nanowires was performed by EBL with negative resist. The thin film was spin coated with AZ nLOF 2070 (Microchemicals), thinned down with AZ EBR solvent (Microchemicals) 2:1 at 6000 rpm, then it was baked at 100 ^{o}C for 2 minutes, providing a 260 nm thick layer of photoresist, and a Cr layer was growth to avoid charge problems. The e-beam lithography was performed at 20 kV with a beam current of 18 nA, irradiating a dose of 18 μC cm^{-2}. After the e-beam irradiation a 20 s treatment with a crometch was carried out to get rid of the Cr layer, and an image reversal step, that consists of a post-exposure bake at 110 ^{o}C for 1 minute, was done to harden the irradiated resist. The development was made with MIF726 for 30 s, rinsed in deionized water and blown with dry N_2, leaving the resist that was not irradiated.

The dry etch via IBE is performed under the same conditions as the positive resist. For the lift-off of the resist the thin film was soaked in 1-Methyl 2-Pyrrolidone (NMP) for 15 hours and in an ultrasound bath for 3 minutes. Finally, it was rinsed in deionized water and blown with dry N_2 to finish the cleaning.

With this procedure the 2×2 mm^2 patterned area remains isolated with no iron from the thin film around it.

In table 3.1 the dimensions of the arrays made by the different techniques are detailed: width of the nanowires (w) and distance between them (d).

w (nm) **d (nm)**	**100**	**200**	**500**	**1000**
140	FIB		EBL Neg	
200		EBL Neg	EBL Neg	
300			EBL Neg	
500	FIB	EBL Neg	FIB EBL Pos	FIB
1000			EBL Neg	

Table 3.1: Dimensions of the nanowires and lithography technique used.

3.3 Structural characterization

Morphological and crystalline structural characterization of the nanowires have been performed by AFM and SEM and reciprocal space maps, respectively.

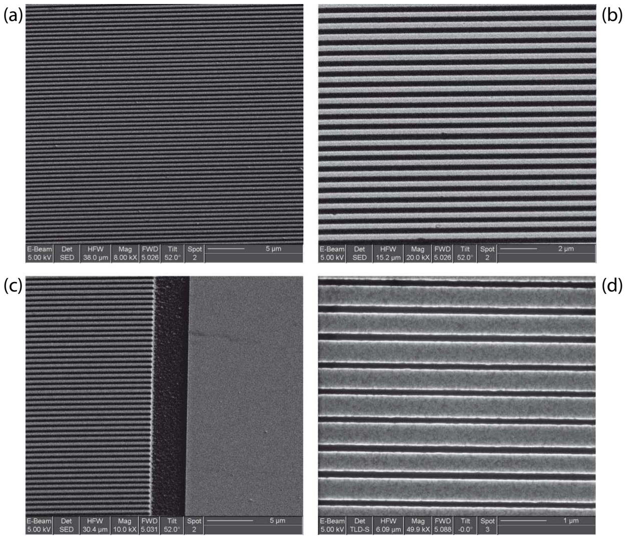

Figure 3.5: SEM images of different nanowires arrays fabricated by FIB.

SEM experiments have been made with the e-beam of the dual beam

FIB system after lithography. In figure 3.5 four SEM images of the nanowires taken at different magnifications are shown: (a) large area image evidences the continuity of the nanowires and the long range repetitive structures; (b) Closer view to inspect the quality of the edge and trench of the nanowires showing a few defects on them; (c) Detail of the end of the end of the nanowires in contact with the frame to isolate them from the continuous film; (d) Nanowires of 500 nm width and 100 nm separation (the smallest distance between nanowires fabricated with FIB, confirming the good resolution of the FIB and good quality of the wires.

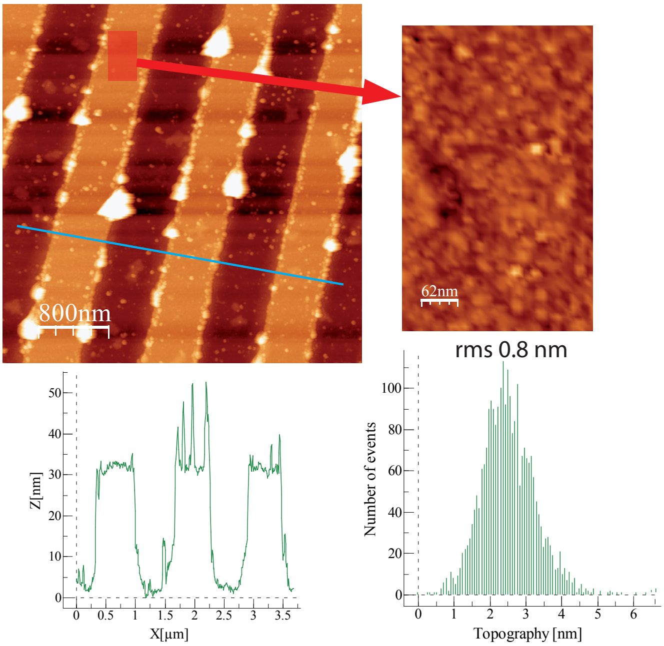

Figure 3.6: AFM image of w=d=500 nm nanowires array.

The arrays fabricated by EBL were observed by AFM. As an example figure 3.6 shows the image of one of the w=d=500 nm array. Bright spots correspond to rests of resit left after fabrication of the array. The rests were minimized with the cleaning after the lithography, but it was not possible to get rid of the resist completely. A zoom image taken on the nanowires yields a rms roughness of 0.8 nm verifying the high flatness of the wires even upon several steps done during EBL process.

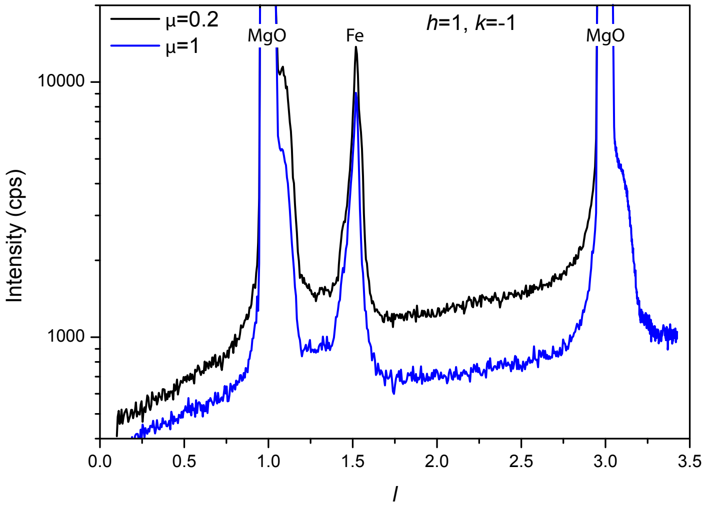

Figure 3.7: l-scans of w = d = 200 nm nanowires (a) (1-1l) (b) (22l).

The structural characterization of the nanowire array with w = d = 200 nm made by EBL with negative resist has been performed by measuring l-scans and reciprocal space maps with synchrotron radiation. These experiments have been carried out at SpLine beamline (ESRF) with the same experimental conditions as those of Au/Fe/MgO (001) thin film already explained in section 2.2.2. Figure 3.7 displays l-scan measurement for the reciprocal space point $h = 1$, $k = -1$ taken at two different incidence angles. This l-scan ($h = 1$, $k = -1$) shows the characteristic signal from Fe ($l = 1.5$) and Au ($l = 1.1$ and $l = 3.3$) similarly to the results obtained for the continuous Au/Fe/MgO (001) thin film. It turns out that the array fabrication does not destroy the good crystallinity present in the epitaxial thin film, even for the extreme case of nanowires with very little amount of material due to the small values of width (200 nm) and separation (200 nm) of this structures.

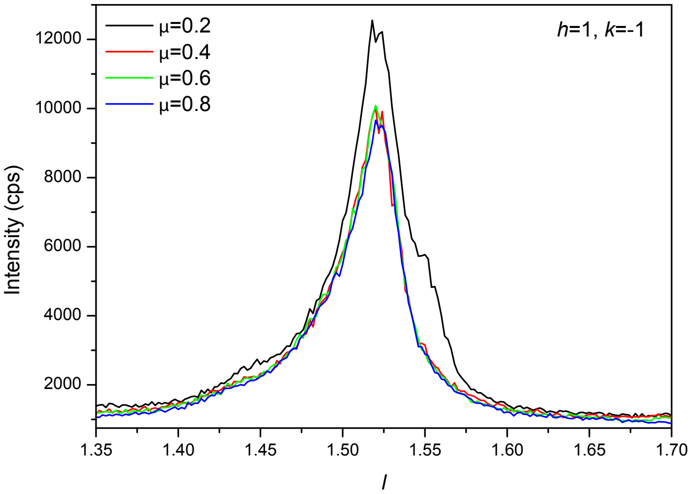

Figure 3.8: Fe peak of the l-scan (1-1l) with four different incident angles.

Figure 3.8 a detailed l-scan of the Fe peak for $h = 1$, $k = -1$ measured at four different incident angles, $\mu = 0.2$, 0.4, 0.6 and 0.8^o. In the case of surface sensitive conditions reached at the incidence angle $\mu = 0.2^o$, there exists a second contribution to the main single peak observed at higher incidence angles. This result was clearly obtained for the continuous eptaxial thin film, although it is not so well resolved in the present case. This second peak was discussed in terms of the contraction of the perpendicular lattice parameter in the atomic planes of the near region at the Fe/Au interface. This fact also confirms the apparent negligible modification of the crystalline structure upon lithography.

To study in detail any possible disorder induced by lithography processes in the central region f the Fe layer, RSMs with "bulk" sensitivity are measured. This experiments might be more sensitive to crystalline changes due to the large amount of material which maintains a relaxed structure with lattice constant values of the bulk Fe.

Figure 3.9 displays RSM of Fe (101), Fe (112) and MgO (111) taken at

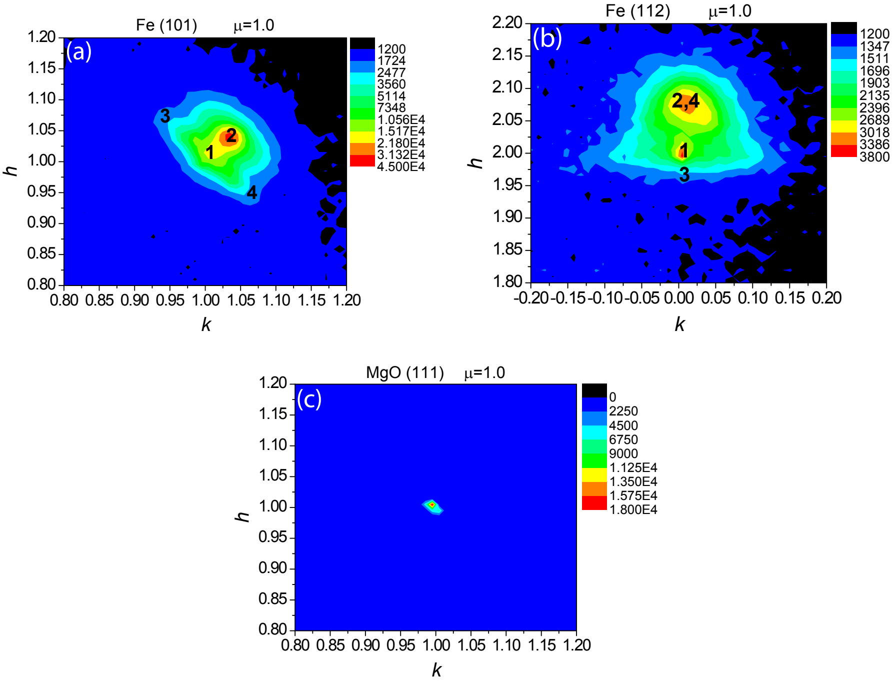

Figure 3.9: Reciprocal space maps of different families of planes: (a) Fe (101) and (b) Fe (112) in logarithmic scale; and (c) MgO (111).

$\mu = 1^o$. The comparison of these maps with those of the continuous thin film (figure 2.19) and 2.19(b)) reveals that the epitaxial nature is preserves, although minor disorder effects are not excluded. The Fe RSMs of the nanowires present the same four features as the thin film. However, there is an additional signal surrounding the most intense one, which means a wider distribution of the Fe (101) and Fe (112) planes. This fact can be clearly observed in figure 3.10 where nanowires and thin film Fe (101) RSM and line-scan profiles are shown.

In summary, although some distortion of the lattice is present due to the disorder induced during lithography, their second order effects do not produce significant changes. Nevertheless, expected and apparent

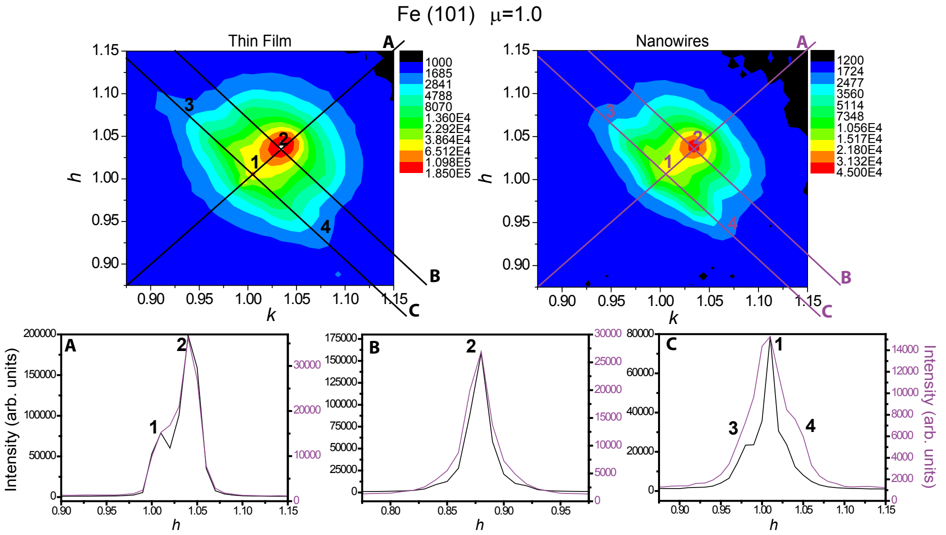

Figure 3.10: Reciprocal space maps of Fe (101) of the thin film and the nanowires (w=d=200 nm). Line profiles comparison across certain position of the RSMs.

destructive effects of the lithography might strongly modify not only the crystalline structure on the edges of the wires but also the chemical composition due to the oxidation of their Fe atoms exposed to air.

3.4 Magnetic characterization

3.4.1 Hysteresis behaviour

For the characterization of the hysteresis behaviour the most used technique has been the vectorial Kerr effect, which can measure the arrays surrounded by Fe film because it is a local technique that measures the area illuminated by the laser. Even though the laser is focused to a spot of 300 μm diameter, smaller than the arrays, the hysteresis loops measured for the arrays lithographed by FIB or EBL with positive resist have some signal from the continuous film. In the particular case of the arrays made by EBL with negative resist there is no contribution from the continuous film, and these arrays have been used to study the temperature dependence of the hysteresis with the VSM.

In this section it is presented the angular dependence of the hysteresis behaviour as well as its dependence on the lithography technique employed. Its evolution with the temperature of the EBL with negative resist arrays is also presented.

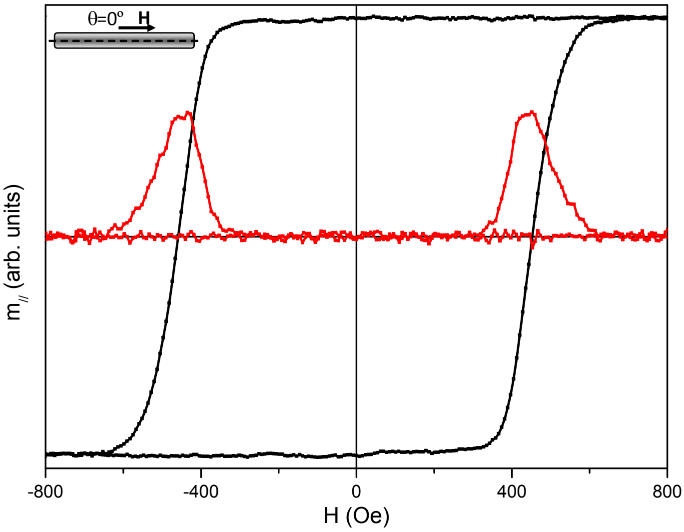

Figure 3.11: Hysteresis loop along the nanowires with w = 200 nm, d = 500 nm and its SFD.

The coercivity of the arrays, measured with the field applied along the long axis of the wires goes up to hundreds of Oe and presents a broad switching field distribution (SFD), in contrast to the thin film with coercivity around 40 Oe and a SFD of 1 Oe, approximately (the SFD of a high remanence, square loop is basically proportional to the differential susceptibility of its demagnetization branch [8]). Figure 3.11 shows the hysteresis loop corresponding to an array with w = 200 nm, d = 500 nm and the differential susceptibility, which is basically proportional to the SFD

[8]. As can be seen, the remanence is equal to the saturation magnetization, the coercivity is one order of magnitude higher than that of the continuous films, 440 Oe for this particular array, and the width of the SFD is roughly equal to half the coercivity. These features are common to all arrays.

When measuring the magnetization component perpendicular to the axis of the wires of any of the arrays, when the magnetic field is parallel to them, no signal was observed. This means that the magnetization is parallel to the wires. Figure 3.11 shows that the magnetization component parallel to the wires is saturated while the perpendicular one is null (inset).

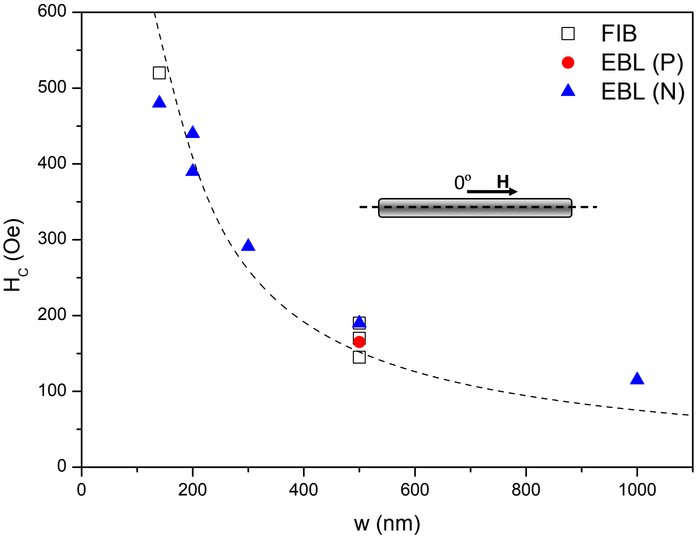

Figure 3.12: Coercivity of the nanowires depending on its width.

Figure 3.12 shows the evolution of the coercivity with the nominal width of the nanowires, following a 1/w law, in agreement with previous results [3, 4, 9–11]. It is essentially independent of the lithography technique employed and of the interwire separation d. The coercivity of three arrays with w = 500 nm, prepared by FIB with separation distances of 100, 500 and 1000 nm are 170, 145 and 190 Oe, respectively. These differences can be attributed to many factors, for example slight variations of the real thickness of the Fe films and/or of the nominal width values of the nanowires.

On the other hand, it is interesting to note that magnetostatic interactions between the nanowires do not play a fundamental role in modifying significantly the coercive force of the arrays. In fact, since the magnetization remains parallel to the axis of the wires, magnetic poles must be concentrated just at their ends which, added to the large interwire separation, leads to weak dipolar fields [2].

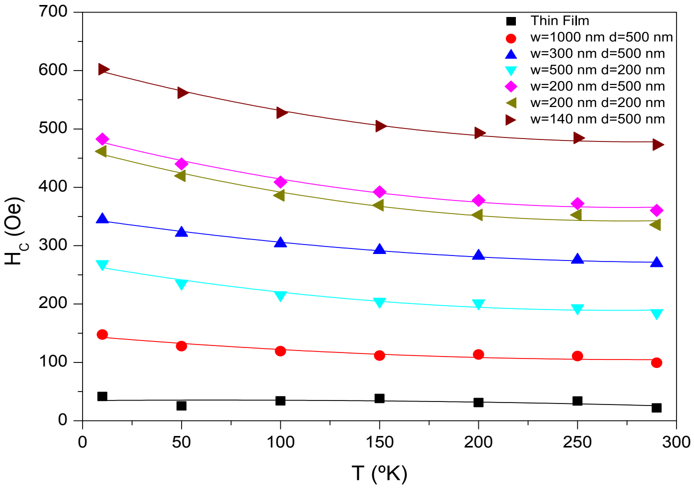

Figure 3.13: Coercivity versus temperature for different arrays of nanowires.

The coercivity of the different arrays made by EBL with negative resist versus the temperature were measured by VSM. Figure 3.13 shows that for all the arrays the coercivity decreases with the temperature. Following the typical behaviour of the ferromagnetic materials [12, 13]. As a general rule, if the system does not present any structural transformations with the temperature, the relaxation time or the time that the system needs to reach the equilibrium state decrease when the temperature increases. The separation of the system from the equilibrium (energy barrier) depends on its anisotropy, which decreases with increasing temperature, and the coercivity, considered as a measure of that separation, should also decrease with the temperature [14].

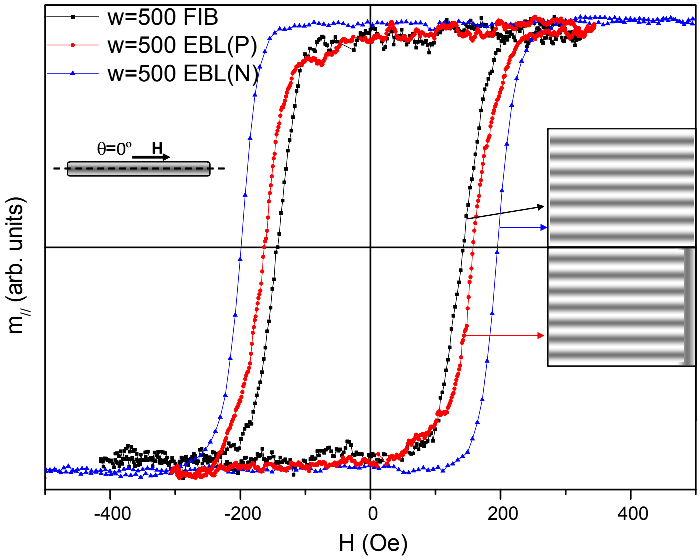

Figure 3.14: Comparison of the hysteresis loops along the wires fabricated by three different lithography techniques.

Another important issue is related to the conditions of the ends of the nanowires. Figure 3.14 shows the hysteresis loops corresponding to three arrays with w = 500 nm fabricated using the three different techniques. The FIB and EBL with negative resist fabricated arrays have their wire ends isolated from the surrounding continuous film, whereas those fabricated by EBL with positive resist are in direct contact with it. In spite of the different conditions of their wire ends, which could lead to different nucleation fields, all the arrays have essentially the same coercivity, remanence and SFD. The magnetization switching of planar nanowires basically follows a nucleation-propagation sequence: reversed nuclei generated at regions where the energy barriers preventing the reversal present a local minimum, usually the ends of the wires, expand along them through the displacement of their walls [4, 5]. If the field required for nucleation H_n is sufficiently low, the pinning field H_p, the field necessary to overcome the wall pinning at propagation hindrances, determines the coercivity. In the particular case of the EBL with positive resist fabricated array the reversed magnetization is nucleated at the continuous film at very low fields, about 20-40 Oe, before reaching the wires, whereas its coercivity is about 160 Oe, almost equal to the value of the other two arrays. This indicates that the magnetization reversal of the arrays is controlled by a pinning mechanism. This also confirmed by the angular dependence of the coercivity, which increases with increasing angle θ between the axis of the wires and the applied field, following the typical $1/cos\theta$ behaviour associated to pinning up to about $\theta = 60^o$ as displayed in the inset of figure 3.15 [15].

Generally, during the FIB patterning procedure, if the dose of Ga^+ exceeds a threshold value, local regions of low anisotropy and magnetization may be generated at the lateral surfaces of the wires due to the implantation of Ga, as explained in section 2.4.2 [16, 17]. The fact that arrays of wires of similar dimensions display the same reversal mechanism with essentially the same hysteresis parameters, irrespective of their fabrication route, suggests that the imperfections generated in the lateral surfaces of the wires during the lithography processes, after the optimization of the parameters, do not alter their magnetic behaviour, so that the defects involved in the pinning centres controlling the magnetization switching in all arrays are minimized. Therefore, the ability to fabricate well controlled magnetic nanostructures would provide not only reproducible hysteretic results but also it would allow the proposal of model systems to be studied by means of simple arguments as discussed next.

A different scenario appears for high values of the angle θ between the applied field and the axis of the wires. For $\theta > 60^o$ the efficiency of the applied field to unpin a wall trapped in a pinning centre decreases dramatically and other reversal mechanisms may become more effective. Figure 3.16 presents the magnetization processes, for the field applied

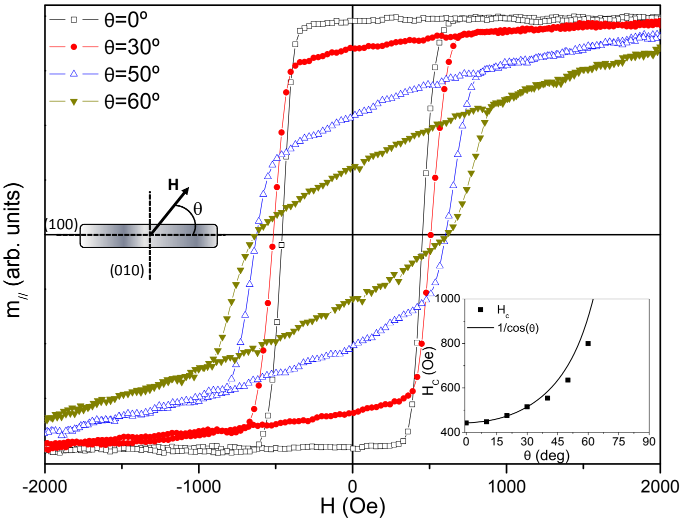

Figure 3.15: Angular dependence of the coercivity of a nanowires array with w = d = 200 nm. Inset: Angular dependence of the coercivity (the dotted line indicates 1/cosθ behaviour).

perpendicular to the axis of the wires ($\theta = 90^o$), corresponding to three arrays, with w = 500 nm and w = 200 nm fabricated by FIB and EBL. As can be seen, the magnetization increases linearly with the field until a high susceptibility jump takes it to saturation at fields about 600 Oe and 1.8 kOe for the wires 500 nm and 200 nm wide, respectively. This behaviour is accompanied by a very little hysteresis, around the high susceptibility jump. As in the case of the loops measured at low angles, the hysteresis parameters measured in wires of similar widths are almost the same no matter what fabrication technique is employed. The minor differences observed in the two arrays of 500 nm width might be due to the different thickness of the original films and/or to their real width being not exactly the nominal value as discussed previously.

The inset of figure 3.16 shows the transverse component of the magnetization, perpendicular to the applied field, corresponding to these loops. For large fields, when the magnetization is parallel to the field, its transverse component is null. As the field decreases, it abruptly switches towards the wire axis and its transverse component becomes almost saturated. It was checked that the magnetization at remanence, after saturation with $\theta = 90^o$, is almost parallel to the wires. As a consequence, these arrays rule out the process that can be observed in both polycrystalline, low anisotropy planar wires, or even in epitaxial Fe wires with a different configuration of crystalline axes, whose uniform magnetization breaks into a multidomain structure when the field decreases [4–7, 10]. This is due to the relatively high anisotropy of Fe and the well defined magnetocrystalline easy axes coincident, respectively, with the easy and hard directions originated by the shape anisotropy in the nanowire array.

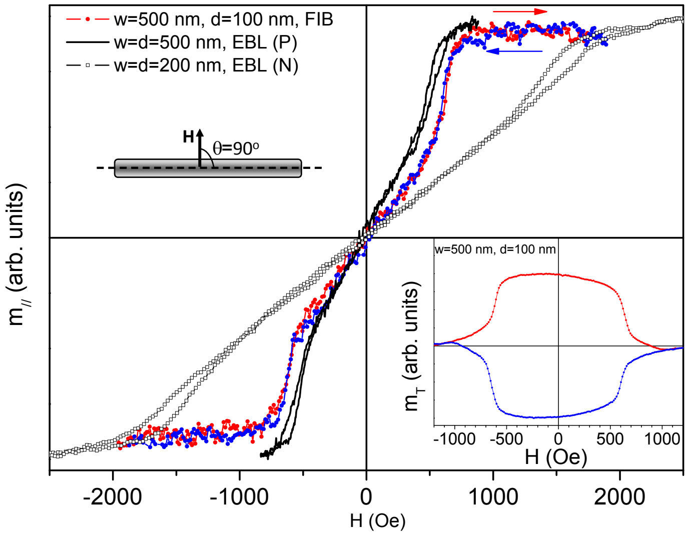

Figure 3.16: Hysteresis loops with the magnetic field applied perpendicular to the nanowires. Inset: Transverse component of the magnetization $m_\perp$ (parallel to the axis of the wires) of the FIB fabricated sample with $w = 500$ nm.

For fields slightly out of the perpendicular, typically $75^o < \theta < 90^o$, the loops present an irreversible low susceptibility region in which the magnetization branch (red) crosses above the demagnetization one (blue) and then drops back producing a characteristic hump. This occurs at about 500 Oe and 1.35 kOe for wires 500 nm and 200 nm wide, respectively, when the field is applied 7^o out of the perpendicular ($\theta = 83^o$), as shown in figure 3.17. This hump comes along with a change of sign in the transverse magnetization component (see inset in figure 3.17). After this hump the widest wires reach saturation by means of a small irreversible jump whereas the narrowest ones reach it through a reversible low susceptibility slope.

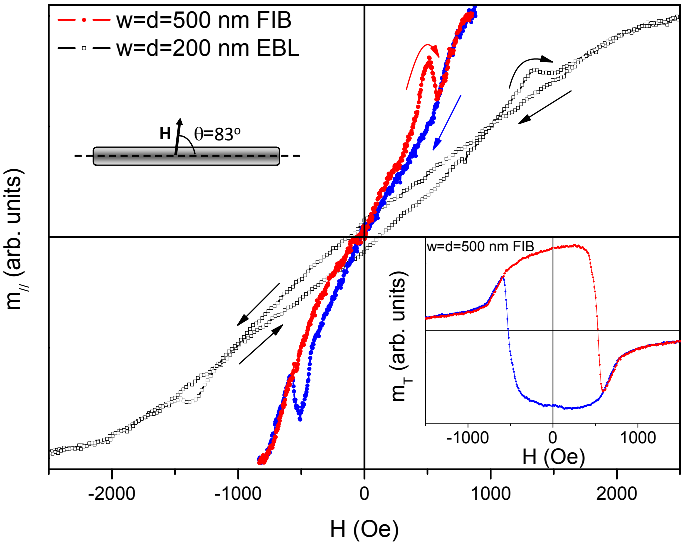

Figure 3.17: Hysteresis loops with the magnetic field applied 83^o to the nanowires axis. Inset: Transverse component of the magnetization of the FIB array with w = 500 nm.

All experimental results evidences that the magnetization processes at high angles involve almost uniform magnetization configurations, which would allow the use of single spin approach to study the trade off between the Zeeman, magnetocrystalline and magnetostatic energy contributions.

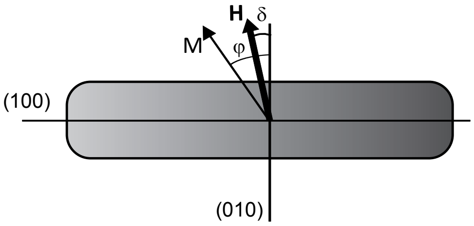

Figure 3.18: Sketch of the angles used for the hysteresis calculations.

This assumption is not fully realistic since the wires are neither perfect rectangular prisms nor ellipsoids and, consequently, non-uniform dipolar fields will be generated inside the wires which, in turn, will lead to non-strictly uniform magnetization configurations. In spite of this, a single spin approach accounts not only qualitative but quantitatively for the main features of the reversal process. Considering that in the case of planar nanowires with a large width-to-thickness ratio the magnetization is mainly confined within the plane of the sample and that, superimposed to the (biaxial) anisotropy energy associated with the (100) and (010) Fe axes, there is an energy term due to the magnetostatic energy. This term presents a minimum when the magnetization is parallel to the wire axis, and maximum when it is perpendicular. Thus, the magnetocrystalline anisotropy energy (MAE) $\mathrm{E_K}$, when restricted to the XY plane, can be written as

$$\mathrm{E_K} = K_1 \alpha_1^2 \alpha_2^2 = K_1 \mathrm{sen}^2\varphi - K_1 \mathrm{sen}^4\varphi \tag{3.1}$$

where K_1 is the first order anisotropy constant of Fe, α_1 and α_2 are, respectively, the director cosines of the magnetization with respect to the x (perpendicular to the wire) and y (parallel to the wire) axes, and φ is the angle between the magnetization and the x axis (see sketch in figure 3.18). The simplest possible expression compatible with an energy term $\mathrm{E_U}$ having axial symmetry and with a minimum when the magnetization is parallel to the wire axis y is

$$\mathrm{E_U} = -D\mathrm{sen}^2\varphi \tag{3.2}$$

where D is a positive constant to be calculated by means of the usual shape anisotropy expression,

$$D = \frac{1}{2}\left(N_{perp} - N_{par}\right) M_s^2 \tag{3.3}$$

where N_{par} and N_{perp} are the demagnetizing factors along the in-plane longitudinal and transverse directions, respectively. By adding the Zeeman energy, the total energy $\mathrm{E_T}$ expressed in reduced form $\mathrm{E_R} = \mathrm{E_T}/2K_1$ is

$$\mathrm{E_R} = A\mathrm{sen}^2\varphi - \frac{1}{2}\mathrm{sen}^4\varphi - h\mathrm{cos}^2\left(\varphi - \delta\right) \tag{3.4}$$

with

$$A = \frac{K_1 - D}{2K_1} \tag{3.5}$$

and where δ is the angle between the field and the x axis, $h = H/H_K$ is the reduced applied field, ($H_K = 2K_1/M_s$ is the anisotropy field and M_s the saturation magnetization). Table 3.2 shows the calculated values of D and A for planar wires 100 μm long, 25 nm thick and with widths varying between 140 and 1000 nm, using the M_s and K_1 values of Fe (2.15 T and 45 kJ m^{-3}, respectively) and demagnetizing factors calculated from [18]. As can be seen, the uniaxial anisotropy constant D is well above that of the Fe MAE, increasing with decreasing width from 75 to 337 kJ m^{-3}, whereas A varies from -0.33 to -3.24, approximately. By minimizing expression 3.4 the angle φ and the magnetization components, both parallel and transverse to the applied field, can be calculated.

The hysteresis loops calculated for wires with $\mathrm{w} = 500$ nm and $\mathrm{w} = 200$ nm with the field perpendicular to the wires are presented in figure 3.19. They show all the features experimentally observed in figure 3.16: a central constant susceptibility region due to a slow magnetization

w (nm)	D (kJ m^{-3})	A
140	337	-3.24
200	261	-2.40
300	194	-1.65
500	131	-0.95
1000	75	-0.33

Table 3.2: Calculated values of D and A depending of the width of the nanowire.

rotation towards the field followed by an irreversible jump up to saturation; the transverse component (inset in figure 3.16) decreases very slowly with increasing applied field, evidencing that the magnetization remains almost parallel to the axis of the wires, until it abruptly switches to zero when the magnetization becomes perpendicular to the wires. Most remarkable, the calculated fields corresponding to the irreversible jumps for the wires with w = 500 nm and w = 200 nm are in very good agreement with the experimentally measured values, as evidenced by comparing figures 3.16 and 3.19. Figure 3.20 shows the loops calculated with the field applied at $\delta = 7^o$ for the wires with w = 500 nm and w = 200 nm, which exhibit the characteristic magnetization branch crossover and hump at fields, respectively, about 700 Oe and 1.7 kOe, which are reasonably close to those experimentally measured (500 Oe and 1.35 kOe, respectively). This difference between the experimental and calculated values might be due to many factors, for example, the misalignment of the Fe crystalline axes with the axes of the wires or the real width of the wires being different from the nominal value. It is also important to note that the calculated transverse magnetization loops (insets of the figures) reproduces the experimental results, including the switching when the hump takes place.

Figure 3.21 exhibits the high field region of the loops and polar energy diagrams calculated when the field is applied at a small angle

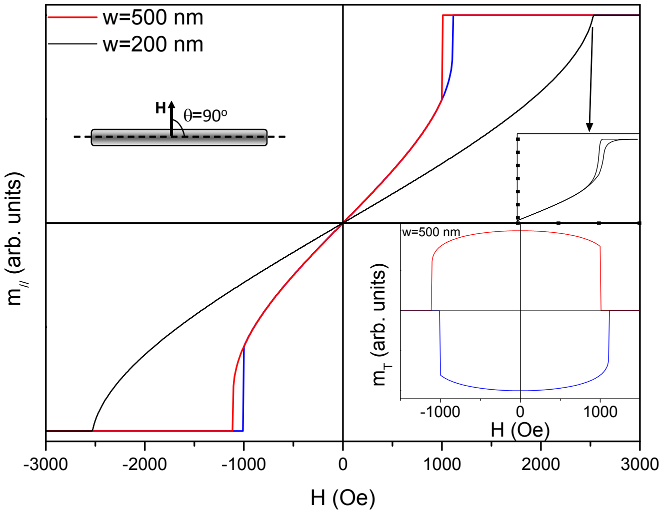

Figure 3.19: Calculated hysteresis loops with the magnetic field applied perpendicular to the nanowires. Inset: Transverse magnetization component calculated for w = 500 nm wires.

from the perpendicular wires axis ($\delta = 3^o$). For the narrowest array, w = 200 nm, there exist two minima A and B separated by an energy barrier. The A minimum disappears with increasing field and the magnetization switches from A to B. This jump produces a decrease in the parallel-to-the-field component of the magnetization and a change of sign in the transverse component, as experimentally observed (figure 3.17). After it the magnetization rotates reversible to saturation. However, for wider arrays, w = 500 nm, a third minimum C appears at higher fields and a second irreversible jump from B to C takes the magnetization near saturation, which again agrees with the experimentally observed behaviour. The return path implies the jump back to C at lower fields, although the low value of the energy barrier between B and C may again ease both B to C and return jumps thus reducing the hysteresis present in the high field region.

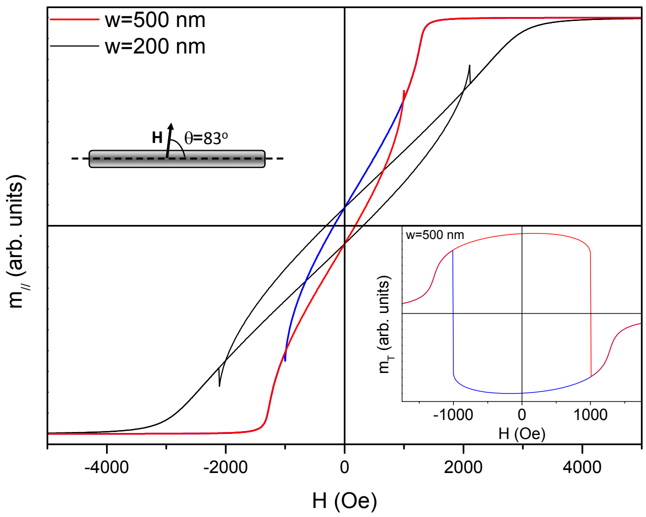

Figure 3.20: Calculated hysteresis loops with the magnetic field applied 7^o out of the perpendicular. Inset: Transverse magnetization component calculated for w = 500 nm wires.

An important issue regarding our single spin approximation is related to the biaxial and uniaxial anisotropy constant values employed. The value used for the biaxial anisotropy was the bulk Fe ($K_1 = 45$ kJ m^{-3}) and the demagnetizing factors used were the analytically calculated from [18] to obtain the uniaxial constant, which results in a good qualitative and quantitatively agreement with the experimental behaviour. Taking this into account, other eventual sources of anisotropy that can be present in the arrays seem to make up a minor contribution in the magnetization processes. This contrasts with the case of very narrow wires [19], in which the interfacial region between the Fe wires and the capping layer gives rise to a very high anisotropy energy contribution that overcomes all others; the total anisotropy and the coercivity of these wires can be tuned, to a certain extent, by using different capping layer materials. Another case in which the interfacial effects are important is that of

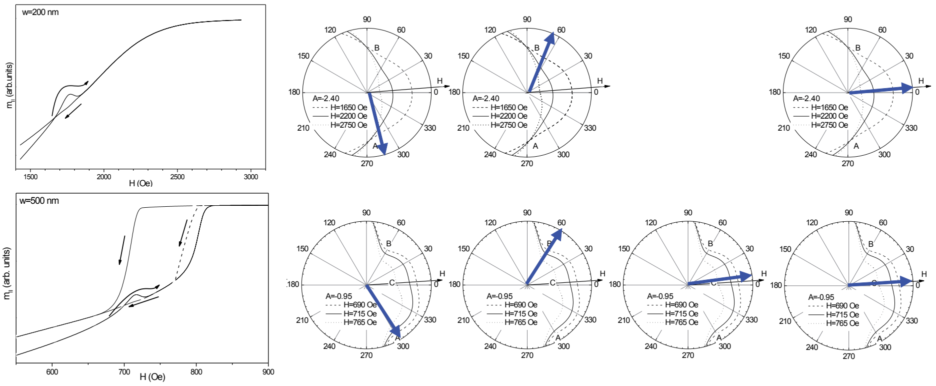

Figure 3.21: High field region of the calculated hysteresis loops for the magnetic field applied 3^o out of the perpendicular in wires with w = 200 and 500 nm and energy landscapes corresponding to uniform magnetization configurations and different values of the reduced field.

epitaxial nanowires lithographed on Fe(110)/GaAs(110) films [6], in which the combination of the stresses generated by the two-fold symmetry lattice and the mismatch at the wires-substrate interface originates an extra uniaxial anisotropy contribution that, in some cases, allows stabilize the remanent magnetization perpendicular to the wires. On the contrary, the Fe and MgO lattices at the interface of the Fe(001)[100]//MgO(001)[110] films from which our wires were fabricated posses four-fold symmetry and, a priori, any eventual anisotropy contribution due to the lattice mismatch would probably be biaxial. The fact that the calculations based just on the Fe MAE and magnetostatic energy contributions account for the magnetization processes, quantitative and qualitatively, clearly rules out any other sources of anisotropy.

3.4.2 Ferromagnetic Resonance

Section 2.3.3 describes the angular dependence of the FMR measurements for the Au/Fe/MgO films used to fabricate the arrays of nanowires. When the magnetic field is parallel to the easy magnetocrystalline directions no signal is observed because even at zero applied field the resonance frequency is above 9.8 GHz; on the contrary, four resonance peaks are observed when the field is applied along the magnetocrystalline hard directions. After the fabrication of the nanowires (by EBL with negative resist to produce isolated wires with no surrounding continuous film) additional resonance peaks appear in the 360^o angular dispersion when the magnetic field is applied near the perpendicular to the nanowires axis. Thus, the angular dispersion of the FMR exhibit resonances when the field is applied either along the Fe $\langle 110 \rangle$ and Fe (100) directions. As an example, the angular dependence for an array with w = d = 200 nm is presented in figure 3.22. Comparing it with figure 2.41, it presents the resonance peaks due to the magnetocrystalline anisotropy with 90^o fourfold periodicity, at the same field value as the thin film, whereas there is an extra signal due to the shape anisotropy of the nanowires at about 135^o and 315^o, corresponding to the field applied perpendicular to the axis of the wires, at higher field values for this particular array. The spectra around 135^o and 315^o have a clear resonance region at fields between 125 and 225 mT and another resonance almost superimposed to the paramagnetic signal of the substrate, near 400 mT. In fact, all studied arrays, for different aspect ratio, exhibit a similar structure of resonance peaks when the field is applied near the perpendicular to the wires: a single, weak peak at relatively high fields (between 350 and 550 mT, approximately, depending on the sample) and a region comprising several peaks with complex structure at much lower fields. This is shown in figures 3.27-3.32.

The analysis will start with the resonances occurring at field values above 350 mT. Table 3.3 summarizes the main features and parameters: a single peak appearing at angles around a central position with an dispersion

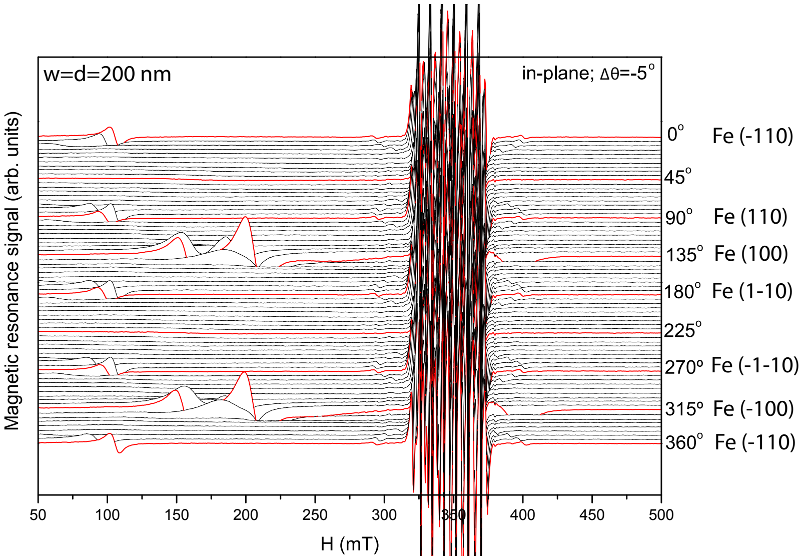

Figure 3.22: FMR spectra angular dependence for nanowires of w = d = 200 nm with in-plane applied magnetic field.

width of 7^o, approximately, for all samples -see figures 3.27(d) to 3.30(d) and 3.32(d)- and a resonance field of a few hundred mT that is weakly dependent on the wire width and that increases with increasing interwire distance (the peak corresponding to the sample with w = 500 nm, d = 200 nm overlaps with the paramagnetic signal from the substrate and it has been assigned to a nominal value of 350 mT in table 3.3). It has to be considered that upon applying fields of hundreds of mT, perpendicular to the wires, the samples are fully saturated with essentially homogeneous magnetization. Thus the resonance fields corresponding to these wires can be calculated by different models, based on the saturated mode, that take into account the anisotropy generated by the shape of the wires. These models [20] yield values that decrease sharply with increasing width, from about 400 mT for the wires with w = 140 nm to less than 100 mT for w = 1000 nm. In contrast to this, the experimental variation by the high field resonances is very weak, as shown in figure 3.23.

d (nm)	w (nm)	H_r (mT)	Angular width (^{o})
200	200	395	7
	500	350	-
500	140	536	7
	200	521	8
	300	471	8
	1000	487	7

Table 3.3: Resonance field and angular width of the resonances occurring at high fields.

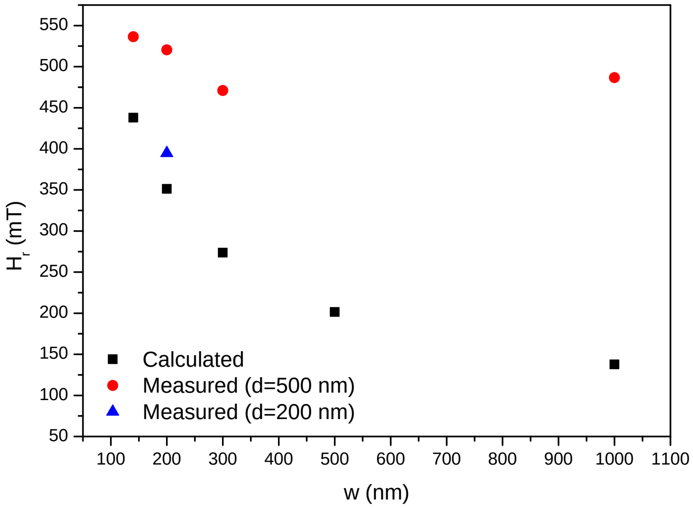

Figure 3.23: Experimental and calculated values of the resonance field (only high field resonances) as function of the width of the wires.

An important issue to understand the origin of these resonances comes from the total losses measured for each array. Figures 3.24 and 3.25 show the peaks corresponding just to the four arrays with wire separation d = 500 nm and the losses associated with them, respectively. Since the area of all arrays is the same (2×2 mm^2), the total Fe volume in an array is proportional to the percentage of its surface covered with Fe (from now on, Fe coverage), which scales as $\mathrm{w}/(\mathrm{w}+\mathrm{d})$. The Fe coverage of the arrays is shown in table 3.4 and, surprisingly, the losses of the arrays with w = 140 and 200 nm are much larger than those of the arrays with w = 300 and 1000 nm, i.e., the losses are larger in the arrays with the lowest Fe content. This result proves that these peaks are not related to a bulk dependent property.

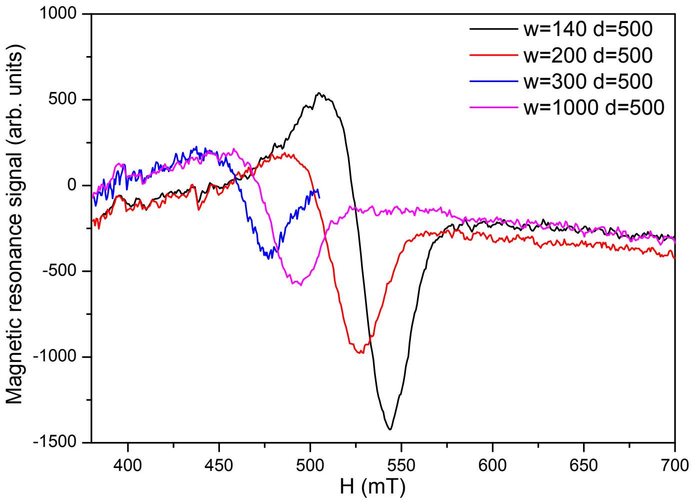

Figure 3.24: High field resonance for the arrays with wire distance d = 500 nm and field applied perpendicular to the wires.

A different point of view comes from the consideration of the density of lateral faces existing in each array, calculated as $2/(\mathrm{w}+\mathrm{d})$. All wires have two lateral faces (100 μm long × 25 nm high each), the narrower the wires

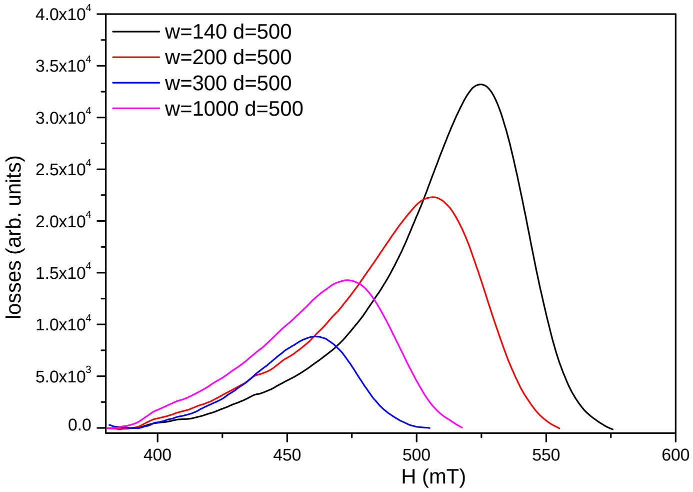

Figure 3.25: Losses corresponding to the resonances of figure 3.24.

the higher the number of lateral faces per width unit (lateral dimension) of the array. The arrays with w = 140 and 200 nm present the highest density of lateral faces and also the highest losses and peak intensities. This, in addition to the weak dependence of the resonance fields on the aspect ratio of the wires, indicates that these high field resonances are probably linked to local properties associated with the lateral surfaces of the wires.

The resonance frequency is essentially a measure of the second derivative of the free energy with respect to the angle around the local energy minimum (the curvature of the free energy or stiffness due to the restoring torque). When the magnetization is already oriented along an anisotropy energy minimum, the applied field required to reach the desired stiffness (corresponding to 9.8 GHz in this case) decreases. It might happen that even with null applied field the curvature around the minimum is above the required value and then no resonance peaks are observed. This is the case of the spectra measured along the easy directions in the continuous films (see section 2.3.3). On the contrary, when the magnetization is oriented

w (nm)	Lateral density (nm^{-1})	Fe coverage %	Total losses (arb.units)
140	$3.12 \cdot 10^{-3}$	22	$2.03 \cdot 10^{6}$
200	$2.86 \cdot 10^{-3}$	28	$1.5 \cdot 10^{6}$
300	$2.50 \cdot 10^{-3}$	37	$4.3 \cdot 10^{6}$
1000	$1.33 \cdot 10^{-3}$	67	$8.8 \cdot 10^{6}$
w (nm)	Peak position (mT)	Peak intensity (arb.units)	Peak width (mT)
140	525	$3.3 \cdot 10^{4}$	52
200	506	$2.2 \cdot 10^{4}$	59
300	461	$8.8 \cdot 10^{3}$	44
1000	473	$1..4 \cdot 10^{4}$	57

Table 3.4: Parameters of the resonance peaks shown in figures 3.24 and 3.25.

along an anisotropy energy maximum the applied field required to reach the desired stiffness increases. The high resonance field values measured from the spectra clearly show that the free energy associated with the lateral surfaces of the wires presents a sharp maximum when the magnetization is perpendicular to these surfaces. The equivalent anisotropy field associated with this maximum can be estimated from the usual resonance expressions [20, 21], yielding values about 350-450 mT, well above the anisotropy field of Fe (52 mT).

Another issue regarding these high field resonances is the decrease of the resonance field values for the two samples with interwire separation d = 200 nm (see Table 3.3). It has to be considered that upon applying fields of hundreds of mT, perpendicular to the wires, the samples are fully saturated with essentially homogeneous magnetization. This suggests that the dipolar interactions between neighbouring wires play an important role in the determination of this resonance field. This can be interpreted in a qualitatively way by means of a simple model.

When the wires are well separated and saturated along the perpendicular

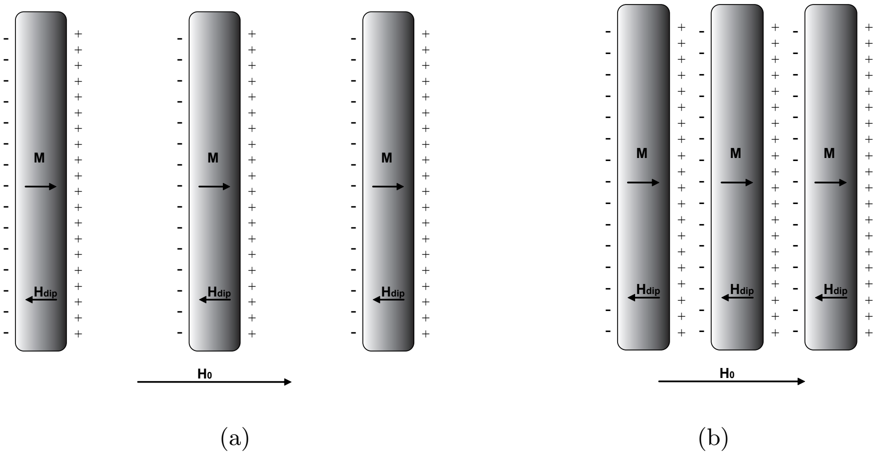

Figure 3.26: Poles distributions for (a) well separated and (b) close wires.

(figure 3.26(a)), the dipolar field H_{dip} opposing the applied field is the demagnetizing field due to the poles generated just at the edges of each wire. When the wires are close enough (figure 3.26(b)) a certain degree of pole intermixing takes place and the dipolar fields decrease. Since a given internal field is required to match the resonance frequency of 9.8 GHz, the higher the (demagnetizing) dipolar fields the higher the applied field needed. As a consequence, higher resonance fields are expected in situation (a) compared to (b).

A very different scenario appears at lower resonance fields, below 300 mT. A complex structure with multiple overlapping peaks can be observed when the field is applied around the perpendicular to the wires, as shown in figures 3.27 to 3.30 and 3.32, (a) and (c), and in figure 3.31 (a) and (b). The black dots in these figures mark the position of the resonance peaks obtained by means of a fitting procedure explained in section 2.3.3 based on linear combination of Dyson curves. As previously mentioned, the perpendicular to the wires corresponds to 135^o and 315^o in our experimental set up and the low field resonance peaks are confined in an angular region around these values whose width increases sharply with increasing wire width, as presented in figure 3.33, from about 5^o to 90^o. In the specific cases of the films with w = 500 and 1000 nm this angular region overlaps with the region around to the (110) and $(1\bar{1}0)$ axis, the magnetocrystalline hard axes, in which the resonances measured in the continuous films are visible (see figures 3.31(b) and 3.32(c)).

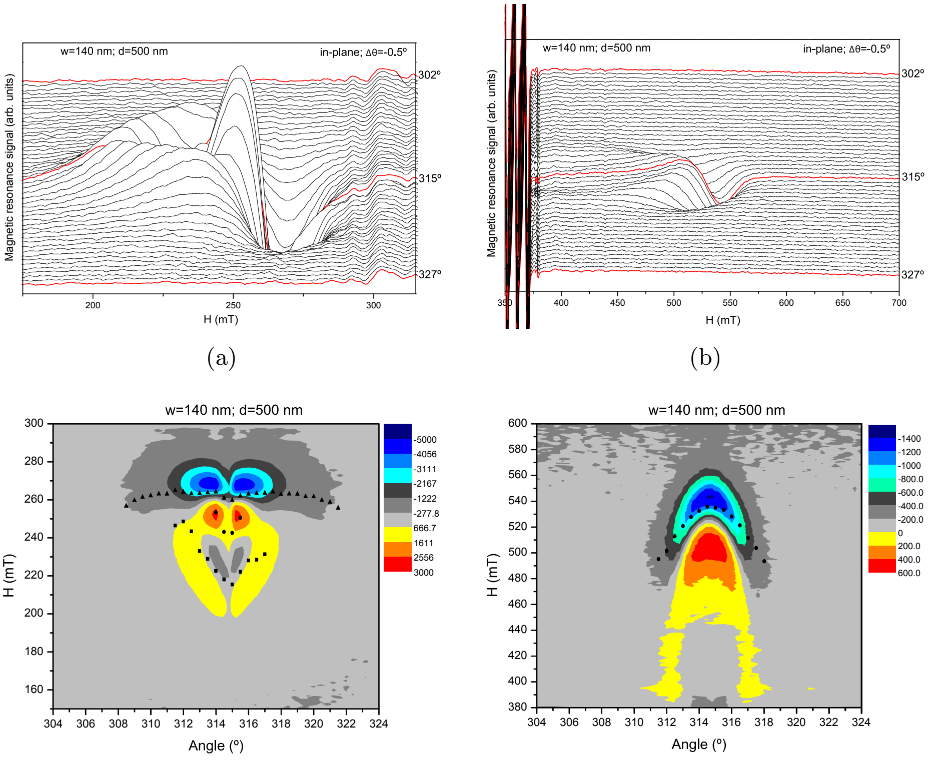

(a) (b)

(c) (d)

Figure 3.27: FMR measurements for w = 140 nm, d = 500 nm (a) low and (b) high field angular dependence, (c) and (d) the 2D plot of the intensity of (a) and (b) respectively.

Figure 3.34 shows the spectra of all arrays when the field is applied at 315^o, perpendicular to the wires. This figure confirms that the number and

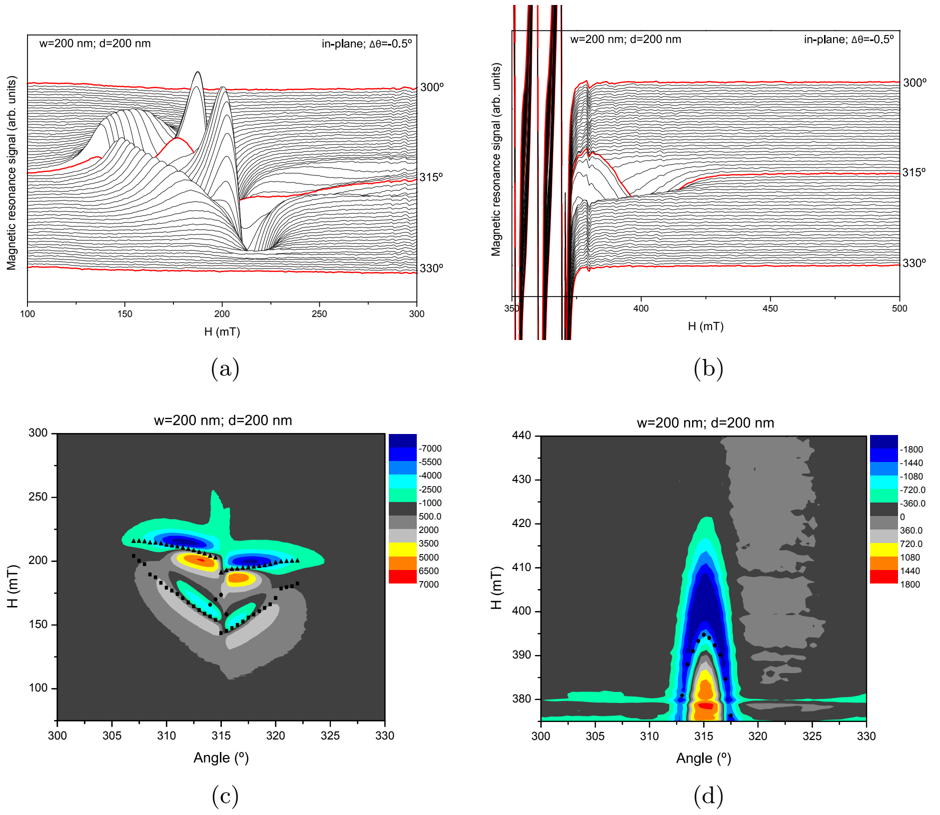

(a) (b)

(c) (d)

Figure 3.28: FMR measurements for w = 200 nm, d = 200 nm (a) low and (b) high field angular dependence, (c) and (d) the 2D plot of the intensity of (a) and (b) respectively.

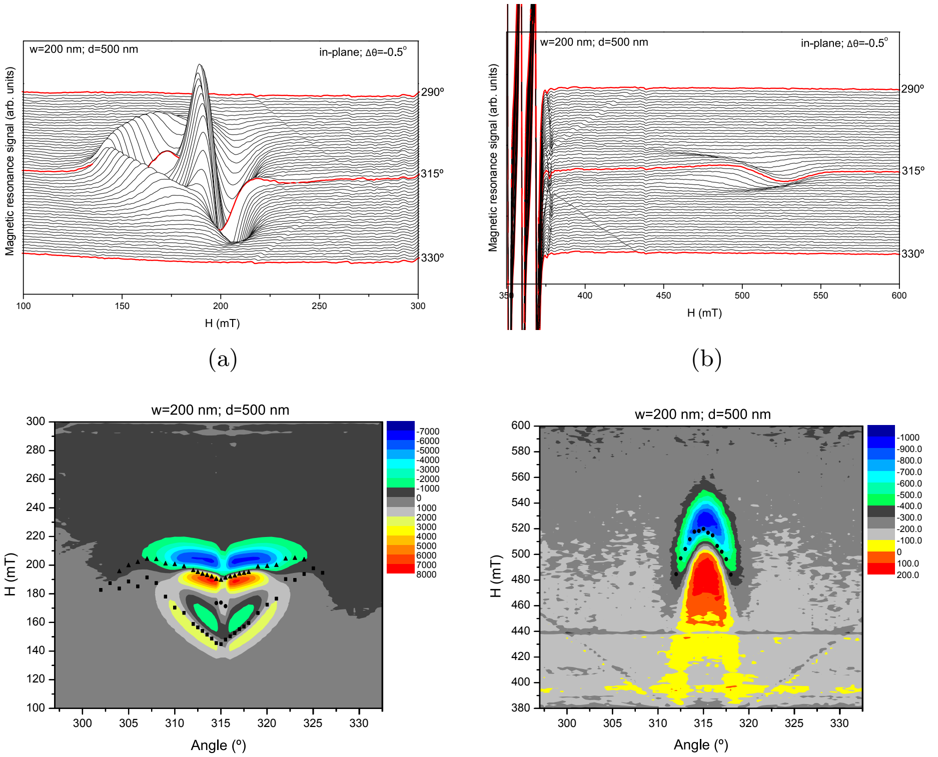

(a) (b)

(c) (d)

Figure 3.29: FMR measurements for w = 200 nm, d = 500 nm (a) low and (b) high field angular dependence, (c) and (d) the 2D plot of the intensity of (a) and (b) respectively.

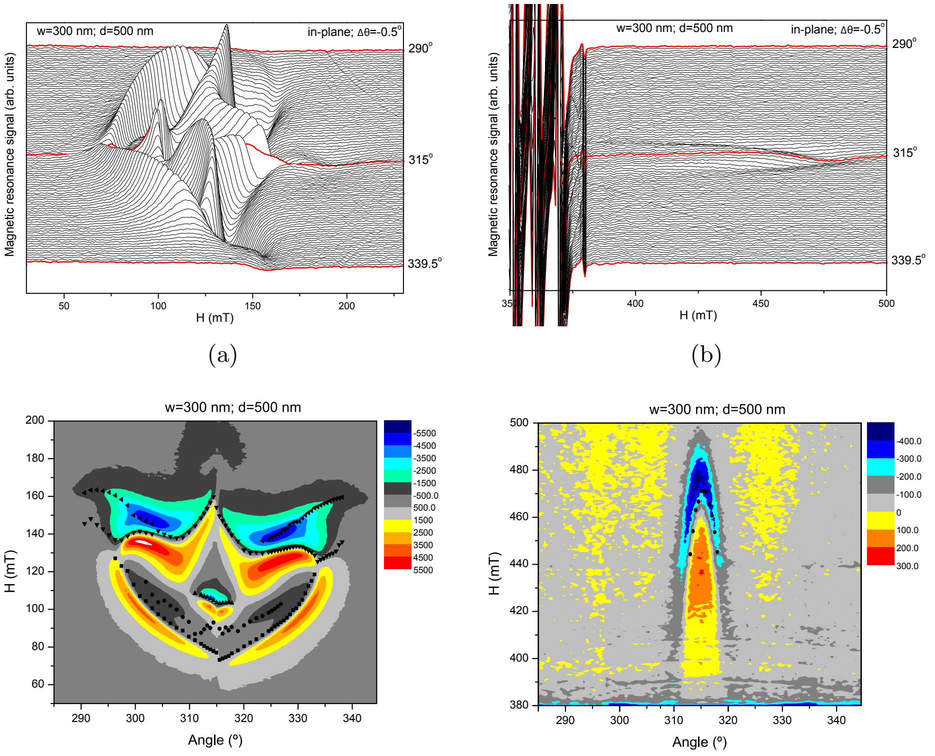

(a) (b)

(c) (d)

Figure 3.30: FMR measurements for w = 300 nm, d = 500 nm (a) low and (b) high field angular dependence, (c) and (d) the 2D plot of the intensity of (a) and (b) respectively.

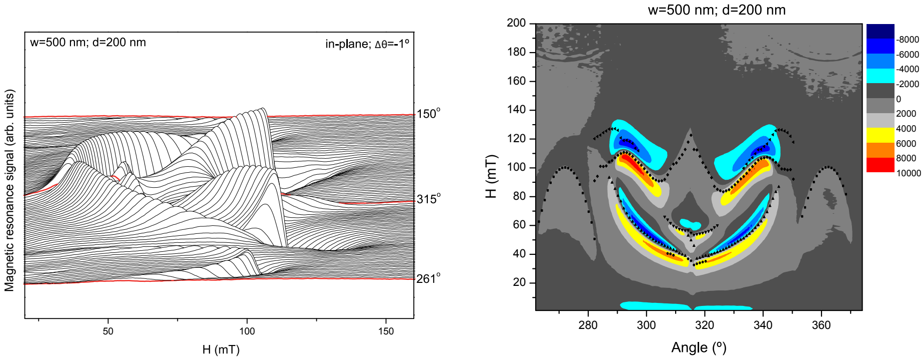

(a) (b)

Figure 3.31: FMR measurements for w = 500 nm, d = 200 nm (a) low field angular dependence, and (b) the 2D plot of the intensity of (a).

intensity of the resonances, as well as the field range in which they occur, increase with increasing wire width. The dotted line sketched over each spectrum indicates the field required to saturate the sample, which varies from about 60 mT, for the widest wires, to more than 200 mT for the wires with w = 140 nm. It is then obvious that just the resonance peaks occurring at the highest field for each spectrum (marked with an arrow in the figure) can be assigned to the *saturated mode*, in which the magnetization vector is essentially parallel to the applied field. The rest of the peaks probably correspond to *unsaturated modes*, where the magnetization vector is not parallel to the applied field.

To properly locate the resonance peaks, all FMR spectra were fitted using Dyson curves (equation 2.10), explained in section 2.3.3. The values of the resonance fields for all peaks in the spectra were obtained from these fits and, as said above, inserted as black dots in the 2D plots of figures 3.27 to 3.32.

Figure 3.35 shows the resonance field of the saturated mode for all arrays. In contrast with the high field mode, the resonance field values

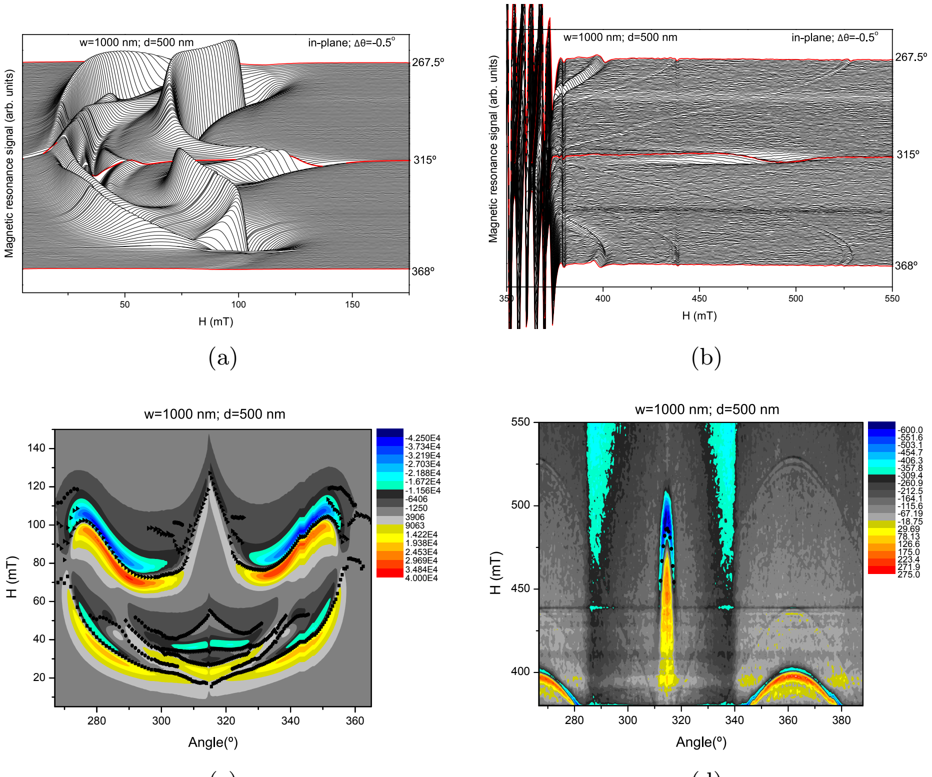

(a) (b)

(c) (d)

Figure 3.32: FMR measurements for w = 1000 nm, d = 500 nm (a) low and (b) high field angular dependence, (c) and (d) the 2D plot of the intensity of (a) and (b) respectively.

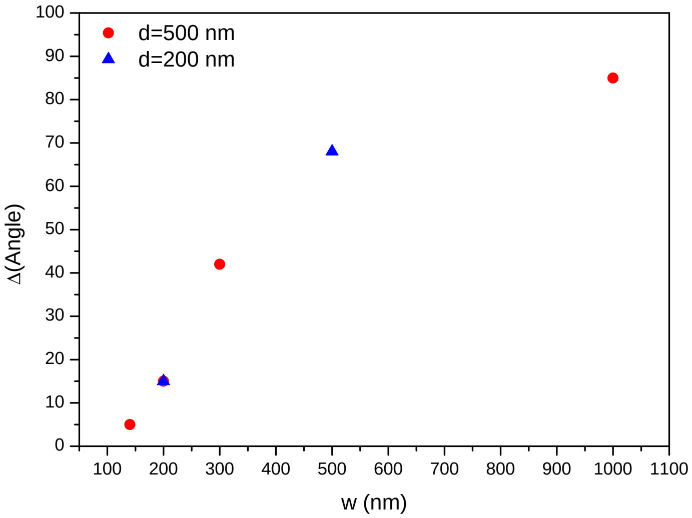

Figure 3.33: Dependence of the angular width with the nanowire width.

decrease sharply with increasing wire width. It is also important to note that the resonance field seems not to be modified by the wire separation d, which implies that the dipolar fields do not modify the energy landscape around the minima linked to the saturated mode of the arrays. The theoretical values of the resonance fields were calculated using the motion equation 2.6, where the effective field used is the sum of the applied, the dipolar and the anisotropy fields. In this calculations the demagnetization factors given by Aharoni [18] were used. Figure 3.36 shows the comparison between the calculated and measured resonance field, both exhibiting the same behaviour but the measured values always are smaller than the calculated ones. This means that the effective anisotropy is smaller than the theoretical value, which might be due to the lattice distortion originated by the lithography, as discussed in section 3.3. This distortion is more significant for the narrowest wires, in which, indeed, the largest difference is obtained.

The angular width of the low field resonance region increases with the

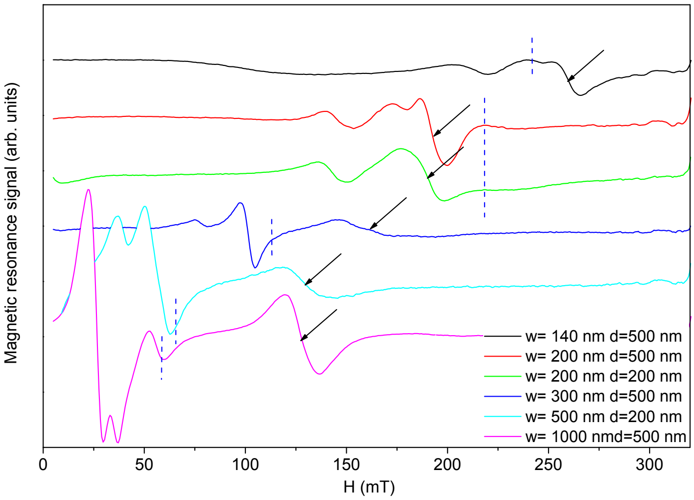

Figure 3.34: Spectra corresponding to the low field region for all arrays and field applied perpendicular to the wires. The arrows mark the saturated mode resonance for each sample.

wire width (figure 3.33), as previously mentioned. It can be seen that for the nanowires of w = 1000 nm the resonance region centered at the energy maximum of the shape anisotropy has an angular width over 90^o, superimposed to that of the magnetocrystalline anisotropy. The number of modes at low fields also increases with the width of the wires: when the magnetic field is perpendicular to the wires the arrays with w = 140 nm and w = 200 nm have three resonances, those with w = 300 nm present four, whereas those with w = 500 nm and w = 1000 nm present five.

All the resonances occurring at fields below the saturation mode are due to unsaturated modes, i.e. oscillations when the magnetization vector is not parallel to the applied field. The analysis of the magnetization processes for fields applied near the perpendicular to the wires (section 3.4.1) have revealed the existence of several energy minima associated with the irreversible jumps at fields slightly below the saturation value, such as those shown in figure 3.21. It is quite likely that the peaks measured

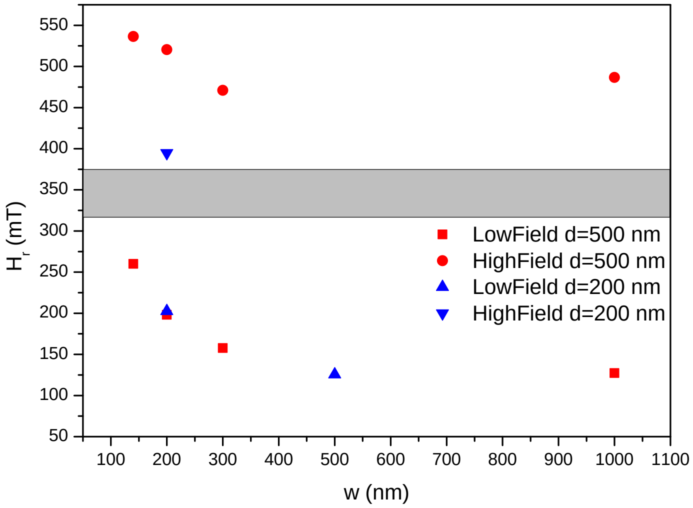

Figure 3.35: Dependence of the resonance field with the nanowire width.

with the applied field close to the perpendicular to the wires and at values slightly below that of saturation correspond to magnetization oscillations around these minima. In addition to this, when the applied field is more than roughly 20^o-25^o away from the perpendicular, the reversal mechanisms are based on both homogeneous rotations and wall pinning. The coercive force of the pinning sites, which is correlated with the depth of their energy minima, increases sharply with decreasing wire width (figure 3.12) and also as the applied field approaches the perpendicular to the wires (figure 3.15). Domain walls in the array with w = 1000 nm are present in the range from 11 mT to 35 mT, approximately, when the applied field moves from parallel to the wires to about 20^o out of the perpendicular. The equivalent range for the w = 500 nm arrays goes from about 15 mT to 60 mT. The large number of low field components of the wires with w = 500 and 1000 nm are probably linked to domain wall resonances. The high coercivity of the narrowest wires, especially for applied fields at large angles with respect to their axis, are indicative of the deep energy minima linked to their pinning

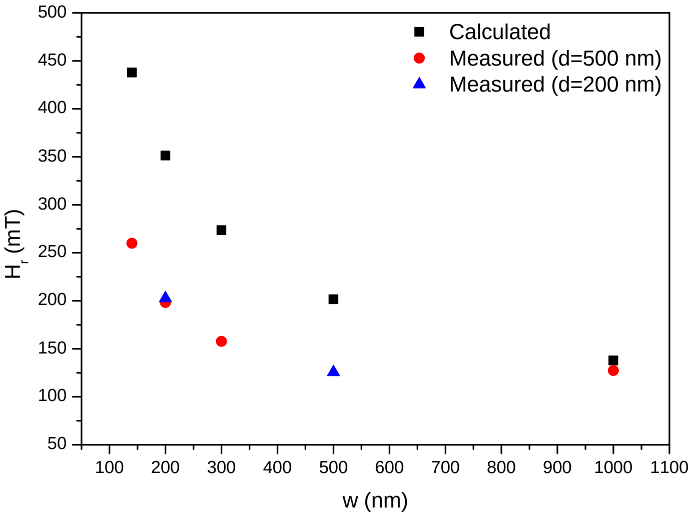

Figure 3.36: Comparison of the calculated and measured resonance fields.

sites. The lack of eventual resonances linked to them can be tentatively attributed to the fact that, as in the case of the resonances along the easy axes, the corresponding frequency is above that of the experimental set up (9.8 GHz) even at null applied field.

Some other FMR works had been done with magnetic nanowires. Two examples are references [6, 22], but they do not have the same contribution due to the uniaxial anisotropy of the wires. Guslienko *et al.* used permalloy wires, and the calculations [23] were made neglecting all the anisotropies of the thin film. In the case of this thesis, it is not possible because of the large biaxial magnetocrystalline anisotropy of the Fe, contrary to that of permalloy, small and isotropic. They have spin wave excitation when the field is applied perpendicular to the wires out of plane, with very high resonance fields, of about 1140 mT.

The FMR system used in this thesis can applied a maximum field of 1500 mT. Arrays were measured in out-of-plane geometry, and no signal was obtained. Perhaps the magnetic field applied was not large enough to excite the spin waves in the singlecrystalline Au/Fe/MgO (001). Figure 3.37 represents the FMR angular dependence of the wires (w = 140 nm, d = 500 nm) measured with the film rotated 90^o which respect to the in-plane measurements. 0^o represents the spectra with the magnetic field applied perpendicular to the film (out-of-plane). 90^o and 270^o represent the spectrum with the magnetic filed in-plane perpendicular to the wires, which are equivalent to the in-plane previous ones when the field is perpendicular to the wires. The only difference is that in this case the microwave is perpendicular to the film and the substrate, so that the paramagnetic MgO signal is smaller in relation to the ferromagnetic one.

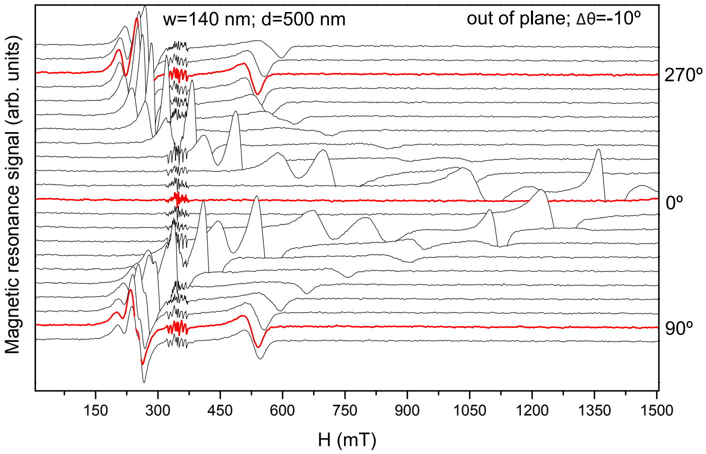

Figure 3.37: Angular dependence of FMR measurements out of plane for w = 140 nm, d = 500 nm.

The second example was done by Hassel *et al.* with wires made of singlecrystalline iron, but with the long axis of the wires parallel to the hard axis of the film. They observed an extra resonance peak in the continuous film which is only present at the rim of the film, but not when the field is perpendicular to the wires as the case presented here.

3.4.3 Scanning Transmission X-ray Microscopy

Scanning Transmission X-ray Microscopy (STXM) experiments were performed to visualize in-situ the reversal mechanism of nanowires with spatial resolution in the nanometer range. STXM measurements were carried in collaboration with Prof. Tolek Tyliszczak at beamline 11.0.2 in the Advanced Light Source (ALS) of the Lawrence Berkeley National Laboratory (LBNL) [24, 25]. This beamline consists of a scanning microscope with a focusing system based on Fresnel zone plates, with a resolution about 30-40 nm, determined by spot size of the beam. A photon-counting detector behind the sample records the intensity of the transmitted radiation, generating an image pixel by pixel during the scan. The magnetic signal is obtained by switching the circular polarization of the incoming light from right to left and subtracting the corresponding images. X-ray magnetic circular dichroism is a well established technique which provides magnetic contrast with element sensitivity. Absorption change appears when the photon energy is scanned through the absorption edge of the inner core levels of the element whose magnetization is analysed. In the particular case of the samples studied the energy was tuned to the Fe $2p_{3/2}$ and $2p_{1/2}$ levels which correspond to L_3 and L_2 absorption edges.

The STXM is an instrument working in transmission mode, so that a new set of samples was fabricated on very thin membranes, transparent to the X-ray beam. Au/Fe films were grown onto silicon nitride membranes from Silson Ltd, 200 nm thick, and with a lateral size of 2 mm. These films were grown with the same conditions as the Au/Fe/MgO (001) films described in section 2.1. The main difference with respect to the Fe deposited onto MgO is that, on these Si_3N membranes, the Fe do grows with nanocrystalline structure. After the thin film growth the samples were lithographed with FIB with an intensity of 300 pA. Thus, the wires fabricated have no competition between the shape anisotropy of the wires and that due to the overall magnetocrystalline anisotropy. However, they can be used to visualize the domain propagation along the wires when the field is applied parallel to them.

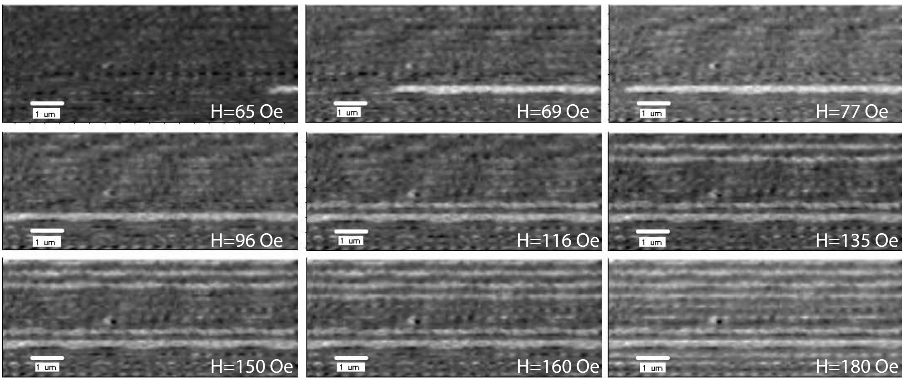

Figure 3.38: Sequence of STXM images of the nanowires with w = 300 nm, d = 100 nm varying the magnetic field from -300 Oe to 300 Oe applied parallel to them.

Figure 3.38 represents a set images of the nanowires array with w = 300 nm, d = 100 nm, measured at a photon energy of 707.9 eV, (Fe L_3 edge). These images were taken by sweeping the magnetic field along the wires from -300 Oe to 300 Oe. To enhance the contrast of the magnetization changes each image is divided by the previous one, so that they display local events of magnetization changes between consecutive images. All the previous images with some changes are added, which therefore, contain the total magnetization reversal processes taking place in the nanowires. It can be clearly seen in the first image ($H = 65$ Oe)the start of the reversal process occurring in single wire. Consecutive stages of domain wall propagation in this wire are visualized for fields $H = 69$, 77 and 96 Oe. This propagation stops at some imperfections of the wires edges acting as pinning centers, probably produced during the lithography process.

From $H = 116$ Oe there exists the simultaneous switching of several nanowires, some of which reverse completely in a single event and others propagate in steps due to the presence of pinning centers. This result evidences the existence of the switching field shown in figure 3.11 with respect to the very narrow disribution of the continuous film.

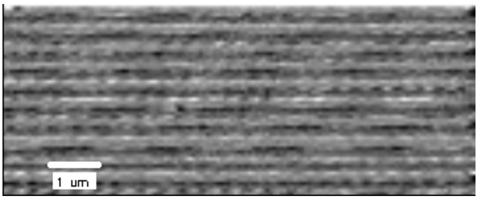

Figure 3.39: STXM image of the nanowires with w = 300 nm, d = 100 nm saturated (H = 300 Oe).

Figure 3.39 displays the STXM images of nanowires with w = 300 nm, d = 100 nm under magnetic field saturation (H = 300 Oe). In this case, all the wires present uniform contrast a a consequence of the complete alignment of magnetization along their main axis. Under this saturation conditions STXM provides complementary information not only on the magnetization but also on the morphology of the nanowires. This combination allows to correlate morphological features with reversal mechanisms at nanometer scale.

Bibliography

[1] M. Kläui, C. A. F. Vaz, J. A. C. Bland, L. J. Heyderman, F. Nolting, A. Pavlovska, E. Bauer, S. Cherifi, S. Heun and A. Locatelli, *"Head-to-head domain-wall phase diagram in mesoscopic ring magnets"* Applied Physics Letters **85** (23) 5637–5639 (2004).

[2] G. Gubbiotti, S. Tacchi, G. Carlotti, P. Vavassori, N. Singh, S. Goolaup, A. O. Adeyeye, A. Stashkevich and M. Kostylev, *"Magnetostatic interaction in arrays of nanometric permalloy wires: A magneto-optic Kerr effect and a Brillouin light scattering study"* Physical Review B **72** (22) 224413 (2005).

[3] P. Vavassori, V. Bonanni, G. Gubbiotti, A. Adeyeye, S. Goolaup and N. Singh, *"Cross-over from coherent rotation to inhomogeneous reversal mode in interacting ferromagnetic nanowires"* Journal of Magnetism and Magnetic Materials **316** (2) e31–e34 (2007).

[4] M. Brands, R. Wieser, C. Hassel, D. Hinzke and G. Dumpich, *"Reversal processes and domain wall pinning in polycrystalline Co-nanowires"* Physical Review B **74** (17) 174411 (2006).

[5] U. Ebels, A. O. Adeyeye, M. Gester, R. P. Cowburn, C. Daboo and J. A. C. Bland, *"Anisotropic domain evolution in epitaxial Fe/GaAs(001) wires"* Physical Review B **56** (9) 5443–5451 (1997).

[6] C. Hassel, F. M. Römer, R. Meckenstock, G. Dumpich and J. Lindner, *"Magnetization reversal in epitaxial Fe nanowires on GaAs(110)"* Physical Review B **77** (22) 224439 (2008).

[7] B. Hausmanns, T. P. Krome and G. Dumpich, *"Magnetoresistance and magnetization reversal process of Co nanowires covered with Pt"* Journal of Applied Physics **93** (10) 8095–8097 (2003).

[8] M. Alonso-Sañudo, J. J. Blackwell, K. O'Grady, J. M. González, F. Cebollada and M. P. Morales, *"Magnetic behaviour and percolation in mechanically alloyed Fe-SiO_2 granular solids"* Journal of Magnetism and Magnetic Materials **221** (1-2) 207–214 (2000).

[9] A. Fert and L. Piraux, *"Magnetic nanowires"* Journal of Magnetism and Magnetic Materials **200** (1-3) 338–358 (1999).

[10] B. Hausmanns, T. P. Krome, G. Dumpich, E. F. Wassermann, D. Hinzke, U. Nowak and K. D. Usadel, *"Magnetization reversal process in thin Co nanowires"* Journal of Magnetism and Magnetic Materials **240** (1-3) 297–300 (2002).

[11] M. Brands, B. Leven and G. Dumpich, *"Influence of thickness and cap layer on the switching behavior of single Co nanowires"* Journal of Applied Physics **97** (11) 114311 (2005).

[12] O. Benda and V. Ac, *"New approach to experimental investigation of coercivity temperature dependence"* IEEE Transactions on Magnetics **3** (3) 518 – 521 (1967).

[13] X.-J. Xu, Q.-L. Ye and G.-X. Ye, *"Temperature dependence of coercivity behavior in iron films on silicone oil surfaces"* Physics Letters A **361** (4-5) 429–433 (2007).

[14] A. Hernando and J. M. Rojo, *Física de los materiales magnéticos.* Editorial Síntesis, S.A. (2001).

[15] D. Givord, M. Rossignol and V. M. T. S. Barthem, *"The physics of coercivity"* Journal of Magnetism and Magnetic Materials **258-259** 1–5 (2003).

[16] C.-M. Park and J. A. Bain, *"Local degradation of magnetic properties in magnetic thin films irradiated by Ga^+ focused-ion-beams"* IEEE Transactions on Magnetics **38** (5, Part 1) 2237–2239 (2002).

[17] J. P. Jamet, J. Ferre, P. Meyer, J. Gierak, C. Vieu, F. Rousseaux, C. Chappert and V. Mathet, *"Giant enhancement of the domain wall velocity in irradiated ultrathin magnetic nanowires"* IEEE Transactions on Magnetics **37** (4, Part 1) 2120–2122 (2001).

[18] A. Aharoni, *"Demagnetizing factors for rectangular ferromagnetic prisms"* Journal of Applied Physics **83** (6) 3432–3434 (1998).

[19] B. Borca, O. Fruchart, E. Kritsikis, F. Cheynis, A. Rousseau, P. David, C. Meyer and J. C. Toussaint, *"Tunable magnetic properties of arrays of Fe(110) nanowires grown on kinetically grooved W(110) self-organized templates"* Journal of Magnetism And Magnetic Materials **322** (2) 257–264 (2010).

[20] C. Kittel, *"On the theory of ferromagnetic resonance absorption"* Physical Review **73** (2) 155–161 (1948).

[21] Kh. Zakeri, Th. Kebe, J. Lindner and M. Farle, *"Magnetic anisotropy of Fe/GaAs(001) ultrathin films investigated by in situ ferromagnetic resonance"* Journal of Magnetism and Magnetic Materials **299** (1) L1–L10 (2006).

[22] K. Y. Guslienko, V. Pishko, V. Novosad, K. Buchanan and S. D. Bader, *"Quantized spin excitation modes in patterned ferromagnetic stripe arrays"* Journal of Applied Physics **97** 10A709 (2005).

[23] K. Y. Guslienko, S. O. Demokritov, B. Hillebrands and A. N. Slavin, *"Effective dipolar boundary conditions for dynamic magnetization in thin magnetic stripes"* Physical Review B **66** (13) 132402 (2002).

[24] A. L. D. Kilcoyne, T. Tyliszczak, W. F. Steele, S. Fakra, P. Hitchcock, K. Franck, E. Anderson, B. Harteneck, E. G. Rightor, G. E. Mitchell, A. P. Hitchcock, L. Yang, T. Warwick and H. Ade, *"Interferometer controlled scanning transmission X-ray microscopes at the Advanced Light Source"* Journal of Synchrotron Radiation **10** 125 (2003).

[25] T. Warwick, H. Ade, S. Fakra, M. Gilles, A. Hitchcock, D. Kilcoyne, D. Shuh and T. Tyliszczak, *"Further development of soft X-ray scanning microscopy with an elliptical undulator at the Advanced Light Source"* Synchrotron Radiation News **16** 22 (2003).

4

Antidots

4.1 Introduction

The aim of the present chapter is to obtain information about the relationships between the extrinsic properties of the antidots and the nature and characteristics of their magnetization reversal processes. An antidot is a non-magnetic region, a hole, defined in an otherwise continuous magnetic film. Highly regular antidot arrays with antidot sizes and separations ranging from a few tens of nanometers up to the microns range are candidate materials to implement magnetic sensors [1]. Different lithographies, including those using X-rays, ions and electrons [2–4] as well as anodic aluminium oxide membranes [5], have been used to produce arrays of nanomotifs whose parameters were chosen aiming at different hysteretic behaviours. The basic idea underlying the implementation of antidot arrays is that related to the occurrence of spatial discontinuities of the magnetization at the surfaces limiting the antidots. Those discontinuities have associated magnetic poles originating an "internal shape" effective magnetic anisotropy that can overcome by up to two orders of magnitude that measurable in transition metal, continuous films of the same composition. Importantly, the "internal shape" effective anisotropy can be conveniently varied trough the modifications of the parameters defining the geometry of the array which opens a way to vary its hysteretic mechanisms and parameters. Previous results in this sense are the large coercivity enhancement originated by the patterning into antidot arrays [1, 4, 6, 7] and the observation of different effective magnetic anisotropy symmetries for different symmetry arrays: square [7, 8] and hexagonal [8, 9] arrays are linked to two-fold and three-fold effective anisotropies.

One of the main problems raised by the patterned films is that related to the understanding of their demagnetization processes and, especially, the relationship between those processes and the array geometry and dimensions. Due to the dipolar energy minimizing structures at the antidot surfaces, the films can exhibit significant spatial inhomogeneities in the magnetic moment distribution which can largely influence the global behaviour of the system and make difficult the description in simple terms of the magnetization reversal.

Two extreme regimes can be distinguished regarding the relationship between the spatial density of antidots and the array magnetic behaviour:

1. Diluted: the antidots are far enough to be considered isolated and do not appreciably alter the magnetic anisotropy [10]. In this case the antidots act as pinning centrers for the domain walls propagating through the array.

2. Highly concentrated: the antidots are close enough that the magnetization structures that are created by the antidot surface occupy the antidot region and create a highly inhomogeneous domain structure [5, 6, 11–14]. In this regime the magnetic anisotropy is dominated by the induced anisotropy resulting from the spatial preference of the created structure.

The length of the magnetic structures created around the antidots is determined by the exchange length in the considered material. Therefore, in de diluted regime the separation between antidots is several times lager than this length.

4.2 Fabrication

The antidots have been lithographed onto the singlecrystalline Fe thin films by means of FIB and EBL with positive resist, as described in section 3.2. The FIB lithography was performed with an intensity of 100 pA, and each array was surrounded by a frame lithographed with an intensity of 3000 pA. For the EBL PMMA was deposited and irradiated using a voltage of 20 kV and an intensity of 0.034 nA, with a dose of 200 μC cm^{-2}. In these thin films the IBE was performed under the same conditions of the nanowires for 105 s.

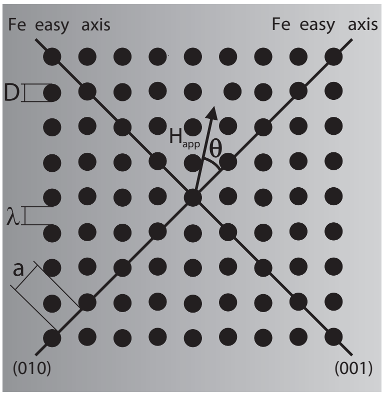

Figure 4.1: Scheme of the antidots array.

With these two techniques antidots arrays with different characteristic parameters were lithographed. Figure 4.1 represents an sketch of an antidot array showing the main parameters, the antidots diameter, D, and separation between their edges, λ, as well as the orientation of the crystalline axes. The parameter parameter a, represented in this figure, is the separation between the edges of the antidots along the diagonal of the array and is given by the equation $a = (D + \lambda)\sqrt{2} - D$.

D (nm) \λ **(nm)**	**200**	**300**	**400**	**500**	**750**	**1000**	**2000**
200	EBL						
300		EBL					
400	EBL	EBL	EBL				
500				FIB2			
750					EBL		
1000						FIB1 EBL	FIB2

Table 4.1: Dimensions of the antidots and lithography technique used.

Just three Fe thin films were used to fabricate all the arrays, table 4.1

shows the dimensions of the arrays and the thin film in which they were lithographed. All the EBL antidots were fabricated on the same thin film whereas the FIB arrays were made in two different thin films, named FIB1 and FIB2 in the table.

4.3 Structural characterization

The structure of the antidots was characterized by microscopy techniques: SEM and AFM. Other techniques such as the reciprocal space maps can not be performed in these arrays because they are surrounded by the continuous thin film, whose signal is larger than the one from the array. Only local techniques can be used with the antidots.

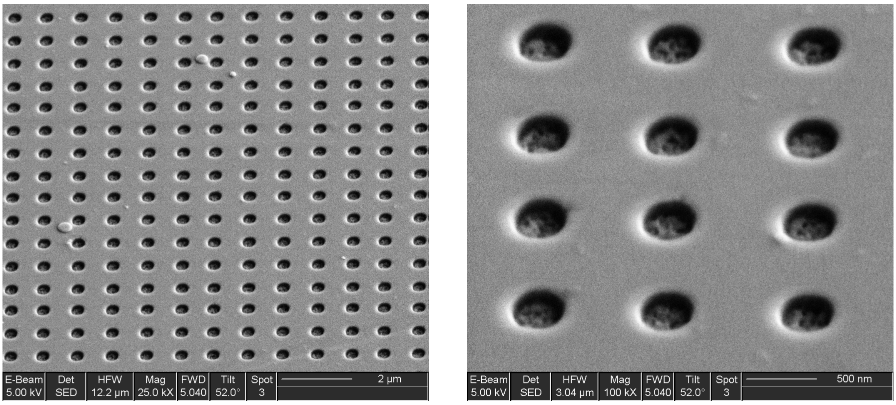

(a) (b)

Figure 4.2: SEM pictures of a (a) large area and (b) detail of an antidot array with $D = 500$ nm, $\lambda = 500$ nm.

The microscopy pictures are shown in figures 4.2 and 4.3. The SEM pictures show the good control of the shape and dimensions of the arrays. The AFM images are useful to measure the rms roughness of the area between antidots and to check if it is damaged by the lithography. After the lithography the rms roughness increases, compared to the thin film roughness (see Fig. 2.23), from 0.2 to 0.4 nm. Although the lithography damages slightly the surface, it can be still considered a very flat surface.

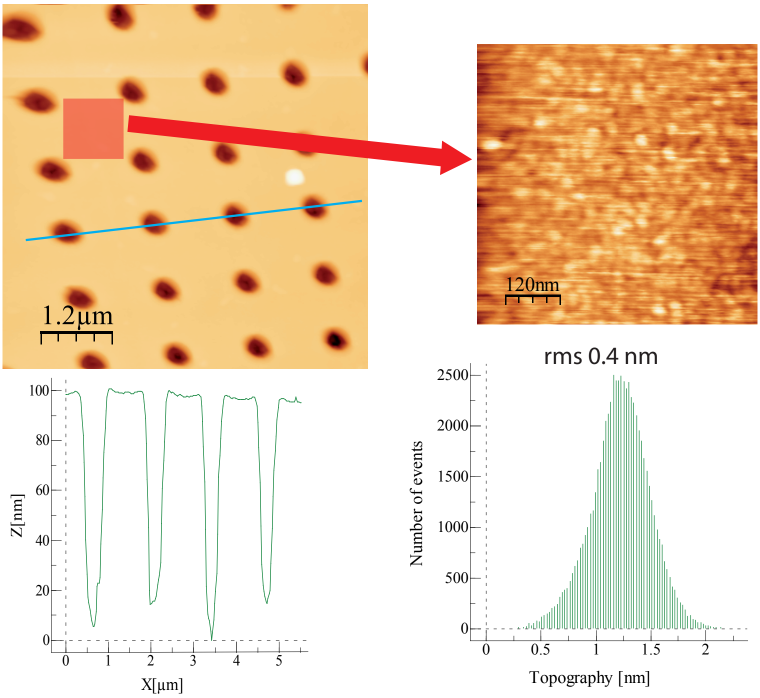

Figure 4.3: AFM image of the antidots array with $D = \lambda = 500$ nm, with a profile of a row of antidots and a zoom of the area without antidots. The rms roughness calculation in that area is also shown.

4.4 Magnetic characterization

4.4.1 Hysteresis behaviour

The purpose of this work is to continue the study of the antidots already started [1, 4, 6] in singlecrystalline Fe films with the Fe (001) axes parallel to the diagonal of the array lattice. The choice of the easy axes orientation is meant to enhance the magnetocrystalline anisotropy through effective anisotropy axes parallel to the magnetocrystalline ones, as shown in figure 4.1. Just one array, with $D = \lambda = 1000$ nm, was lithographed rotated 45^o, with the Fe easy axes along the rows and columns, instead of the diagonal, in the thin film called FIB1 in table 4.1.

The separations of the antidots that are going to be studied in this chapter are not large enough to be in the diluted regime but still allow the propagating domain walls to be fully accommodated into the inter-antidot region, so they are neither in the highly concentrated regime. The antidots arrays are in the so-called intermediate concentrated regime.

The hysteresis of these arrays has been characterized by means of Kerr Effect in the longitudinal configuration. All the arrays are surrounded by Fe thin film, so the hysteresis loops measured by Kerr have contribution of the thin film added to the antidots one.

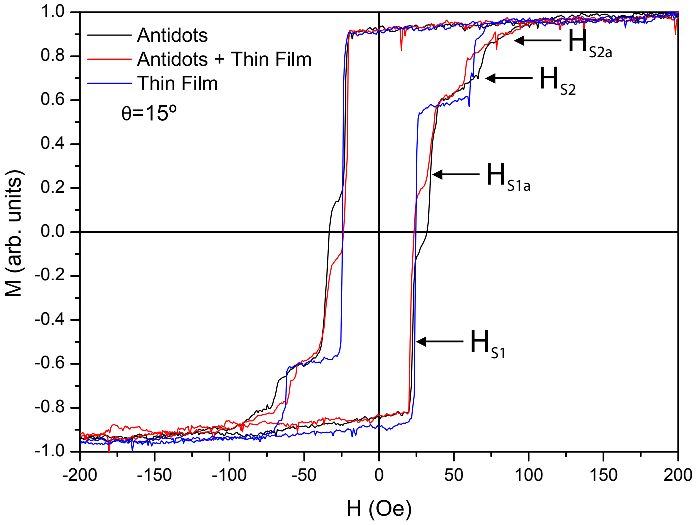

Figure 4.4: Hysteresis loops of the antidots $D = 1000$ nm, $\lambda = 2000$ nm lithographed with FIB with the field applied 15^o with the hard axes.

This work has been focused in the differences of the hysteresis parameters along the easy and the hard axes of array, because the angular dependence had been measured and simulated previously [15]. Only one measurement was done out of these two axes to test if it is consistent with the previous results. This measurement was done for the array with $D = 1000$ nm, $\lambda = 2000$ nm, 15^o out of the hard axes. Figure 4.4 shows the comparison between the thin film and the antidots hysteresis loops. The black loop represents the hysteresis loop with the laser spot centred inside the antidots array, although part of it reaches the continuous film, so the hysteresis loop has a contribution from the thin film; the red one represents the loop with the spot centred between the antidots and thin film; finally, the blue one is the thin film loop. From these three loops it is clear that there is an extra switching field due to the antidots, H_{s1_a}, higher than the thin film one, H_{s1}, represented in the angular dependence of the thin film (section 2.3.1). The antidots also increase the second switching field, H_{s2}, of the thin film to H_{s2_a}.

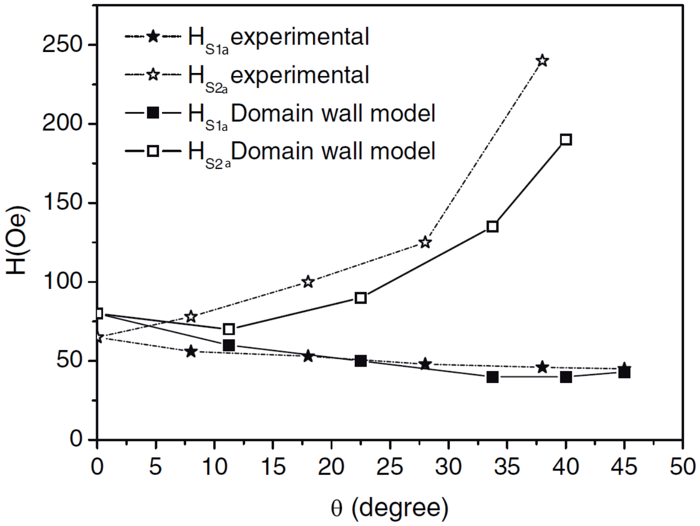

Figure 4.5: Calculated and experimental angular dependence of the switching fields of the antidot arrays with $D = \lambda = 440$ nm [15].

This result is consistent with the simulation model associated to a nucleation of the demagnetisation process occurring outside the array, represented in figure 4.5. According to this model, a first (H_{s1_a}) irreversible process takes place when the externally nucleated domain wall reaches the array border and triggers an additional wall that propagates inside the array. As that domain wall traverses the different inter-antidot regions, the average magnetization of these regions changes to the intermediate easy-axis direction. At the point for which the domain wall has already swept the array, the external zone is completely reversed but the average magnetization of the array is still aligned along the intermediate easy-axis direction and this fact creates a domain wall in the outer array region pinned at the antidot structure. A second (H_{s2_a}) irreversible process occurs when that wall gets unpinned from the outer line of antidots. Consequently, the hysteresis loops calculated out of the easy and hard axes exhibit two irreversible jumps with a higher switching fields than those of the thin films.

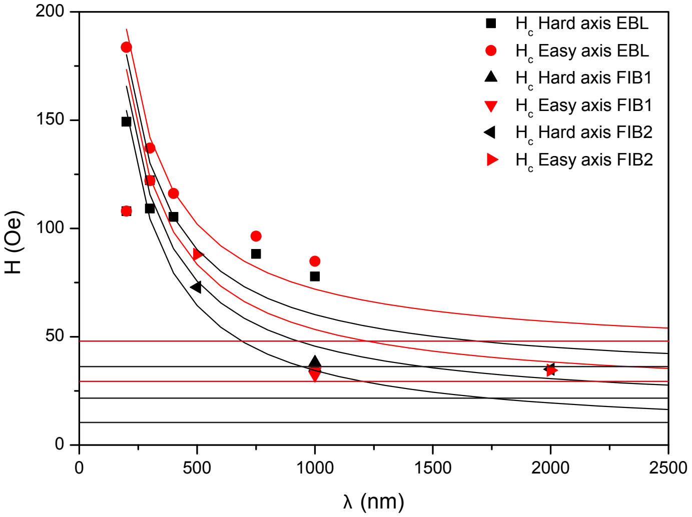

Figure 4.6: Comparison of the coercive field *vs* separation for all the antidots arrays, the horizontal lines correspond to the coercivities of the thin films before the lithography.

Contrary to the case of the nanowires the coercivity depends on the surrounding thin film, assuming this model where the reversal process starts outside of the array. This is in good agreement with figure 4.6, that represents the coercivity of all the arrays. These arrays were lithographed in three different thin films, with different coercive fields, as said in section 4.2. It is not possible to directly compare the coercivity of the antidots lithographed in different films, because for arrays with similar dimensions it strongly depends on the surrounding thin film. Even though the arrays fabricated by FIB are surrounded by a frame the coercivity depends on the original thin film. The reversal process should start in the film in contact with the edges, the frame does not make a difference in the reversal process of the antidots.

λ (nm)	D (nm)	H_c e.a. (Oe)	H_c h.a. (Oe)
200	200	108	108
	400	184	149
300	300	122	109
	400	137	122

Table 4.2: Variation of the coercive field with the diameter for a fixed λ

It is clear that the coercivity increases while λ decreases for all the arrays. Taking into account that the magnetization is stabilized around the antidots, in a region of the order of 50 nm (correlation length), to minimize the magnetostatic energy, a decrease of the distance between the antidots increases the percentage of these stable magnetization regions, so does the coercivity. However, the coercivity also depends on the diameter of the antidots, it increases with the antidots diameter for a given separation, as shown in table 4.2, because the percentage of the stable magnetization area also increases.

One parameter to compare all the arrays could be the increment of the coercivity with respect to that of the thin film. Representing this

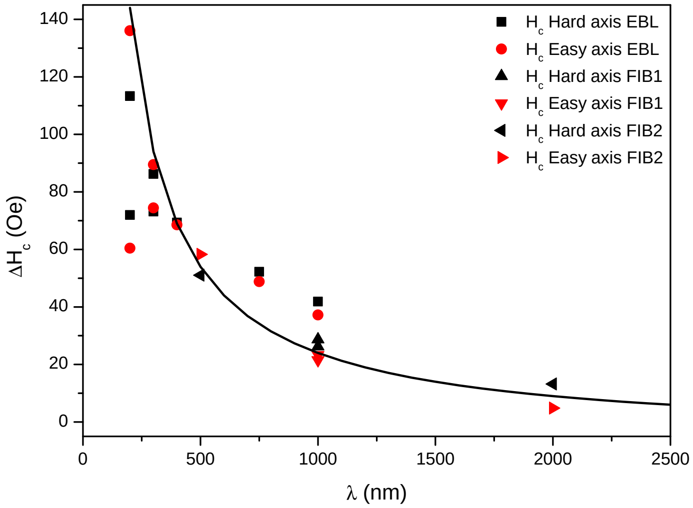

Figure 4.7: Comparison of the increment of coercive field *vs* separation for the three antidots arrays.

increment versus the separation, figure 4.7, the global behaviour approaches $1/\lambda$ reasonably, taking into account that in this case the diameter has also a contribution to the increment.

The antidots induce a shape anisotropy due to the magnetization inhomogeneities, appearing at the lateral surface of the antidots to minimize the dipolar energy, as shown figure 4.8. When the magnetization is along one direction the edges of the antidots at the beginning and at the end of the magnetization vector act as poles, creating a dipolar field against the magnetization. When these poles are closer the dipolar field is higher, so it is more difficult to have the magnetization along the minimum antidots separation than along the maximum separation. That is why the easy axes are along the diagonals and the hard axes along the rows and the columns of the array.

It could be assumed that the magnetization inhomogeneities around the antidots have a width of approximately 20 nm. Calculating percentage of

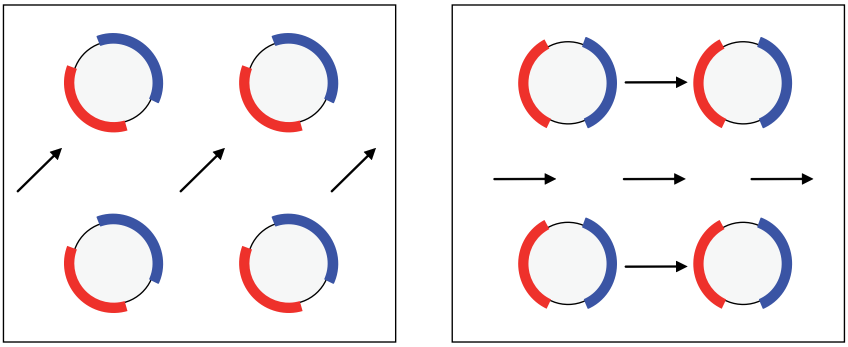

Figure 4.8: Scheme of the dipolar interactions.

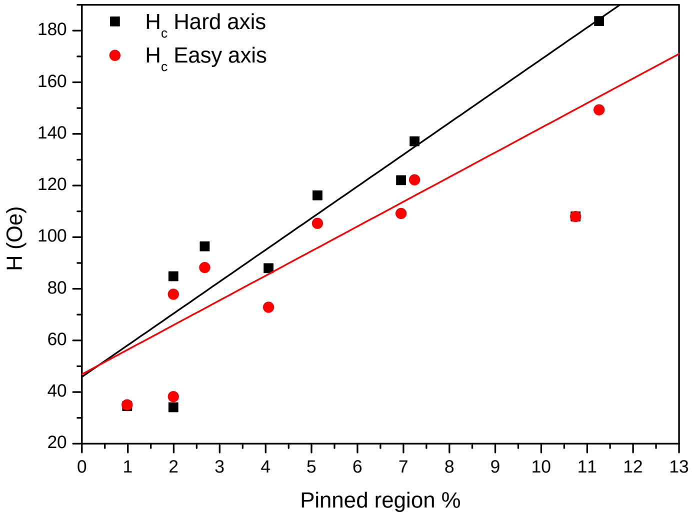

Figure 4.9: Coercive field *vs* percentage of pinned region.

pinned Fe and representing the coercivity field against it, shown in figure 4.9, all the arrays, but the $D = \lambda = 200$ nm one, follow a linear behaviour. The adjustments were made for all the arrays (but the $D = \lambda = 200$ nm), it could be seen that the hard axis increase more rapidly than the easy one, which might be due to the increase of the shape anisotropy while the percentage of pinned Fe increases.

As represented in figure 4.1, a and λ are the distances between the antidots edges along the diagonal and the side of the array, respectively. When the ratio a/λ increases, the relation between the distances separating the poles along the diagonal ad the rows increase, thus increasing the shape anisotropy due to the dipolar interactions explained above.

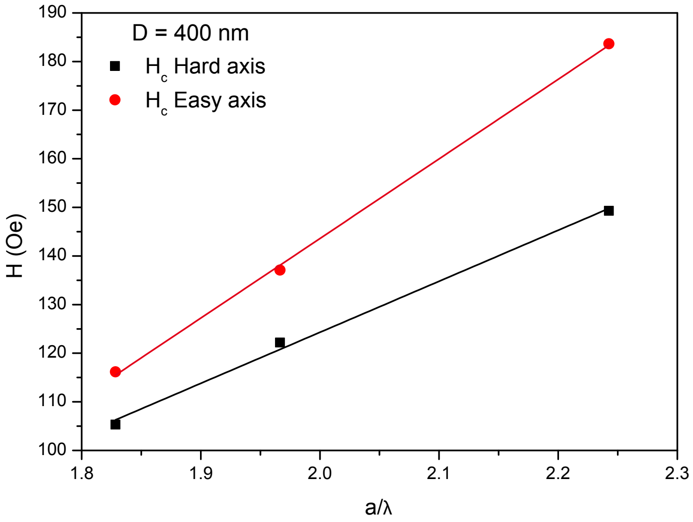

Figure 4.10: Coercive field for antidots with $D = 400$ nm *vs* a/λ.

This increasing of the induced shape anisotropy with the ratio a/λ can be seen comparing arrays with the same diameter and different λ. Figure 4.10 represents the coercivity of the easy and hard axis versus a/λ of three arrays in the EBL thin film that fulfil this condition. When a/λ increases the difference between the two coercivities increases, the easy axis coercivity increases more than the hard axis one. This shows that the shape anisotropy increases with a/λ, as expected.

This behaviour is consistent with previous results presented by Torres Bruna [16] for antidots with $D = 1\ \mu$m and different λ, where the induced anisotropy also increases with decreasing separations.

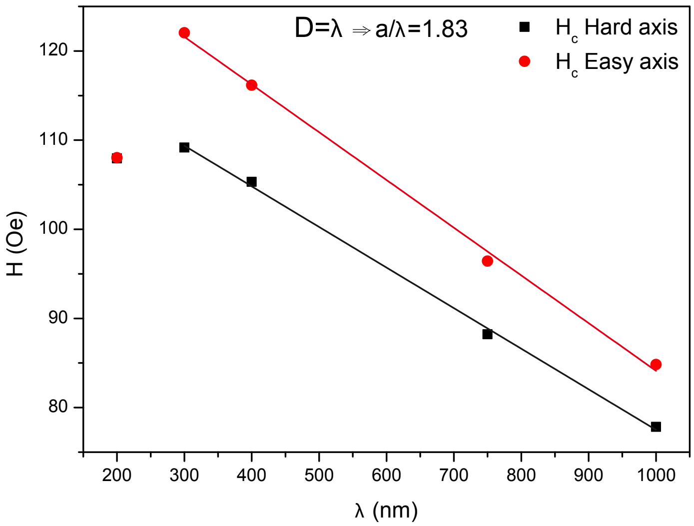

Figure 4.11: Coercive field *vs* separation for EBL arrays with $D = \lambda$.

For the arrays with $D = \lambda$ the ratio a/λ is constant, $a/\lambda = 1.83$, on the EBL thin film there are five different arrays with this characteristic, with $D = \lambda = 1000$, 750, 400, 300 and 200 nm. The arrays made by FIB with the same characteristic are not comparable with them, as already explained, because they were lithographed in different films. For all these arrays but $D = \lambda = 200$ nm it is clear how while D and λ decrease both the easy and hard axis coercive fields increase. Figure 4.11 represents this increase, it can be seen how the difference between the two fields also increases when the dimensions are decreasing, even though the slopes for both axis are not very different. This might be because not only the ratio a/λ affects the induced shape anisotropy, when the D is smaller the coercive field along the hard axis does not increase as much as the easy axis one because the antidots are too close to each other making the magnetization harder to align along that axis.

For $D = \lambda = 200$ nm a non expected behaviour occurs, both fields decrease and are the same. Heyderman *et al.* show a dramatic change in the magnetic domain configuration for square antidots of similar size [17, 18]. The unexpected decrease of the coercivity observed for the EBL arrays with $D = \lambda = 200$ nm might mark a start of change of tendency for shorter antidot distances. Unfortunately, no arrays with $\lambda < 200$ nm were fabricated during the works carried out in this thesis. Further studies for the low λ range need to be conducted in order to confirm it.

The arrays with $D = \lambda = 1$ μm lithographed by FIB were in a very soft thin film and isotropic, with a coercive field of 10 Oe either in the hard and easy axis. The coercive fields of both arrays are almost equal and still being isotropic. This should be because the antidots are far enough for not inducing a shape anisotropy, even though the coercive field increase in comparison to the thin film one. They make the film harder, but without induced anisotropy.

4.4.2 Magnetic Transmission X-ray Microscopy

In order to get insight into the magnetization mechanism of the antidots arrays, a set of arrays was fabricated on a silicon nitride membrane following the procedure outlined in section 3.4.3. All the arrays were lithographed by FIB, using the same intensity, 300 pA, and they were studied by the magnetic transmission X-ray microscopy (MTXM) in collaboration with Prof. Peter Fischer at beamline 6.1.2 in the Advanced Light Source (ALS) of the Lawrence Berkeley National Laboratory (LBNL) [19]. The high spatial resolution of MTXM ($\approx$ 20 nm) and the possibility to acquire images under applied magnetic fields allows to observe the fine details of the magnetic spin configurations and the reversal behaviour of the arrays.

Figures 4.12 and 4.13 represent two sequences of MTXM images

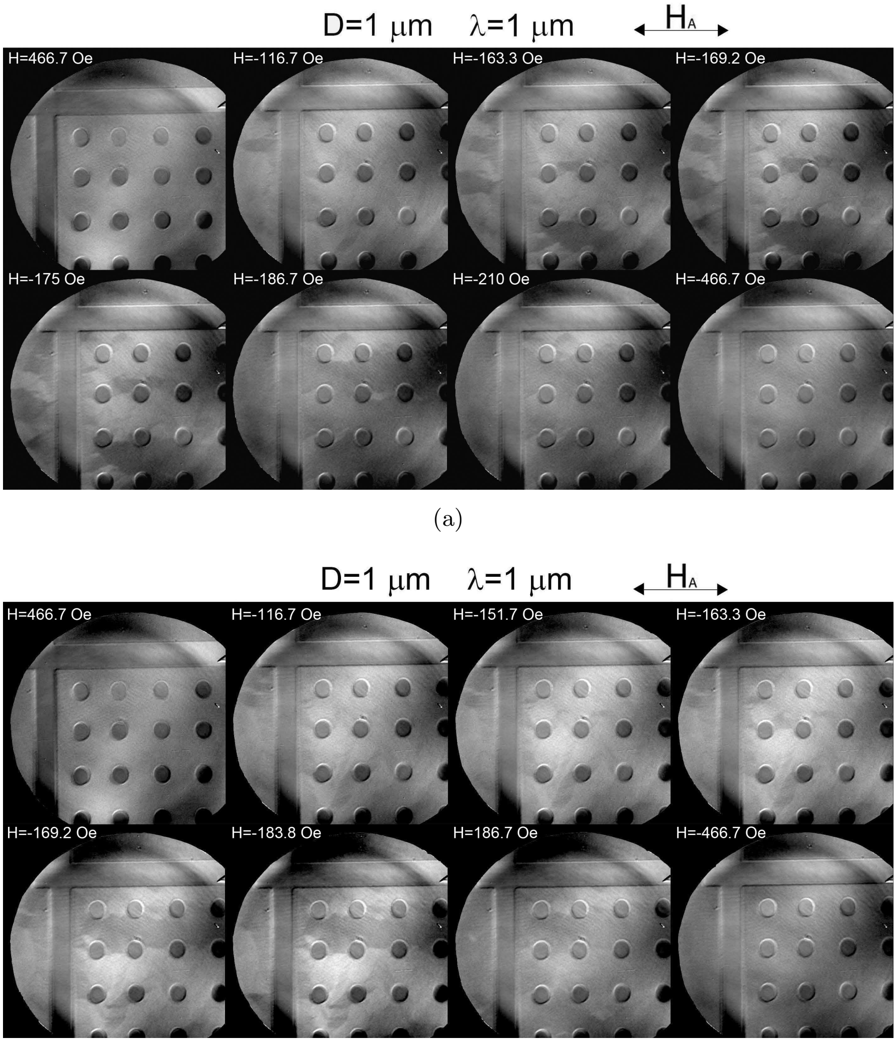

(a)

(b)

Figure 4.12: Dependence with the magnetic field of MTXM images of the corner of the array $D = \lambda = 1$ μm (a) first and (b) second measurements.

corresponding to an array with $D = \lambda = 1$ μm, obtained by sweeping the in-plane magnetic field from 470 Oe to -470 Oe, approximately. This is enough to run the magnetization from positive to negative saturation. The magnetic contrast of these images results from the subtraction of the images with both light polarizations (left and right circularly polarized) and it scales with the projection of the local magnetization onto the photon propagation direction (the membrane is not oriented perpendicular to the propagation direction). The magnetization sensitivity direction (MSD) is parallel to H_A: Ferromagnetic domains with magnetic spins parallel or antiparallel to the MSD appear black or white in the MTXM image, respectively.

Figures 4.12 (a) and (b) show two sequences of the evolution of the magnetization with the field in a region near the corner of the array. Although both images were acquired under identical experimental conditions, the configurations of domains and walls are different in these sequences. From these figures it is clear that the the formation of the walls takes place in the edge that is surrounding the array, in agreement with the model by F. García Sanchez *et al.* [15]. In both sequences the first domain appears at -116.7 Oe and the second one at -163.3 Oe. During the first sweeping run (figure 4.12(a)) one domain starts its propagation at the edge between the two bottom rows, at -163.3 Oe; at -186.7 Oe most of the array is reversed, just the region between the edge and the top row remains unswitched. This region is finally reversed between -210 Oe and -466.7 Oe, leading to the full saturation of the array in the negative direction. During the second run (figure 4.12(b)) a domain appears between the two top rows, at -169.2 Oe; at -183.8 Oe new domains appear and at -186.7 Oe the array is almost fully reversed, again with the exception of the area between the edge and the top row. Finally, the array results fully reversed upon the application of a field of -466.7 Oe.

These sequences suggest that the reversal processes starts at the edges of the array and show that they are not strictly repetitive. In both cases the last part to reverse its magnetization is the region between the edge and the top row of antidots.

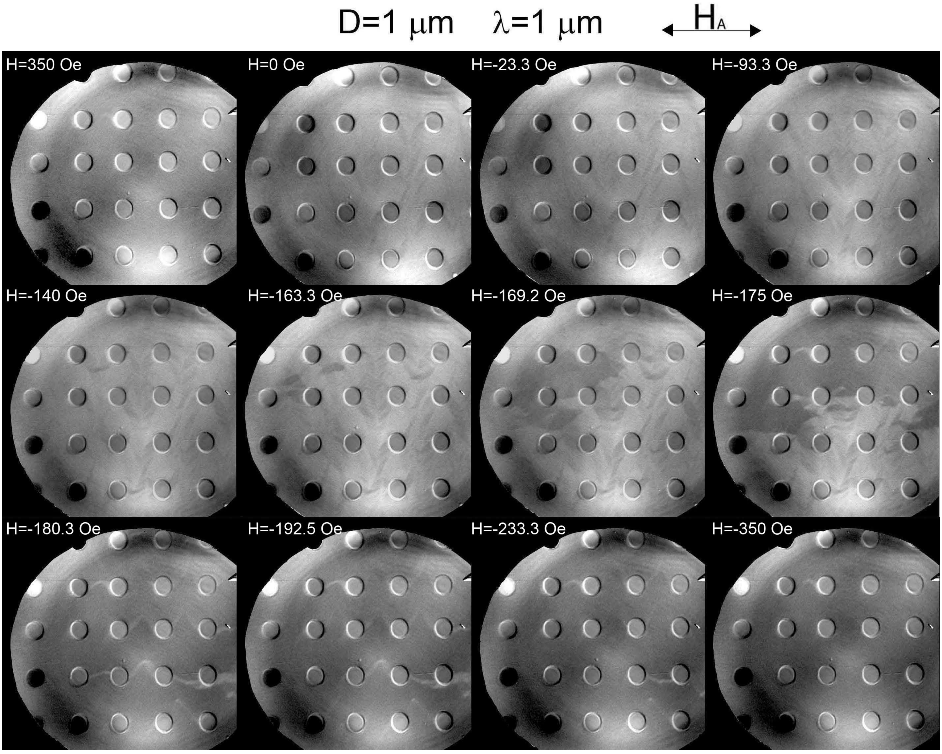

Figure 4.13: Dependence with the magnetic field of MTXM images of the array $D = \lambda = 1$ μm.

Figure 4.13 shows a sequence of images corresponding to a central region, far from the edges of the array. In this case, some domains are formed pointing along the diagonal of the array, between the remanent state and -163.3 Oe. At -169.2 Oe a large reversed domain appears between two rows which propagates partially to the next lower row and, when the field increases up to -175 Oe, to the upper rows. part of the array is reversed. At -180.3 Oe the magnetization reversal is almost complete, with just some unreversed domains between the antidots requiring higher fields for the switching; at -350 Oe the array is fully saturated.

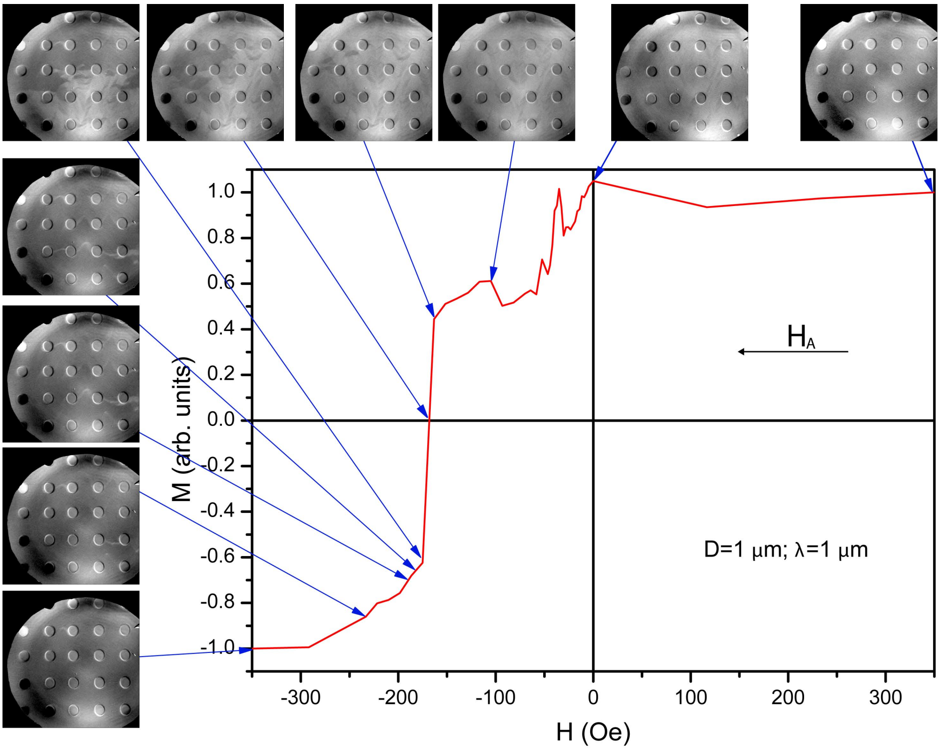

Figure 4.14: Hysteresis loop and MTXM images of the array $D = \lambda = 1\ \mu$m.

A quantitative analysis of the evolution of the magnetization with the applied field can be carried out by measuring the area associated with each domain along a sequence, by means of an image treatment software (e.g. ImageJ). As a result, the demagnetization branch of a hysteresis loop can be traced, associating the images prior and after each reversal event to its magnetization jump. Image 4.14 shows the demagnetization branch of the loop obtained for the array with $D = \lambda = 1\ \mu$m using the images of figure 4.13.

The fact that the reversed domains are formed between the antidots rows, in all the arrays fabricated on Silicon Nitride membranes and analysed by MTXM, is congruent with the observations of Heyderman *et al.* [11, 20] in Co arrays, in spite of the different anisotropy constants of Fe and Co. It is important to remark, however, that the Fe films deposited on Silicon Nitride are polycrystalline, in contrast with the films deposited on MgO, which are clarly singlecrystalline. In addition, the resolution of the images shown in figures 4.12 and 4.13 is not good enough to visualize the domain wall configurations. These considerations compel us to be cautious about assuming that the evolution of the magnetization evidenced through the MTXM images can be readily transposed to that of the arrays fabricated on singlecrystalline films.

In all the different arrays the domains are formed in between the antidots rows as it happens in the Co arrays of. The big different between the Co and the Fe arrays is the magnetocrystalline anisotropy, this Fe thin films are isotropic. The images shown in figures have not so good resolution to see the configuration of the domain walls, so there can not be seen the domain walls as they have reported and there might be some differences due to the anisotropy.

Bibliography

[1] J. M. González, O. A. Chubykalo-Fesenko, F. García-Sánchez, J. M. Torres Bruna, J. Bartolomé and L. A. García Vinuesa, *"Reversible magnetization variations in large field ranges associated to periodic arrays of antidots"* IEEE Transactions on Magnetics **41** (10) 3106–3108 (2005).

[2] P. Vavassori, V. Metlushko, R. Osgood, M. Grimsditch, U. Welp, G. Crabtree, W. Fan, S. Brueck, B. Ilic and P. Hesketh, *"Magnetic information in the light diffracted by a negative dot array of Fe"* Physical Review B **59** (9) 6337–6343 (1999).

[3] A. O. Adeyeye, J. A. C. Bland and C. Daboo, *"Magnetic properties of arrays of "holes" in* $Ni_{80}Fe_{20}$ *films"* Applied Physics Letters **70** (23) 3164–3166 (1997).

[4] I. Ruiz-Feal, L. López-Díaz, A. Hirohata, J. Rothman, C. M. Guertler, J. A. C. Bland, L. M. García, J. M. Torres Bruna, J. Bartolomé, F. Bartolomé, M. Natali, D. Decanini and Y. Chen, *"Geometric coercivity scaling in magnetic thin film antidot arrays"* Journal of Magnetism and Magnetic Materials **242-245** (Part 1) 597–600 (2002).

[5] M. Jaafar, D. Navas, A. Asenjo, M. Vázquez, M. Hernández-Vélez and J. M. García-Martín, *"Magnetic domain structure of nanohole arrays in Ni films"* Journal of Applied Physics **101** (9) 09F513 (2007).

[6] J. Torres Bruna, J. Bartolomé, L. García Vinuesa, F. García Sánchez, J. González and O. Chubykalo-Fesenko, *"A micromagnetic study of the hysteretic behavior of antidot Fe films"* Journal of Magnetism and Magnetic Materials **290-291** (Part 1) 149–152 (2005).

[7] F. Pigazo, F. García Sánchez, F. J. Palomares, J. M. González, O. Chubykalo-Fesenko, F. Cebollada, J. M. Torres Bruna, J. Bartolomé and L. M. García Vinuesa, *"Experimental and computational analysis of the angular dependence of the hysteresis processes in an antidots array"* Journal of Applied Physics **99** (8) 08S503 (2006).

[8] C. C. Wang, A. O. Adeyeye and N. Singh, *"Magnetic antidot nanostructures: effect of lattice geometry"* Nanotechnology **17** (6) 1629–1636 (2006).

[9] P. Vavassori, G. Gubbiotti, G. Zangari, C. T. Yu, H. Yin, H. Jiang and G. J. Mankey, *"Lattice symmetry and magnetization reversal in micron-size antidot arrays in Permalloy film"* Journal of Applied Physics **91** (10) 7992–7994 (2002).

[10] A. Pérez-Junquera, G. Rodríguez-Rodríguez, M. Vélez, J. I. Martín, H. Rubio and J. M. Alameda, *"Néel wall pinning on amorphous Co_xSi_{1-x} and Co_yZr_{1-y} films with arrays of antidots in the diluted regime"* Journal of Applied Physics **99** (3) 033902 (2006).

[11] L. J. Heyderman, F. Nolting, D. Backes, S. Czekaj, L. López-Díaz, M. Klaui, U. Rudiger, C. A. F. Vaz, J. A. C. Bland, R. J. Matelon, U. G. Volkmann and P. Fischer, *"Magnetization reversal in cobalt antidot arrays"* Physical Review B **73** (21) 214429 (2006).

[12] J.-G. Zhu and Y. Tang, *"Micromagnetics of percolated perpendicular media"* IEEE Transactions on Magnetics **43** (2, Part 2) 687–692 (2007).

[13] M. B. A. Jalil, *"Bit isolation in periodic antidot arrays using transverse applied fields"* Journal of Applied Physics **93** (10) 7053–7055 (2003).

[14] P. Gaunt, *"Ferromagnetic domain-wall pinning by a random array of inhomogeneities"* Philosophical Magazine B-Physics of Condensed Matter Statistical Mechanics Electronic Optical and Magnetic Properties **48** (3) 261–276 (1983).

[15] F. García-Sánchez, E. Paz, F. Pigazo, O. Chubykalo-Fesenko, F. J. Palomares, J. M. González, F. Cebollada, J. Bartolomé and L. M. García, *"Coercivity mechanisms in lithographed antidot arrays"* Europhysics Letters **84** (6) 67002 (2008).

[16] J. M. Torres Bruna, *Propiedades magnéticas de sistemas nano y micrométricos: muliticapas de nanopartículas de cobalto y redes de agujeros en hierro.* PhD thesis, Universidad de Zaragoza-CSIC (2005).

[17] L. J. Heyderman, F. Nolting and C. Quitmann, *"X-ray photoemission electron microscopy investigation of magnetic thin film antidot arrays"* Applied Physics Letters **83** (9) 1797–1799 (2003).

[18] L. J. Heyderman, H. H. Solak, F. Nolting and C. Quitmann, *"Fabrication of nanoscale antidot arrays and magnetic observations*

using x-ray photoemission electron microscopy" Journal of Applied Physics **95** (11, Part 2) 6651–6653 (2004).

[19] P. Fischer, D.-H. Kim, W. Chao, J. A. Liddle, E. H. Anderson and D. T. Attwood, *"Soft X-ray microscopy of nanomagnetism"* Materials Today **9** (1-2) 26–33 (2006).

[20] L. Heyderman, S. Czekaj, F. Nolting, D.-H. Kim and P. Fischer, *"Cobalt antidot arrays on membranes: Fabrication and investigation with transmission X-ray microscopy"* Journal of Magnetism and Magnetic Materials **316** (2) 99–102 (2007).

Conclusions

This thesis is devoted to the preparation, characterization and magnetic properties of epitaxial Fe nanostructures. In particular, the magnetization processes of artificial arrays of two types of motifs, planar nanowires and antidots, are studied. The aim of this thesis was to produce several series of these types of arrays by means of a reliable, controlled procedure allowing to tailor their hysteresis behaviour basically through their morphological features and the Fe intrinsic properties, with as little influence as possible of other extrinsic factors. From this point of view, this thesis has a very broad scope focused on each and every one of the stages required to fabricate the high quality nanoelements studied: (i) the growth and characterization of thin films, structural, chemical and magnetically; (ii) the optimization of the lithography processes to avoid the generation of undesired defects; (iii) the careful analysis of the correlation between the crystallochemical structure and the magnetic properties of the arrays of nanowires and antidots.

The main results of this work are summarized as follows:

- Regarding the preparation of thin films grown on MgO (001) substrates, the ability to produce epitaxial Au (001)/Fe (001) films with sharp and flat interfaces upon optimization of growth conditions has been achieved. The crystalline characterization, combining different high sensitivity techniques, evidenced their high quality singlecrystalline character.
- Au/Fe grown films present well controlled magnetization reversal processes with very narrow switching field distribution, and perfect biaxial magnetocrystalline anisotropy with no evidences of extra uniaxial contribution.

- The optimization of Focused Ion Beam (FIB) and Electron Beam Lithography (EBL) parameters has allowed the controlled fabrication of well ordered arrays of nanowires and antidots in terms of their shape and size, minimizing the influence of the unavoidable imperfections inherent to them on the crystalline structure of the Fe films, with negligible increase in roughness and lattice distortion.
- The magnetization processes of high quality Fe singlecrystalline planar nanowires, with widths between 100 nm and 1 μm, have confirmed that their reversal evolve from wall pinning, at low angles between the applied field and their long axis, to basically uniform magnetization rotation, at high angles. This behaviour has been described in terms of single spin configuration, ruling out the formation of multidomain structures even at high angles.
- The magnetic characterization of the antidots, with diameter and separation between 200 nm and 2 μm, has shown that the coercivity of the arrays is up to a factor of 10 above that of the films, increasing sharply with decreasing separation. The dependence of the coercivity on the diameter and separation arrays has been analysed as a function of the percentage of magnetic material around the antidots that forms inhomogeneous structures, evaluated from the magnetostatic correlation length.

In summary, this thesis has shown that the magnetic properties of the lithographed nanoelements, wires and antidots, depend almost exclusively on their morphology and characteristic dimensions, with minimum influence of the imperfections inherent to the different fabrication routes.

Conclusiones

En esta tesis se ha estudiado la prepración, caracterización y las propiedades magnéticas de nanoestructuras de Fe epitaxial, en particular, los procesos de imanación de redes artificiales con dos tipos de motivos, nanohilos planos y antidots. El propósito de esta tesis es la fabricación de diversas series de estas redes mediante un procesos controlados y reproducibles que permitan diseñar a medida sus procesos de histéresis a través de sus características morfolgícas y las propiedades intriníosecas del Fe, con la menor influencia posible de otros factores extrínsecos. Desde este punto de vista, esta tesis tiene un amplio objetivo enfocado en cada uno de los pasos necesarios para fabricar los nanoelementos de alta calidad: (i) el crecimiento de láminas delgadas y su caracterización estructural, química y magnética; (ii) la optimización de los procesos litográficos para evitar defectos no deseados; (iii) el cuidadoso análisis de la correlación entre la estructura cristalina y química y las propiedades magnéticas de las redes de nanohilos y antidots.

Los principales resultados de este trabajo se resumen de la siguiente manera:

- Se ha conseguido la preparación de láminas epitaxiales de Au (001)/Fe (001) sobre substratos de MgO (001) con intercaras abruptas y planas tras la optimización de las condiciones de crecimiento. La caracterización cristalina realizada mediante la combinación de técnicas de alta sensibilidad, ha puesto de manifiesto su alta calidad monocristalina.
- Las láminas de Au/Fe presentan procesos de la imanación controlados con una distibución de campos de inversión muy estrecha, y una anisotropía manetocristalina biáxica perfecta, sin contribución uniáxica.

- La optimización de los parámetros en las litografías por haz de iones (FIB) y de electrones (EBL) ha permitido la fabbricación controlada de redes ordenadas de nanohilos y antidots en función de su forma y tamaño, minimizando la influencia de imperfecciones inherentes a estas técnicas en la estructura cristalina de la lámina delgada, con efectos despreciables en el aumento de la rugosidad y del desorden.
- Los procesos de imanación en nanohilos planos de Fe monocristalino, de anchuras entre 100 nm y 1 μm, confirman que su inversión tiene lugar mediante el enganche de pared, para bajos ángulos entre el campo aplicado y el eje largo de los hilos, y mediante un proceso de rotación de la imanación basicamente uniforme a altos ángulos. Este comportamiento ha sido descrito como una configuración de un único spin, descartando la formación de estructuras de tipo multidominio a altos ángulos.
- La caracterización magnética de los antidos, de diametro y separación entre 200 nm y 2 μm, ha mostrado un aumento hasta de factor 10 en la coercitividad de las redes respecto a la de la lámina, aumentando rápidamente cuando la separación decrece. La dependencia de la coercitividad con el diámetro y la separación ha sido analizada en función del porcentaje de material magnético alrededor de los antidots que forma estructuras inhomogéneas, evaluado mediante la longitud de correlación magnetostática.

En resumen, esta tesis muestra que las propiedades magnéticas de nanoelementos litografiados, hilos y antidots, dependen fundamentalmente de su morfología y dimensiones, con mínima influencia de las imperfecciones inherentes a las diferentes técnicas de fabricación.

List of Acronyms

AFM	Atomic Force Microscopy
EBL	Electron beam lithography
ESRF	European Synchrotron Radiation Facility
FIB	Focused Ion Beam
FMR	Ferromagnetic Resonance
FWHM	Full Width at Half Maximum
IBE	Ion Beam Etching
ICMM	Instituto de Ciencia de Materiales de Madrid
IPA	Isopropyl Alcohol
LHe	Liquid He
LIMS	Liquid-Metal Ion Source
MAE	Magnetocrystalline Anisotropy Energy
MBE	Molecular Beam Epitaxy
MCP	Multichannel Plate
MIBK	Methyl Isobutyl Ketone
MOKE	Magneto Optical Kerr Effect Magnetometer
MTXM	Magnetic Transmission X-ray Microscopy
NMP	1-Methyl 2-Pyrrolidone
OOMF	Object Oriented MicroMagnetic Framework
PLD	Pulsed Laser Deposition
PMMA	Poly-Methyl Methacrylate
PVD	Physical Vapor Deposition
RC	Rocking Curve
rms	Root Mean Square
RSM	Reciprocal Space Map
RT	Room Temperature

SEM	Scanning Electron Microscopy
SFD	Switching Field Distribution
STXM	Scanning Transmission X-ray Microscopy
TEM	Transmission Electron Microscopy
UHV	Ultra High Vacumm
VSM	Vibrating Sample Magnetometer
XPS	X-ray Photoelectron Spectroscopy
XRD	X-ray Diffraction
XRR	X-ray Reflectometry

List of Figures

List of Tables